12-2018

sCAM: An Untethered Insertable Laparoscopic Surgical Camera Robot

Ning Li
University of Tennessee

To the Graduate Council:

I am submitting herewith a dissertation written by Ning Li entitled "sCAM: An Untethered Insertable Laparoscopic Surgical Camera Robot." I have examined the final electronic copy of this dissertation for form and content and recommend that it be accepted in partial fulfillment of the requirements for the degree of Doctor of Philosophy, with a major in Mechanical Engineering.

Jindong Tan, Major Professor

We have read this dissertation and recommend its acceptance:

William R. Hamel, Hairong Qi, Eric R. Wade

Accepted for the Council:

Dixie L. Thompson

Vice Provost and Dean of the Graduate School

(Original signatures are on file with official student records.)

sCAM: An Untethered Insertable Laparoscopic Surgical Camera Robot

A Dissertation Presented for the

Doctor of Philosophy

Degree

The University of Tennessee, Knoxville

Ning Li

December 2018

I dedicate this dissertation to my parents, Shuhang Li and Shilan Ma, and my wife, Xueyan Shao.

Acknowledgments

I have been supported by so many family, friends and colleagues during my Ph.D. research, without whose love and help this work wouldn't have been possible.

My advisor, Dr. Jindong Tan took me on as his first graduate student since he arrived at the University of Tennessee and opened the door for me to the amazing world of biomedical robotics. His enlightening, guidance, and encouragement have not only navigated me through the academic research but also my life in an alien culture, especially during those hard times. Also, my sincere appreciation goes to my other committee members, Dr. William R. Hamel, Dr. Eric R. Wade, and Dr. Hairong Qi whose input and valuable suggestions have greatly enhanced this work.

Also, I want to thank my fellow lab members: Dr. Hongsheng He, Dr. Zhenzhou Shao, Dr. Xiaolong Liu, Mr. Yan Li, Mr. Reza Yazdanpanah A., and Mr. Zhe Su for their generous help and friendship.

During my Ph.D. study, Ms. Linhui Li and Prof. Hongxing Wei have shown their kind considerations, which makes me feel warm from home overseas. Meanwhile, my best American friends Josh and Nicole Flory and their four lovely kids have brought me so much happiness and experience in American culture and values.

Last but not least, I want to express my special thanks to my family, whose constant support, tolerance, and love have been the source of my courage and motivation to march forward, and meet the challenges.

This work is supported by the National Science Foundation grant No. 1309921 and my Ph.D. study is partially supported by the China Scholarship Council.

00:07 on Friday 17th August, 2018, DO332

Abstract

Fully insertable robotic imaging devices represent a promising future of minimally invasive laparoscopic vision. Emerging research efforts in this field have resulted in several proof-of-concept prototypes. One common drawback of these designs derives from their clumsy tethering wires which not only cause operational interference but also reduce camera mobility. Meanwhile, these insertable laparoscopic cameras are manipulated without any pose information or haptic feedback, which results in open loop motion control and raises concerns about surgical safety caused by inappropriate use of force.

This dissertation proposes, implements, and validates an untethered insertable laparoscopic surgical camera (sCAM) robot. Contributions presented in this work include: (1) feasibility of an untethered fully insertable laparoscopic surgical camera, (2) camera-tissue interaction characterization and force sensing, (3) pose estimation, visualization, and feedback with sCAM, and (4) robotic-assisted closed-loop laparoscopic camera control. Borrowing the principle of spherical motors, camera anchoring and actuation are achieved through transabdominal magnetic coupling in a stator-rotor manner. To avoid the tethering wires, laparoscopic vision and control communication are realized with dedicated wireless links based on onboard power. A non-invasive indirect approach is proposed to provide real-time camera-tissue interaction force measurement, which, assisted by camera-tissue interaction modeling, predicts stress distribution over the tissue surface. Meanwhile, the camera pose is remotely estimated and visualized using complementary filtering based on onboard motion sensing. Facilitated by the force measurement and pose estimation, robotic-assisted closed-loop control has been realized in a double-loop control scheme with shared autonomy between surgeons and the robotic controller.

The sCAM has brought robotic laparoscopic imaging one step further toward less invasiveness and more dexterity. Initial *ex vivo* test results have verified functions of the implemented sCAM design and the proposed force measurement and pose estimation approaches, demonstrating the technical feasibility of a tetherless insertable laparoscopic camera. Robotic-assisted control has shown its potential to free surgeons from low-level intricate camera manipulation workload and improve precision and intuitiveness in laparoscopic imaging.

Table of Contents

List of Tables

List of Figures

Chapter 1

Introduction

Human kind began to design intervention treatment devices as soon as they learnt how to make tools since ancient times [1], each time more sophisticated than the last. However, until the industrial revolution, surgeons were not able to overcome the three major obstacles which had plagued the medical profession from its infancy – bleeding, pain, and infection. By now, interventional surgical techniques have taken a significant branch in modern medical science, capable of treating a wide spectrum of diseases and conditions. However, clinically available surgical techniques remain invasive in principle. For almost a century, medical pioneers and researchers have been exploring towards minimally invasive or even non-invasive techniques for improved surgical performance and quality of life.

1.1 Motivation

Minimally invasive surgery (MIS) encompasses surgical techniques allowing for small incisions, reduced trauma, less bleeding, better cosmetic results, and faster recovery [1] compared to traditional open surgery (OS), thus is getting accepted for an increasing series of procedures. As is indicated in Fig. 1.1, MIS has been continuously redefined by emerging technologies enabled by advances in medical instrumentation and surgical robotics.

[1] According to Wikipedia: https://en.wikipedia.org/wiki/History_of_surgery

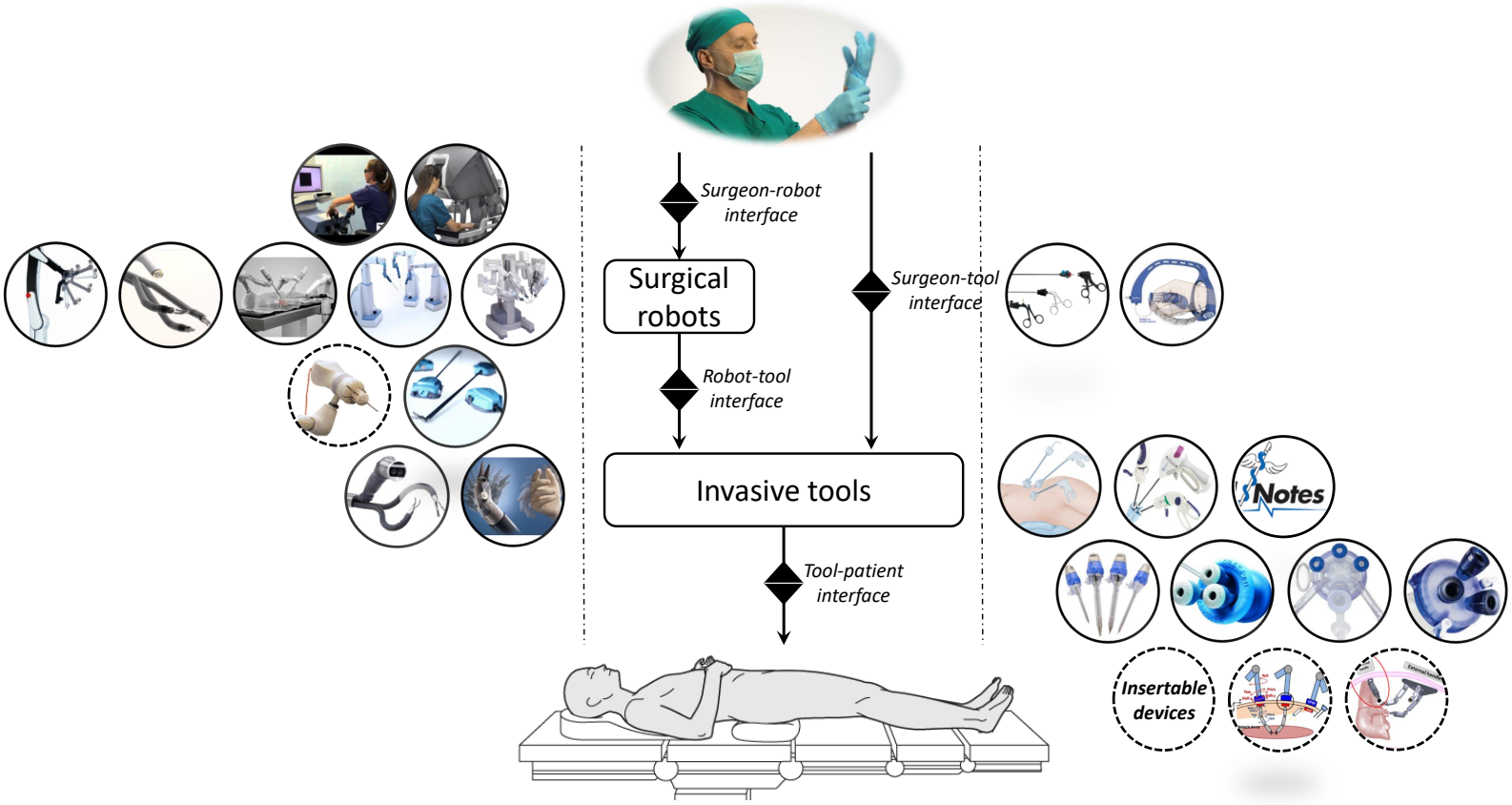

Figure 1.1: Innovations along the way from the surgeon's hands to the patient's anatomy.

Laparoscopic surgery (LS) represents one popular subspecialty of MIS that is used to treat conditions in the abdominopelvic cavity [2], which is conventionally performed with trocar-based rigid straight devices partially inserted into the patient's anatomy through multiple small incisions (usually 0.5cm∼1.5cm)(multiport laparoscopic surgery, MLS). Although, due to the intrinsic kinematic constraints caused by the trocar, manipulation of these rigid stick devices suffers from the counter-intuitive fulcrum effect and the confined workspace [3], ingenious surgeons have been able to master them by intensive training and continuous practice and even successfully established MLS as the gold standard for many abdominal surgical procedures such as cholecystectomy, splenectomy, and appendectomy etc [4][5].

Aiming to reduce the number of or even eliminate incisions for LS, single-incision laparoscopic surgery (SILS) [4][6][7][8][9] and natural orifice transluminal endoscopic surgery (NOTES) [10] have been introduced and enthusiastically practiced by surgeons in the past decades [4]. SILS is typically performed with a single incision in the umbilicus while NOTES utilizes natural openings of the human body for surgical device introduction, enabling invisible scarring or even no scarring cosmetic outcomes. These patient-oriented benefits are achieved at the cost of sacrificing more ease of operation for surgeons including the loss of triangulation and increased inter-device clashing, since the surgical instruments and the laparoscope share the same entry port in SILS and NOTES. As a result, these techniques give rise to more operational challenges and are often considered difficult procedures even in the hands of the most experienced surgeons [11].

Hence, robotics has found its way into the operating room by mapping complex device movements to intuitive surgeon operations through an ergonomic user interface. Best manifested by the *da Vinci*® series surgical systems [2] (Intuitive Surgical, Inc., Approved by FDA in 2000) [12] and the Senhance Surgical system (TransEnterix Surgical, Inc., Approved by FDA in 2017), robotic-assisted minimally invasive surgery (RMIS) has provided unprecedented operational intuitiveness and precision. However, the laparoscopic devices including the laparoscopic camera adopted for RMIS fail to show equivalent improvements and their workspace is still kinematically restricted to the trocar channel constraints [13][14]. Occasionally, a second cut becomes inevitable for repositioning these laparoscopic devices so

[2]According to: https://www.intuitivesurgical.com/products/davinci-surgical-system/davinci-single-site/

as to get a preferred view angle or better operation triangulation, which may convert a SILS to an MLS or even a OS [15].

Obviously, the trocar-based rigid stick laparoscopic surgical instrument paradigm has become a bottleneck hindering modern MIS progress. A paradigm-shifting minimally invasive surgical technique breaking current instrument boundaries would effectively enhance surgical efficacy, advance MIS instrumentation, and boost the next round of medical science progress. One promising approach lies in pushing miniaturized robotic surgical devices completely into the patient's abdominal cavity [11][16][17][18][7][19] to provide imaging assistance or even perform possible diagnostic and operative tasks. Once introduced into the anatomy, these fully insertable laparoscopic devices leave the entry port available for other surgical instruments, which helps reduce the number and/or size of incisions, and alleviate inter-device clashing at the entry port. Moreover, these intra-cavity robotic units could locomote under appropriate actuation and eliminate the trocar constraints, granting a larger workspace and field of observation.

1.2 Challenges

Unlike conventional surgical robots which are situated outside the patient's anatomy, cost millions of dollars, and could take a large footprint in the operating room (OR), the fully insertable laparoscopic devices need to be miniaturized to function *in vivo*, space-efficient, cost-effective, and clinically safe. Unique technological and engineering challenges arise from compound physical and medical restrictions for design, implementation, and clinical acceptance of the fully insertable laparoscopic surgical robots.

1.2.1 Robotic Implementation

One immediate challenge to develop fully insertable laparoscopic surgical devices lies in robotic implementation of these minimally invasive medical systems. **From the hardware point of view**, the implementation features integrating the just right resources within a compact biocompatible profile in a reliable robotic manner. *Mechanically*, in order to guarantee minimum invasiveness, the fully insertable laparoscopic surgical device needs to

be miniaturized to a small form factor so as to entirely fit into the peritoneal cavity through a trocar channel ranging 2mm∼18mm in diameter. Meanwhile, for better actuation and motion control, a light weight is always preferred, especially in cases where the actuation force and operation margins might be physically limited. Moreover, to improve *in vivo* mobility and reduce operational interference, physical fixation and tethering to the fully insertable device should be avoided as much as possible. *Electrically*, the robotic insertable laparoscopic device has to incorporate necessary driving, sensing, processing, communicating as well as powering resources so that it can perform desired surgical functions. Therefore, outfitting the insertable laparoscopic device needs to leverage a delicate tradeoff between cutting-edge biomechatronics and stringent space and weight restrictions. Only necessary function payloads and limited resources could be allowed onboard and should be encapsulated in a most space-efficient manner. **From the software point of view**, control and management of onboard resources for these fully insertable devices necessitate logics and algorithms. An effective approach is to use embedded programs executed on a local microcontroller. For safety-critical surgical applications, reliability of these software programs should be an important emphasis. Thus, embedded software running on the fully insertable device should meet high safety and risk management requirements. Usually, the inserted surgical device constitutes only part of the whole system that makes it possible to function. Software running on the other part of the system also needs to be reliable in terms of event response, processing time, and programming efficiency. **Considering clinical applications**, the implemented robotic surgical devices should be easy to introduce, retrieve and sterilize according to appropriate clinical protocols. Meanwhile, these devices must be compatible with existing MIS tools so that they can be seamlessly fitted into the operating room.

1.2.2 Actuation and Mobility

The fully insertable laparoscopic device needs to be effectively anchored and actuated to support designed surgical operations. No physical actuation linkage could be allowed from the outside so that the insertable device could maneuver flexibly in the abdominal cavity. Thus, the robot has to either make use of its onboard actuators or seek for a non-contact transabdominal actuation technology. Although onboard actuators represent

a straightforward mobility solution, they often lead to a bulky robot volume and high power consumption. Non-contact transabdomial actuation based on magnetic coupling could be an innovative approach, however it is quite challenging to model and control. Meanwhile, existing fully insertable laparoscopic devices are usually tethered by a bundle of wires which have been a necessary evil required for video transmission, control communication, and/or powering. These cumbersome tethering wires cause notable operational interference and have been recognized as a major drawback for device mobility [20][11]. To guarantee flexible device mobility, non-contact transabdominal actuation needs to be effectively realized with the cumbersome tethering wires completely eliminated, while the device is still accessible from the outside for actuation, communication, control, and/or powering.

1.2.3 Spatial Information Recovering

In OS, surgeons rely on direct binocular vision on the surgical area thus are able to utilize various cues for spatial information perception. By contrast, spatial information loss has been an intrinsic problem with LS due to the indirect laparoscopic vision [5], which conventionally is a monocular 2D projection of the 3D operating field observed on a 2D display. Not only depth perception is seriously impaired, but also the surgeons have to align the misorientation between instrument movements and the laparoscopic vision through hand-eye coordination while performing the surgical tasks. The spatial information loss problem becomes worse than ever when it comes to fully insertable laparoscopic surgical devices, as the surgeon's hands and eyes have been remotely isolated from these devices. Not only the 3D structural information of the surgical area is lost within the 2D laparoscopic vision, but also the poses (positions and orientations) of the insertable devices are unknown. In order to effectively manipulate these devices from the outside, poses of these devices need to be correctly restored for control feedback. Ultimately, the recovered spatial information is expected to help reconstruct the 3D operating environment remotely in a virtually augmented manner for advanced MIS operation.

1.2.4 Haptic and Force Feedback

Another critical concern stems from restoring the haptic and force feedback of these insertable laparoscopic devices, which plays an important part in making surgical decisions and avoiding intra-operative injury [5]. According to a population-based study, laparoscopic cholecystectomy carries a nearly twofold higher risk of major bile, vascular, and bowel complications compared to open cholecystectomy, due to the inappropriate use of force [21]. In traditional LS, although the haptic perception has been reduced compared to OS due to indirect touch of organs through rigid stick laparoscopic devices, the surgeons are still able to determine shape, texture, and consistency in the absence of visual feedback using indirect palpation [22][23]. However, for the fully insertable laparoscopic surgical devices, as is pointed out in Section 1.2.3, the surgeon's hands have been physically separated from these devices and thus no haptic perception or force sensing could be naturally available. To remotely reproduce the haptic perception and force feedback could benefit both the surgeons and the patients in terms of operation confidence and safety, however, implies great technological challenges that need to be met.

1.3 State of the Art

Motivated by the idea of fully insertable laparoscopic devices, the state of the art could be represented by several proof-of-concept laparoscopic camera prototypes categorized in Fig. 1.2, which have, to different extents, shown their potential to eliminate trocar constraints, reduce surgical incisions, and alleviate inter-device clashing. Starting from mechanical fixation, motorized actuation, and wired tethering, these state-of-the-art designs have been advancing toward magnetic anchoring/actuation and tetherless access.

Hu *et al.* introduced a *cable-tethered* insertable surgical imaging device (Fig. 1.2(a)) with variant implementations [24][25]. *Rigidly sutured* onto the interior abdominal wall, each of these prototypes selectively demonstrated *motorized* pan/tilt motion, stereoscopic vision, zoom and lighting capabilities. By contrast, MARVEL [26][27] designed by Castro *et al.* is a *cable-free motorized* robotic pan/tilt surgical camera (Fig. 1.2(b)). MARVEL established wireless video and control links, however replaced suturing with an anchoring needle which

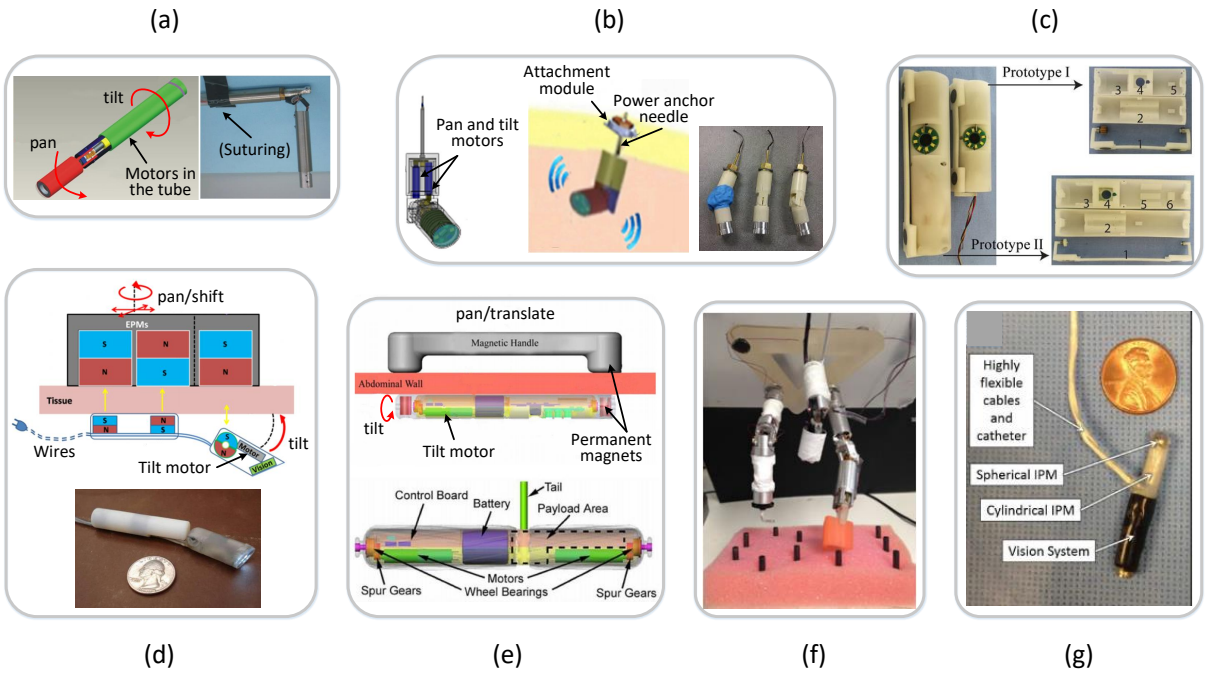

Figure 1.2: Start-of-the-art insertable laparoscopic camera prototypes.

pieced through the abdominal wall for camera fixation and powering. Obviously, both suturing and piercing fixate the camera mechanically and cause extra invasiveness, making reposition of the camera difficult if not impossible.

Instead of fixating the camera mechanically, more flexibility in camera locomotion has been observed with non-invasive transabdominal anchoring based on magnetic coupling. A magnetic levitated laparoscopic imaging robot (Fig. 1.2(d)) designed by Simi *et al.* and Valdastri [28][29] showed the ability to translate the camera in addition to motorized pan and tilt motion. However, two motors integrated onboard the camera for tilt and roll motion made this device bulky and power-consuming [28]. Although they removed one motor in another version [29], a bunch of wires tethering the robot were still required for power supply, motor control, and video transmission. Recognizing operational interference caused by tethering wires from their previous work on tethered *in vivo* mobile surgical robots [30][17], Platt *et al.* presented a *wireless* design of a wheeled ceiling pan/tilt robot (Fig. 1.2(e)) with magnetic anchoring and *motorized* mobility [20]. This platform could be controlled and powered with few physical connections to the camera, except for one small tether for video output. Another two platforms with magnetic anchoring and motorized actuation were contributed

respectively by Menciassi *et al.*(Fig. 1.2(f)) and Fu *et al.*(Fig. 1.2(c)). Menciassi *et al.* were able to dock an array of insertable articulated robots with different functions on a magnetic anchoring frame, offering impressive device dexterity [16][31]. Meanwhile, Fu *et al.* completely eliminated the cumbersome tethering wires to an *in vivo* mobile laparoscopic camera on their second prototype [32]. These designs are characterized by magnetic anchoring and motorized actuation. Although magnetic anchoring has effectively improved mobility of insertable laparoscopic devices, the onboard motors and actuation mechanisms make these prototypes mechanically bulky and complicated.

A pure magnetic anchoring/actuation link for an insertable laparoscopic camera was presented by Garbin and Valdastri *et al.* [33][34] as shown in Fig. 1.2(g). This device allows for manual lateral translation as well as robotic tilt and pan motion based on an orthogonal magnetic arrangement. A small form factor has been achieved by eliminating motors and complicated actuation mechanisms except that a bundle of tethering wires were still required. However, operational interference caused by tethering wires has been recognized as a common drawback of current prototypes [20][11]. As is reported by studies [20][35][36], increasing the number of wires in the tether reduces its overall flexibility and thus affects mobility of the *tethered* camera.

So far, exploring steps have been taken towards eliminating mechanical fixation, motorized actuation, and physical tethering for insertable laparoscopic cameras. Unfortunately, each solution was only able to partially meet these expectations, and a tetherless insertable laparoscopic camera with flexible *in vivo* mobility under magnetic anchoring/actuation remains beyond the state of the art. Moreover, few research efforts have been seen in recovering the lost spatial information or restoring the haptic and force feedback for these insertable laparoscopic devices, which are definite challenges to be met before these devices could finally reach clinical practice.

1.4 Objectives

The work in this dissertation aims to develop an untethered fully insertable laparoscopic surgical camera (sCAM) robot. Specifically, the following four objectives have been targeted.

The **first objective** is robotic design and implementation of the sCAM system which features no physical links to the insertable laparoscopic camera. Specifically, there exists no mechanical fixation or tethering wires to the sCAM robot while the *in vivo* camera is still accessible for anchoring, actuation, communication and control remotely from outside the patient's anatomy.

The **second objective** is to recover the lost camera-tissue contact force measurement and characterize the camera-tissue interaction process. This contact force needs to be maintained in an appropriate safe range so that the camera will neither fall off due to insufficient anchoring nor damage the tissue due to overload. Meanwhile, the camera-tissue interaction model could relate the contact force with pressure distribution over the contact profile.

The **third objective** is to enable tracking the insertable laparoscopic camera in terms of position and orientation. Pose estimation of the camera is not only necessary for robotic closed-loop camera control, but also could be helpful in recovering spatial information of the surgical environment and augmenting laparoscopic vision.

Finally, based on the above objectives, the **fourth objective** is to realize robotic-assisted closed-loop control of this *in vivo* laparoscopic camera, which could provide an intuitive surgeon interface with unprecedented ergonomics and precision. Thus, the surgeons could be potentially freed from low-level intricate camera control workload and focus more on the surgical tasks.

1.5 Contributions

This work develops an sCAM robot that has paradigm-shifting impacts on laparoscopic surgical instrumentation. Achieving the objectives listed in Section 1.4, the fundamental contributions from this research have been summarized as follows.

Feasibility of an Untethered Fully Insertable Laparoscopic Surgical Camera

The sCAM features a novel untethered fully insertable laparoscopic surgical camera that has completely eliminated mechanical fixation, motorized actuation and tethering wires.

Borrowing the principle of spherical motors, camera anchoring and actuation are achieved through transabdominal magnetic coupling in a stator-rotor manner. To avoid the tethering wires, laparoscopic vision and control communication are realized with dedicated wireless links based on onboard power. For the first time, a standardized clinical protocol has been recommended to guide the process of employing a fully insertable laparoscopic camera in a SILS procedure. Moreover, a custom Bluetooth low energy (BLE) application profile and a real-time operating system (RTOS) based multitask programming framework have been proposed for the sCAM, which could also provide a reference to facilitate embedded software design for other insertable medical devices. The whole design of the sCAM has been implemented using rapid prototyping technologies, characterized in terms of basic functions, and verified using a simulated human abdomen model, showing technical feasibility of an untethered fully insertable laparoscopic surgical camera.

Camera-Tissue Interaction Characterization and Force Sensing

The interaction between the rigid sCAM robot and the viscoelastic abdominal wall tissue is investigated. This camera-tissue interaction modeling sheds light on the relation between the tissue deformation and the stress distribution when the camera is in contact with the tissue. Integrating the stresses over the deformation profile, the camera-tissue interaction forces are mathematically calculated. Facilitated by the definition of a contact boundary condition, the tissue deformation profile has been further related to the camera-tissue interaction force. Moreover, a non-invasive indirect approach is proposed to provide real-time camera-tissue interaction force measurement, where the force sensors have been placed outside the patient's anatomy. Taking the force measurements as inputs, the camera-tissue interaction model generates not only the corresponding deformation profile but also the exact stress distribution. Ultimately, the recovered stresses provide feedback for camera force control and help improve laparoscopic surgical safety.

Pose Estimation, Visualization, and Feedback with sCAM

In order to actuate the camera precisely, the position and orientation of the camera are remotely estimated using a complementary filter (CF) assisted by a magnetic matching

process. An onboard 9-axis motion tracking device that combines a 3-axis gyroscope, a 3-axis accelerometer, and a 3-axis magnetometer senses raw motion information of the camera and provides inputs for the estimator. The software is implemented with three primary tasks: wireless sensor measurement acquisition, CF algorithm, and results visualization. The optimal estimation results provide feedback for closed-loop pose control of the sCAM and are also visualized using OpenGL rendering for the surgeon's reference. Unlike many others implicitly assuming that the camera is moving on a 2D horizontal plane [20][32], this approach requires few unrealistic kinematic assumptions on camera motion and tracks the camera in a practical 3D working scenario.

Robotic-Assisted Closed-Loop Laparoscopic Camera Control

Last but not least, robotic-assisted closed-loop camera control has been realized with the enabled force and pose feedbacks. A double-loop control scheme has been employed to enable surgeons to precisely control the surgical view without concerning that the camera might fall off or damage the tissue. The outer loop governs the camera pose according to the reference associated with the desired surgical view. Meanwhile, the inner loop takes care of the camera-tissue contact force with the concept of shared autonomy where free camera pose manipulation is allowed within a safe stress range. The safe stress range is predefined by tissue damage characterization and translated into pose limits online using the actuation model.

1.6 Dissertation Outline

The dissertation is organized as follows:

Chapter 2 elaborates the design and implementation of the sCAM robotic system in terms of hardware and software.

Chapter 3 presents approaches to untethered camera access including transabdominal camera actuation, wireless vision, wireless control and wireless power.

Chapter 4 introduces how the camera-tissue interaction is investigated as well as a non-invasive force measurement approach.

Chapter 5 reveals the remote pose estimation and visualization solution for the sCAM based on a complementary information fusing algorithm.

Chapter 6 details robotic-assisted control for the camera based on the state estimations from the Chapter 4 and Chapter 5.

Chapter 7 concludes the dissertation and shares some vision into the future.

Chapter 2

sCAM Robotic System

2.1 Introduction

As more benefits are being observed for patients with the emerging less invasive MIS techniques, one noteworthy problem is that the ease of operation for surgeons has also been further impaired by loss of triangulation and increase of clashing between surgical devices at the shared entry port. To meet these arising operational challenges, researchers and engineers have been working towards novel surgical devices or platforms [37][38][31][39][24][26][28][30] with improved ergonomics and flexibility. Among them, a most characteristic device required for LS is an laparoscope [40], which is an essential telescopic imaging equipment that allows viewing the inside surgical site from the outside. This device plays an irreplaceable role in laparoscopic surgical imaging, however, it makes the shared entry port more crowded for SILS and suffers from kinematic limitations due to the inherited trocar-based paradigm.

Evolution of laparoscope paradigms could be interpreted in terms of their dexterity and ease of manipulation as indicated in Fig. 2.1. Thanks to advances in biomechatronics, delicate mechanisms and robotic features are being integrated to improve the state of the art. The most conventional laparoscope [40] shown in Fig. 2.1(a) is a rigid slender stick with a trocar-confined 4-DoF workspace [41]. In order to obtain a larger field of observation, an articulating tip was introduced [42] [1] as indicated in Fig. 2.1(b). This improved design adds two degrees of articulation and subsequently enables full abdominal observation, although sometimes

[1] According to: http://medical.olympusamerica.com/products/laparoscopes/endoeye-flex-3d

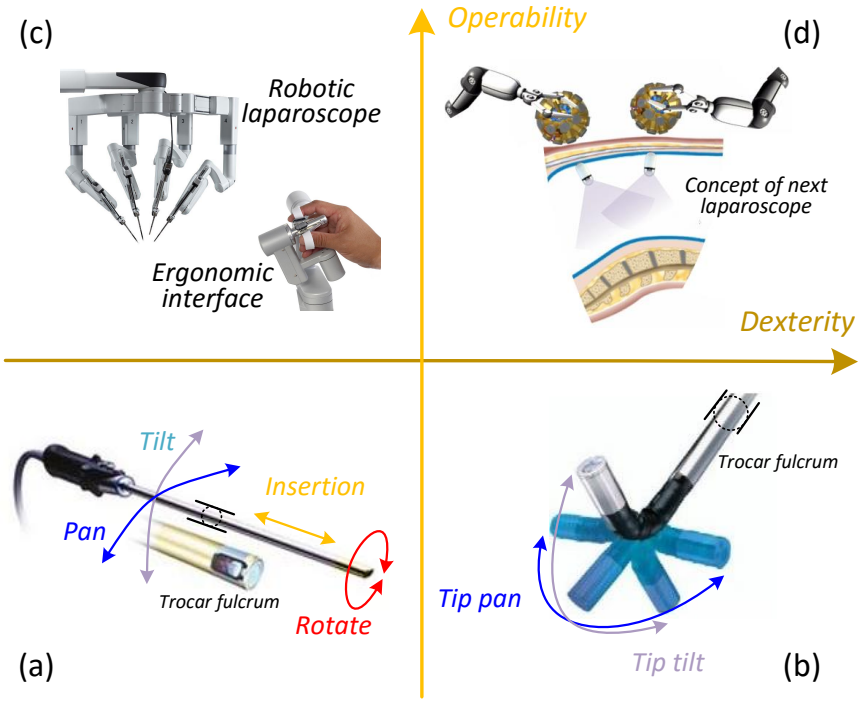

Figure 2.1: Laparoscope paradigm evolution in terms of operability and dexterity.

at an inferior angle of view. However, suffering from the trocar constraints, both of them significantly depend on *counter-intuitive* manual control and hand-eye coordination of a well-trained laparoscopist. That's why robotics has found its way into the operating room with its potential in improving surgical operability against the steep learning curve. Best manifested by the *da Vinci® Single-Site* surgical system presented in Fig. 2.1(c), robotic-assisted laparoscope has provided an intuitive surgeon interface with unprecedented ergonomics and precision. Unfortunately, due to inherent trocar channel constraints, movement of the long stick laparoscope is still confined to the same limited workspace as before. Occasionally, a second cut becomes inevitable for laparoscope replacement to get a preferred view angle, which may convert a SILS surgery to a MLS or even an open surgery [15][43]. Conclusively, current clinical state of laparoscopes leads to incisions, accounts for instrument clashing, and therefore is becoming a bottleneck of modern medical progress.

2.2 Platform Overview

2.2.1 Concept and Principle

Robotic-assisted medicine has been a clear future of modern medical science with an increasing series of robots dedicated for various diagnostic or operative procedures. Therefore, it's advisable to root the next-generation laparoscopic camera deep in robotics so as to carry forward precision and intuitiveness in surgical imaging. Following the evolution trending interpreted in Fig. 2.1, the next desirable generation of laparoscope should appear as Fig. 2.1(d) and be characterized by both dexterous mobility and intuitive operability.

Fig. 2.2 depicts the concept and working principle of the sCAM, which features a self-contained robotic laparoscopic imaging system that could either work independently in a diagnostic procedure or function as part of an integral robotic surgical system. The sCAM system consists of an insertable laparoscopic camera, an actuator held by a collaborative robotic arm, and an external control unit (ECU). The camera is completely inserted into the abdominal cavity, which makes more room in the SILS access port for other surgical instruments. Borrowing the principle of spherical motors, magnetic-based transabdominal

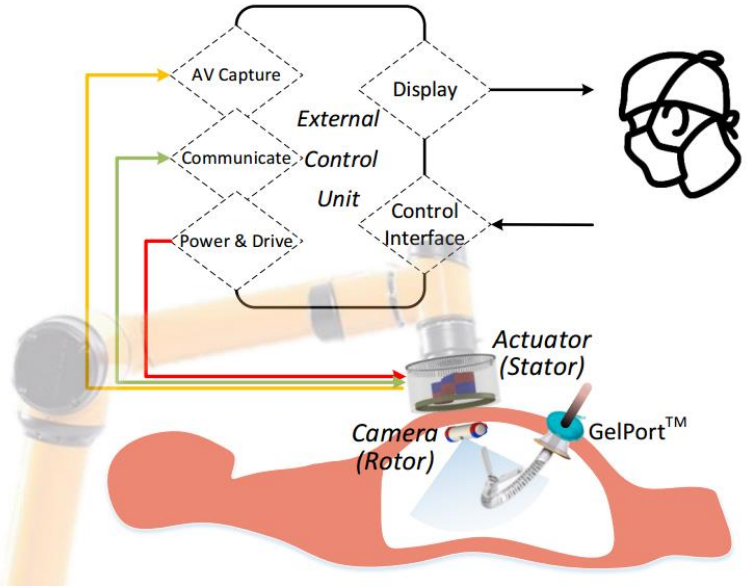

Figure 2.2: sCAM concept and working principle. [An AUBO-i5™ collaborative robotic arm, a continuum robotic manipulator (©2016 Titan Medical Inc.) and a GelPort® SILS access port (©2017 Applied Medical Resources Corporation) are included for technical reference.]

camera anchoring and actuation eliminate mechanical fixation and motorized actuation, thus laying foundation for flexible camera mobility. Laparoscopic audiovisual (AV) and control communications between the camera and the actuator are realized in wireless manners, which helps remove cumbersome tethering wires in other surgical instruments' way.

To integrate robotic merits into the sCAM system, the stator actuator is manipulated through a robotic arm controlled by the ECU. Although robotic manipulators have been seen in many surgical systems, few of them assign adequate emphasis on safety for either patients or surgeons, which unfortunately should be a major concern of surgical platforms. In the sCAM system, a collaborative lightweight robotic arm capable of force sensing and collision detection is adopted for manipulating the stator actuator, which not only provides robotic automation but also interacts safely side by side with surgeons. This robotic arm stops in milliseconds once an overload or collision event arises during operation, preventing potential injuries or accidents. By manually dragging the collaborative robotic arm, the surgeon could take control of the stator actuator anytime intraoperatively in case of an incident and reposition it arbitrarily to a desired safe pose, avoiding secondary harms. The arm will follow the dragging passively until automatic control is reenabled from the ECU.

The ECU is the control center of the sCAM system, serving as a bridge between the surgeon and the robotic camera. On the robotic camera side, the ECU controls the robotic arm to manipulate the actuator which finally drives the camera. At the same time, the ECU accesses AV signals from, communicates with and powers the actuator. On the surgeon's side, the ECU provides an ergonomic user interface for intuitive camera manipulation with real-time video display. In this way, behavior of the *in vivo* camera could be precisely controlled from a remote console. Meanwhile, the ECU could be integrated into existing robotic surgical systems in the operating room, immediately enabling the sCAM improvements for the state of the art.

2.2.2 Clinical Protocol

The availability and observation of a standardized protocol for robotic-assisted surgical procedures are of more significance than those for the traditional hand-operated practice due to the growing system complexity and technology intensity. A clinical protocol represents a

formal set of rules followed by the operating team to perform certain actions that lead to specific objective results. A well-devised protocol could be advantageous or even life-saving for patients in extreme cases. Usually it is considered to be stricter than a guideline and carry more weight with the law. When employing the sCAM in a SILS procedure, the following steps in Table 2.1 should navigate and regulate the process.

Table 2.1: Clinical protocol for SILS with sCAM

Step No.	Rules
Step 1	**Preparation of the procedure**
	Patient investigation
	sCAM setup
	Operating team knowledge
Step 2	**Access port introduction**
	Anesthesia
	Access port (GelPort®insertion)[1]
Step 3	**Instrument introduction**
	Optical cannula and manipulator cannula
	Pneumoperitoneum initiation
	sCAM camera introduction
	Surgical tools and additional cannulas
Step 4	**Exploration, operation, and retraction**
	Explore the anatomy
	Procedure-specific standard operation
	Cutting, dissection, and removal
Step 5	**Procedure closure**
	Remove tool under vision
	Retrieve sCAM camera
	Desufflation
	Remove access port
	Incision closure

[1] GelPort is used as the access port for SILS

Preparation for the procedure could start even more than eight hours before it is performed by preventing the patient from eating and drinking. Routine preoperative investigations in patients such as blood test, urinalysis, electrocardiogram (ECG), ultrasound image, CT scan, or MRI scan could be made per the doctor's request. In the operating room, besides standard preparation, the sCAM system needs to be properly set up to a ready-to-function status by a technician who is becoming more frequently involved owing to the increased technology intensity in robotic-assisted surgery. The operating team should also

be familiarized with general knowledge as well as primary principles of each device and get aware of their conditions prior to the operation.

General anesthesia should be preferably administrated although local anesthesia may be considered in some cases according to the surgery plan and the patient's condition. A keyhole incision varying in size with the access port (GelPort® 2.5cm 5cm, SILS™ Port 1.5cm 2cm) should be made in the belly button for better cosmetic results unless an effective view of the surgical site could only be established somewhere else on the anatomy. Introduction of the access port features particular folding and inserting techniques , where special attention and delicate operation should be used for appropriate port-tissue contact and pneumoperitoneum seal. Correct placement of the access port must be verified before further steps could be taken.

The instrument introduction step begins with insertion of a 5mm 12mm optical cannula and a 20mm working cannula. Pneumoperitoneum should then be initiated and maintained to create a working space in the abdominal cavity for viewing and operating. To introduce the sCAM camera, an articulating laparoscope is firstly introduced through the optical cannula for visual assistance. After that, a continuum robotic manipulator [44] [2] holding the sCAM camera will be guided into the insufflated abdominal cavity through the working cannula. Once magnetic coupling and wireless communication between the inserted camera and the actuator are confirmed, the continuum manipulator and the assistant articulating laparoscope will be removed in sequence. Surgical tools will then take these unoccupied cannulas and additional cannulas may be inserted or removed intraoperatively according to operational needs. Should the sCAM camera fall incidentally during the procedure, similar techniques using the assistant laparoscope and the continuum manipulator could take care of the situation to reengage or retrieve the camera.

The fourth step represents a set of procedure specific tasks and thus consists of multiple sub-steps which could be of dramatic differences from procedure to procedure. An exploration of the abdominal cavity is strongly encouraged before actual operations so as to avoid any misunderstanding of the patient's anatomy, particularly since flexible *in vivo* mobility of the robotic sCAM camera has granted a larger viewing space with

[2] According to: http://www.titanmedicalinc.com/technology/

improved intuitiveness and efficiency. Procedure specific sub-steps should strictly follow relevant standards if there exist, such as the critical view of safety (CVS) [45] concept for laparoscopic cholecystectomy, which could reduce the incidence of complication and increase the success rate. Before and after any cutting, dissection, and removal, the surgeon should double-check to exclude misidentification and confirm a clean retraction.

Finally, in step 5 the robotic-assisted procedure should be terminated in a safely planned process. Firstly, surgical tools and corresponding trocars should be removed under effective sCAM vision. Secondly, similar to its introduction process, the sCAM camera should be retrieved using the articulating laparoscope and the continuum robotic manipulator. The continuum manipulator and the articulating laparoscope will be sequentially removed afterwards. Next, the manipulator cannula is removed followed by desufflation via the laparoscope cannula. Then, the laparoscope cannula is also removed and the access port is taken out. Finally, it's mandatory to close the fascial incision carefully to prevent the development of a postoperative hernia. The fascia and the skin in the umbilicus should be infiltrated and sutured subcuticularly. Surgical tapes and bandages may be placed over the wound. The actuator is reusable after appropriate sterilization while the camera is disposable.

2.3 Hardware

A whole picture of the sCAM hardware is given in Fig. 2.3 in a schematic view, each part of which will be detailed in the following sections. Separated by the abdominal wall tissue, there exists no physical connection between the rotor/camera and the stator/actuator. Features supported by this hardware design include pan/tilt camera motion control, wireless stator-rotor control communication, wireless video streaming, as well as some reserved interfaces for manual manipulation and computer-assisted control. These features have been implemented and validated on the first prototype as a beginning, while more features have been enabled on a second prototype introduced in Section 2.5 to enhance the system capability.

sCAM (alpha 0.0) Features

1. Pan / Tilt control
2. Wireless stator-rotor communication
3. Wireless video streaming
4. *User interface*
   LEDs, buzzer, keys, joystick
5. PC (control station) interface

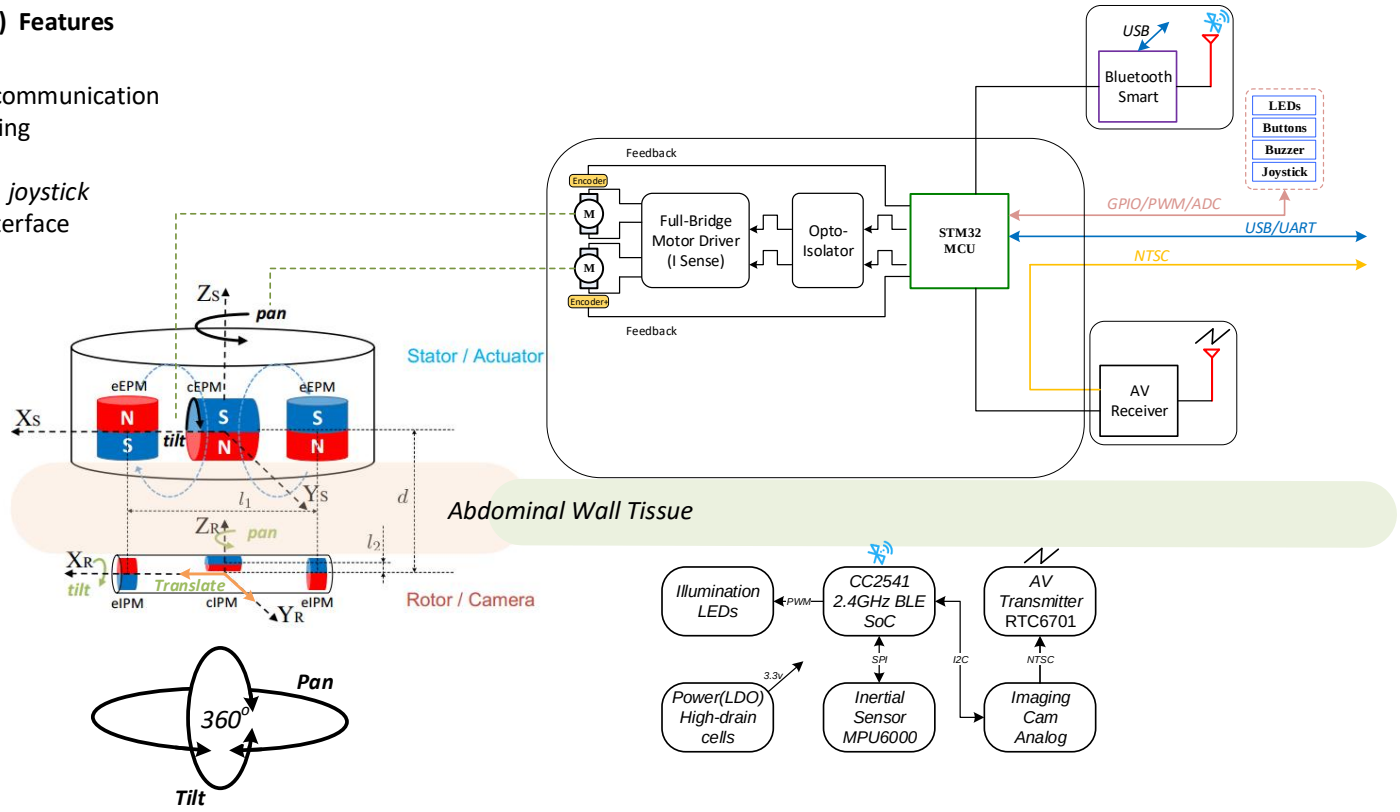

Figure 2.3: System schematic (i).

2.3.1 Mechanical Design

Rotor Design and Implementation

The *in vivo* camera traverses across the abdominal cavity against the interior abdominal wall and has been designed as the rotor. Fig 2.3 and Fig. 2.4 respectively present its magnetic schematic and mechanical implementation. Three diametrically magnetized IPMs have been integrated for actuation purpose. One cIPM is rigidly attached inside the camera body and moves with the camera as one piece. Meanwhile, two end internal permanent magnets (eIPMs) are fitted inside two end caps which are mounted at the camera ends through two bearings, as is shown in the implementation (Fig. 2.4). In this way, the camera would be able to tilt with respect to the eIPMs. Moreover, an oval window is opened sideways in the middle for camera view and illumination. Finally, the whole camera assembly has been encapsuled into a biocompatible transparent tube, which temporarily prevents the lens from getting blurred. The finished rotor profile resembles a cylinder of $\phi 16mm \times 81mm$ (refer to Table 2.2 and Table 2.3 for details). All electrical functional payloads and other onboard resources are housed inside the 3D printed biocompatible camera shell and will be detailed in Section 2.3.2.

Table 2.2: Physical attributes of the stator and the rotor

Symbol	Description	Value
Φ_s	Stator diameter	$120mm$
h_s	Stator height	$108mm$
m_s	Mass of stator	$762.3g$
Φ_r	Rotor/tube diameter	$16mm$[1]
l_r	Rotor length	$81mm$
ϕ_c	Camera body diameter	$12.5mm$
h_c	Camera body length	$68mm$
a	Window length	$16mm$
b	Window width	$10.8mm$
m_r	Mass of rotor	$37.5g$
l_1	eEPM/eEPM distance	$72.5mm$
l_2	cIPM offset	$4.35mm$
d	Stator-rotor distance	$variable$[2]

[1] Φ_r is being further reduced to around $10.5mm$
[2] Affected by the abdominal wall thickness [46]

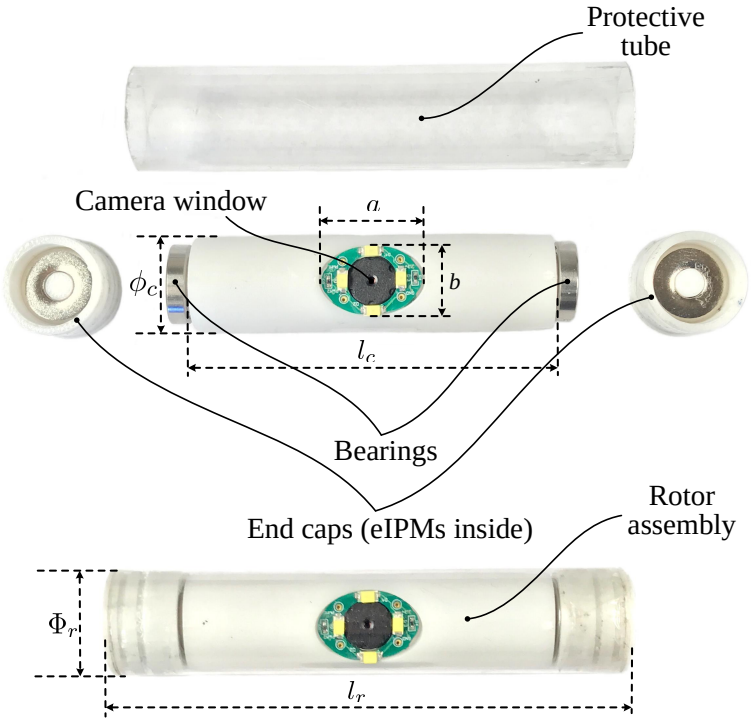

Figure 2.4: Mechanical design and implementation of the rotor.

Table 2.3: Physical attributes of magnets[1]

Magnets	**Outer diameter**	**Inner diameter**	**Hight**	**Mass**	**Grade**
eEPM(×2)	$25.4mm$	N/A	$25.4mm$	$96.5g$	$N52$
cEPM	$25.4mm$	$6.35mm$	$25.4mm$	$90.5g$	$N42$
eIPM(×2)	$12.7mm$	$4.76mm$	$6.35mm$	$5.19g$	$N42$
cIPM	$6.35mm$	N/A	$12.7mm$	$3.02g$	$N42$

[1] All are NdFeB based permanent magnets

Stator Design and Implementation

In order to anchor the camera for still imaging, translate and rotate it intraoperatively for a preferred perspective, the stator needs to generate controllable magnetic fields for camera actuation. Motor-driven permanent magnets have been adopted for this purpose since electromagnets have been proven prone to bulky volume and heat dissipation problems with coils [47]. As is schematically illustrated in Fig. 2.3, the stator has been equipped with three movable EPMs corresponding to the rotor IPMs. All EPMs could pan together about Z_S axis with respect to the stator housing. At the same time, the diametrically magnetized cEPM could tilt about X_S axis with respect to the axially magnetized end

external permanent magnets (eEPMs). The two eEPMs are installed in an opposite manner to make their magnetic fields cancel out in the middle around the cEPM as indicated by the blue dashed lines. This configuration minimizes additional forces and torques exerted on the cEPM by eEPMs which counteract tilt motion of the cEPM.

Mechanical implementation of the stator is also rapidly prototyped as shown in Fig. 2.5. Overall profile of the stator assembly is a cylinder of $\phi 120mm \times 108mm$. The stator core

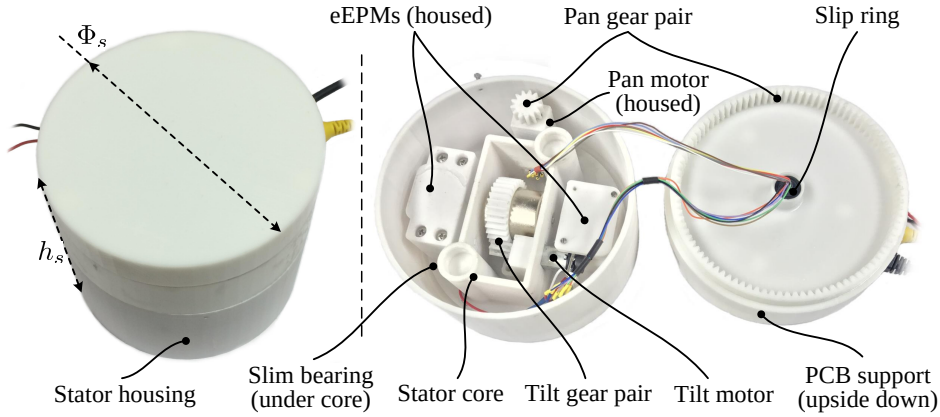

Figure 2.5: Mechanical design and implementation of the stator: the assembled stator profile (left) and its inside mechanism (right).

which carries all EPMs is fitted into the stator housing and seated on a thin slim angular contact ball bearing. Once installed, this bearing facilitates pan motion of all EPMs with respect to the stator housing. Meanwhile, the cEPM with a ring gear is installed on a shaft supported by the stator core and thus could rotate with respect to the eEPMs. Two DC servo motors are fixed on the stator core to respectively drive the pan and tilt rotations through gear pairs. After assembled, the printed circuit board (PCB) support will be bolted to the stator housing. Pan motion of the stator core is achieved through gear actuation between the pan motor gear and the inner gear in the PCB support while tilt driving is a straight-forward gear transmission from the tilt motor pinion gear to the cEPM ring gear. All electronic components which will be described in Section 2.3.2 sit on top of the PCB support and a 12-wire slip ring connector is utilized to prevent twisting of motor wires.

2.3.2 Electrical Design

Tethering wires are usually required for video transmission, control communication, and power supply for insertable laparoscopic cameras. Unfortunately, interference between these wires and other surgical instruments brings about additional operation restrictions and obstructs mobility of the camera. Furthermore, these wire bundles could be difficult to sanitize and thus increase the chance of patient infection. Therefore, tetherless design and implementation carry practical meaning in making insertable laparoscopic cameras more clinically acceptable. This section elaborates on the electronic solution which enables tetherless vision and control while contributing a fully functional sCAM hardware architecture.

System Architecture Overview

An architecture block diagram of the sCAM electronic system is provided in Fig. 2.6. Separated by the abdominal wall, the electronic system could also be divided into two parts: rotor camera and stator actuator. Although no physical connection exists in between, wireless control communication and video streaming have been established as indicated in the dashes rectangles.

Rotor/Camera Design and Implementation

As is interpreted in the lower part of Fig. 2.6, electronic system of the rotor camera is built around a cc2541 wireless microcontroller unit (MCU), a low-power system-on-ship (SoC) solution for bluetooth low energy (BLE) applications. This cc2541 not only facilitates wireless stator-rotor communication in the ISM band for camera control but also governs all other resources onboard the rotor camera. Images captured by the imaging sensor are fed into an AV transmitter and then sent out over an embedded antenna. The cc2541 configures and tunes the imaging sensor online with I2C protocol for better imaging performance. Illuminating LED lights are controlled by PWM signals generated by an on-chip timer of the cc2541. Moreover, the cc2541 has access to an inertial measurement unit (IMU) through an SPI interface for camera motion estimation. All the above components run on a $3.3v$

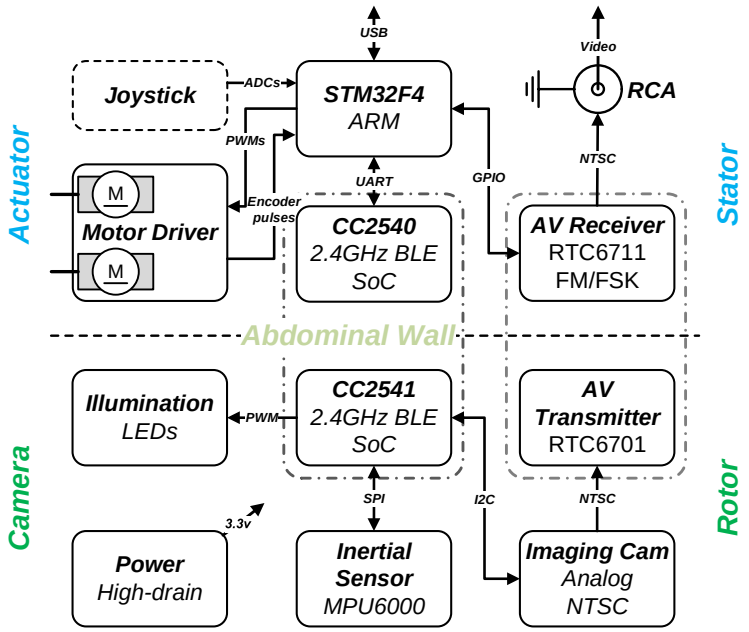

Figure 2.6: sCAM electronic system architecture block diagram (wireless links indicated in dashed rectangles).

voltage regulated from onboard high-drain batteries. Design and implementation of the rotor camera electronic system represent a most challenging part of this research work. All onboard resources need to be sealed inside a stringently limited space in an extremely low profile. As is preliminarily unveiled in [48] and implemented in Fig. 2.7, all camera payloads have been tailored into specific function modules. These modules are designed as round PCBs and stack up in the most space-efficient manner inside the camera, except for the imaging sensor and the illumination LEDs which are facing sideways and fitted in under the cIPM. Fabricated function modules and onboard power batteries are presented in a disassembled view of the camera in Fig. 2.7.

Wireless *MCU* Most of the processing and computational work will be fulfilled outside, therefore, not much processing power is required onboard. A lite programmable wireless *MCU* with basic on-chip peripherals will manage all onboard resources, and at the same time provide a wireless link for control communication. Although more tissue absorption could be caused by high carrier frequency, viability of $2.4GHz$ based Zigbee solution for GI tract physiological parameter monitoring had been verified in [49][50], providing feasibility evidence for this $2.4GHz$ *BLE* design. Thus, *TI* cc2541 stands out from many candidates for

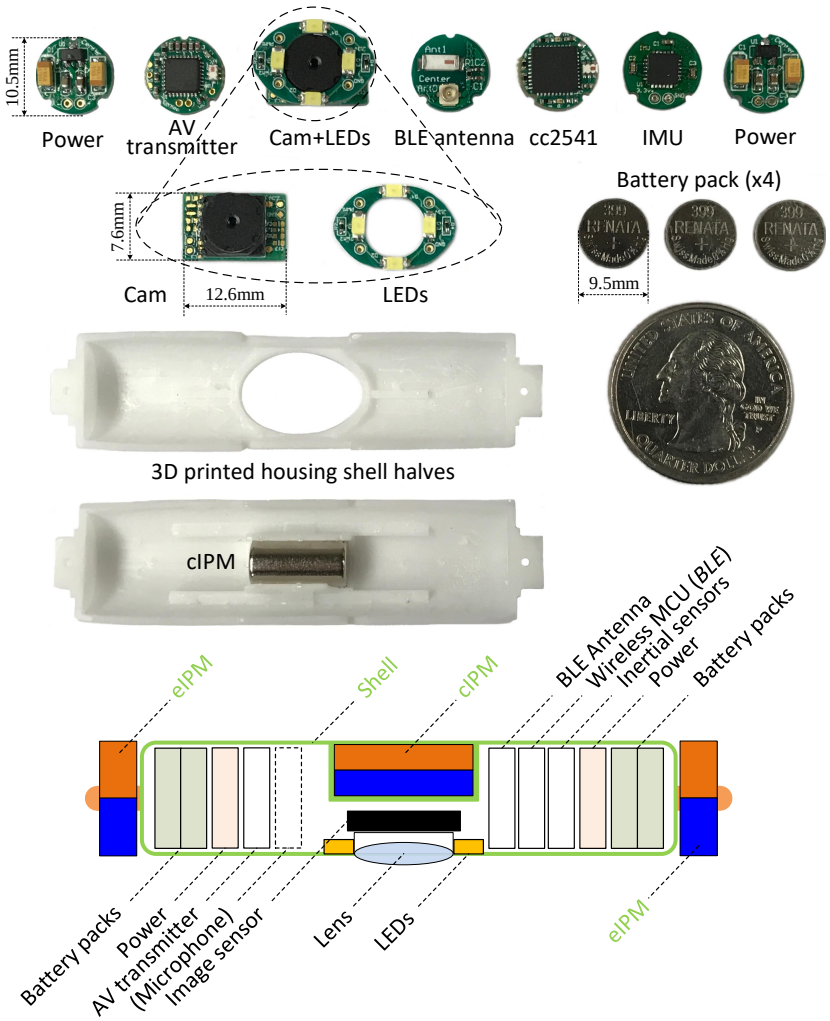

Figure 2.7: Implementation and layout of camera onboard modules (a microphone module is being integrated for audio feedback).

its proprietary merits as an *SoC* for *BLE* solutions. This wireless *MCU* has built a $2.4GHz$ *BLE* compliant RF transceiver and many other necessary peripherals around a low-power 8051 micro-controller core into a $6mm \times 6mm$ QFN package with at least $128KB$ in-system-programmable flash, which makes it an ideal choice for the central *MCU* of the camera hardware system. Moreover, there is a built-in temperature sensor and a battery monitoring circuit which could be configured as inputs for the built-in analog-to-digital converter (ADC) channels, thus enabling on-chip battery and temperature monitoring.

***BLE* Antenna** A 50Ω ceramic monopole chip antenna from Johanson Technology was adopted to match a front-end chip balun on the *BLE* module. Due to limited area on the *BLE* module, this antenna has been incorporated into a specific BLE antenna module as shown in Fig. 2.7.

Inertial Sensors Laying foundation for closed-loop camera motion control, inertial interface is a "must-have" function. The *MPU*-6000 digital motion processing unit from InvenSense with a built-in triple-axis gyro plus a triple-axis accelerometer in a $4 \times 4 \times 9mm$ QFN package had been chosen. One thing worth noticing is that an *MPU*-6000 on-chip temperature sensor could also be accessed by the cc2541 through *SPI* interface for more accurate system temperature estimation.

Imaging Digital imaging has many advantages in image-quality and post-process, however it challenges the design with high transmission bandwidth and power consumption, even after compression. An analog imaging sensor (ov7955, OmniVision®) has been chosen for its superior low-light sensitivity, small package ($5.7mm \times 5.4mm$), and most importantly, low transmission bandwidth and power consumption compared to digital imaging. This $1/3.7''$ CMOS sensor offers NTSC format video output with a 60^o field of view provided by a low-profile all-plastic aspheric lens (DSL756B, Sunnex®).

***AV* Transmitter** For the video transmitter module, an *rtc*6701 $2.4GHz$ *FM* transmitter for wireless camera has been chosen, as this device features modulation of both video and audio signals in a compact $5 \times 5mm$ QFN package. The *rtc*6701 has four transmission frequency channels and two output power levels which are all software configurable. A quarter wavelength wire antenna of $31mm$ was easily folded into the camera for this *AV* transmitter.

Smart Illumination Four high luminous flux LEDs from TOSHIBA have been placed on a circle uniformly at a 90^o interval as shown in Fig. 2.7. Each LED is of a low-profile $3.0\times1.4\times0.67mm$ size and generates $22.9lm$ flux at $65mA$ forward current. These LEDs have been configured into two parallel series to appropriately work with onboard batteries. Instead of simple on/off light control for most state-of-the-art insertable laparoscope prototypes, illumination level for this sCAM is arbitrarily adjustable from zero up to $91.6lm$ ($4\times22.9lm$), which enables active imaging light optimization. A simple condensing lens casting only 52% of the light onto the surgical site would meet the illumination design objective. Thus, a smart illumination strategy could be programmed to optimize power efficiency without a compromise on imaging performance.

Reliable Power Onboard power of this *in vivo* camera needs to be reliably safe. Twelve FDA approved high-drain batteries, each of which comes in a $\phi9.5\times2.7mm$ size with a capacity of 55mAh at $1.55v$, have been selected. Assembled into four parallel packs, a resultant power source of 220mAh at a $4.65v$ nominal voltage powers the entire camera electronic payloads. Meanwhile, two low-dropout (LDO) voltage regulators have been integrated for sufficient current supply of the $3.3v$ output, which powers most onboard electronics. The only exception is the LEDs which need to drain power directly from the batteries. According to electrical ratings of onboard modules, two power modules are required and the system could continuously operate in full for at least 50min, without any power optimization strategy.

Modular and Reconfigurable Design Hardware modularity and reconfigurability have been given special attention throughout design of the camera. Thus, these onboard camera modules could be easily interchanged for maintenance or reconfigured to build other insertable surgical devices dedicated for different purposes. For example, another rotor filled with batteries may be deployed alongside the camera rotor to extend camera working time, or an illumination specific rotor equipped with only batteries and LEDs could be introduced for better surgical illumination, to name just a few. As a result, a family of these insertable devices would be available to offer a systematical surgical solution in the future.

Other Onboard Sensing In addition to the mast-have imaging sensor, only a minimum amount of necessary sensing could be allowed onboard the camera. Battery health monitoring

is enabled by a simple voltage sampling circuit. Besides, a microphone module is being considered for intraoperative audio sensing which, as reported [51], plays a very helpful role in surgical perception.

Stator Actuator Design and Implementation

Different from design of the rotor camera electronic system which is restricted by multiple constraints, the stator actuator has a larger space and more resources available outside the patient. As is illustrated in the upper part of Fig. 2.6, electronic system of the stator actuator is centered at a 32-bit ARM Cortex-M4 microcontroller (STM32F4) . A cc2540 based BLE module is connected to the STM32F4 processor through an UART serial port to enable wireless control communication between the stator and the rotor. The STM32F4 could configure the AV receiver using GPIO pins for different operation frequencies of wireless AV transmission. Video received by the AV receiver could be accessed through an RCA connector by the control unit and then displayed for the surgeon's reference. Facilitated by a dual full-bridge motor driver, encoder signal measurement circuits, and motor current sensing, closed-loop control of the pan and tilt DC servo motors is programed with the STM32F4 processor, which enables precise and safe camera actuation. A two-axis joystick could be plugged on and connected to the analog to digital converter (ADC) of the STM32F4 processor. Thus, manual control of camera pan and tilt motion is also supported. In addition, a piezoelectric buzzer and several LEDs have been integrated to provide emergency alerts and warn surgeons of system status for safety concerns. Meanwhile, the stator actuator communicates with the control unit via a mini USB port.

Fig. 2.8 gives an explosive view of the stator actuator as well as a closeup of its electronic control system implementation. As is presented, the whole stator has been designed as a two-story ($\phi 120mm \times 108mm$, see Table 2.2) cylinder with a cap. The first story houses the stator actuation mechanism while the second story supports all electronic hardware. The cc2540 BLE module is designed as a USB dongle with a postage package for multiple purposes. It could be either soldered on the stator PCB for stator-rotor communication or plugged onto a computer for BLE development and debugging. The stator actuator is powered with an external $12v$ DC power supply. Meanwhile, protective photocouplers have

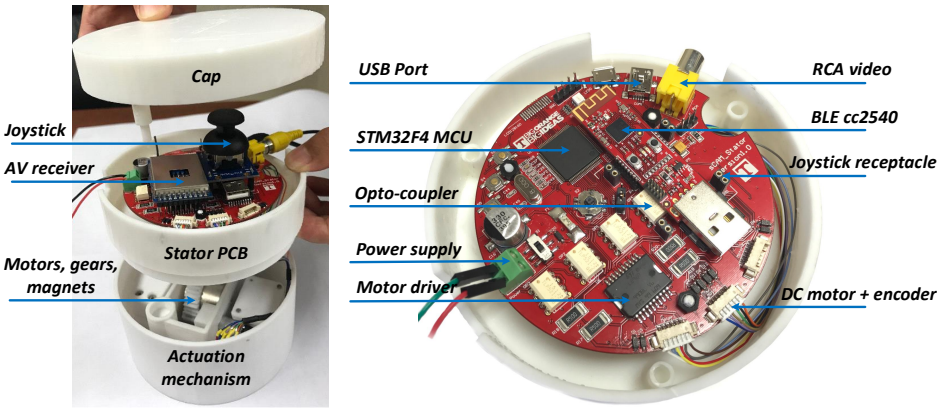

Figure 2.8: Implementation of the actuator electronic hardware.

been employed between logic circuits and high-power circuits to improve system reliability. In case of control failure of the ECU, a joystick could be plugged into the receptacle to enable manual steering of the camera, which helps make this sCAM fail-safe.

2.3.3 Experimental Validation

The feasibility of the hardware design has been validated by a series of function experiments. The illumination tests are presented in this section while more validation tests are presented in Chapter 3.

Illumination tests were performed outside the synthetic abdomen model using an adjustable frame built with the t-slotted 80/20 aluminum structural material as shown in Fig. 2.9. The LED illumination module was hovering right above a 30cm×30cm square plane which was divided into 100 small squares of 3cm×3cm. The distance between the illumination module and the square plane was adjusted to 5cm, 10cm, 15cm, and 20cm respectively for 4 tests. Each test was repeated 3 times and averaged illumination level of each small square was recorded using the LED light meter (Extech LT40). All tests were carried out at night in a natural dark environment and the LEDs were fully lit with a PWM of 255.

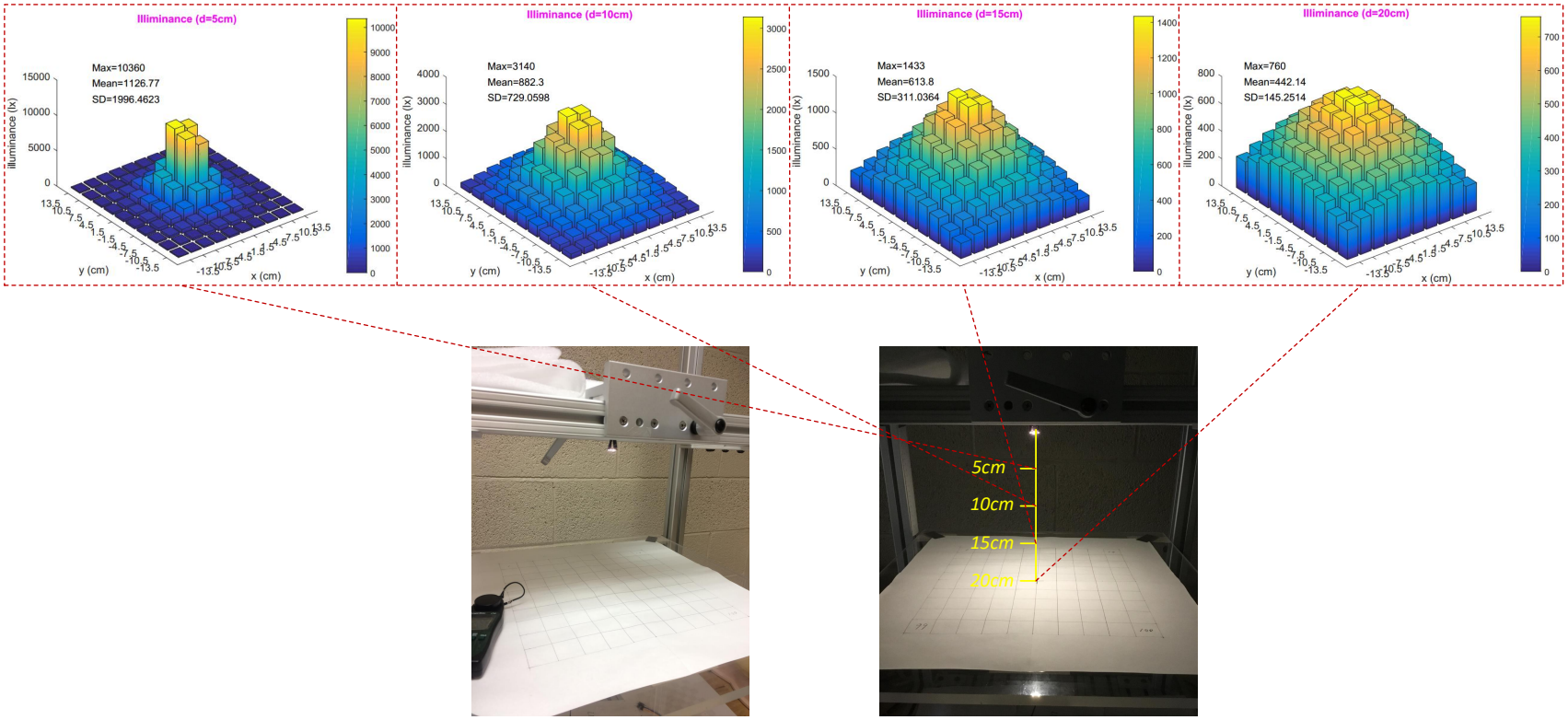

Figure 2.9: Illuminance test.

Experimental results at different distances were visualized using 3D bar graphs in Fig. 2.9, which unveiled radiation and distribution properties of the LED illumination module. High illumination levels were all in the center of the plane for each test with the highest of 10360lx seen in the 5cm test. As the testing plane moved away from the LED module, illumination levels decreased and light flux became more evenly distributed. This is reasonable since the radiation pattern of the LED module resembles a semi-sphere facing the testing plane. More illumination flux will fall on the testing plane at a closer distance. Meanwhile, the center of the testing plane is nearer to the illumination module compared to its surrounding areas, thus more luminous flux will fall in this area. Also, the further the testing plane moves, the smaller the distance difference becomes between the center and the surrounding areas, which results in lower standard deviations.

The lowest mean illumination level was 442.14lx with the 20cm test, which still facilitates acceptable imaging performance according to the tetherless laparoscopic vision test in Section 3.3. This exceptional low-light performance should be attributed to the high sensitivity of the imaging sensor. Moreover, it's worth noting that the laparoscopic camera is usually hovering around 10cm above a surgical area no larger than 15cm×15cm in clinical practice, where sufficient illumination with a mean level of 1983lx could be provided according to the experiment results.

2.4 Software

2.4.1 sCAM BLE Profile

Bluetooth low energy (BLE, marketed as Bluetooth Smart) is part of the Bluetooth 4.0 standard targeting wireless healthcare and other applications with low-power, low-latency, and low-throughput features. Frequency hopping among 40 channels defined by the Bluetooth protocol counteracts RF interference and guarantees connection reliability. As a member of the Bluetooth Special Interest Group (BT-SIG), TI has designed and provided their BLE stack and cc254x series wireless SoCs for BLE user application development. Assisted by the TI BLE-Stack, a generic attribute profile (GATT) based proprietary sCAM

application profile has been developed for stator-rotor wireless communication and camera control.

As is shown in Fig. 2.10, a central-peripheral role configuration is adopted for stator-rotor BLE connection. The cc2540 onboard the stator is programmed as an sCAMCentral master while the cc2541 onboard the rotor works as an sCAMPeripheral slave. Once powered on,

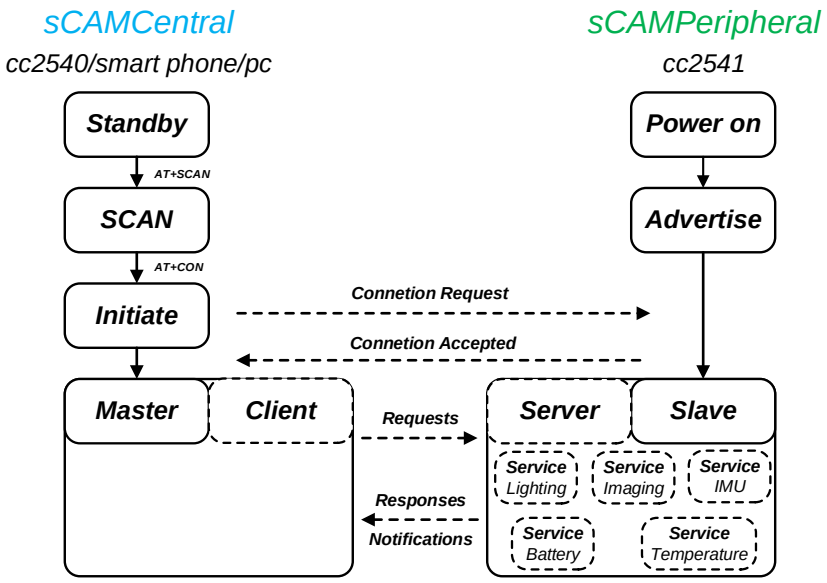

Figure 2.10: sCAM BLE profile and application flow chart.

the peripheral device will periodically broadcast advertisements until a connection request is received from the central device. The central device is managed by the STM32F4 through an UART serial port using AT commands as is illustrated in Fig. 2.6 and Fig. 2.10. The sCAMCentral will initiate a connection request to the sCAMPeripheral when the peripheral device is found. If the request is successfully accepted, connection between sCAMCentral and sCAMPeripheral will be established after a mutual parameter update. Once connected, the master works as a data client while the slave works as a data server. The sCAMPeripheral provides services related to camera onboard resources including lighting, imaging, IMU, temperature and battery. The sCAMCentral requests these services so as to realize wireless control of the camera. More meaningfully, more than one sCAMPeripheral slave could be connected to the sCAMCertral master to form a star topology multi-camera network, drastically augmenting the system capabilities.

2.4.2 Real-Time Software Framework

An embedded real-time operating system (RTOS) needs to be chosen for this medical device for the following reasons. First, as one may realize from the system architecture diagram of Fig. 2.6, most low-level control and processing algorithms are being executed on the STM32F4 ARM processor, which is too complex to be implemented just in one simple programming loop. Second, processing time matters particularly for this safety-critical application and failure of timely event response may cause serious medical disasters. Third, application programming and debugging on a bare MCU is time consuming, error prone, and code inefficient. An RTOS supports multitasking, is time sensitive, and more meaningfully, bounds event responses within fixed time constraints. Meanwhile, the operating system encapsulates hardware resources into system services and APIs to expedite software programming.

μC/OS-II from Micrium® (acquired by Silicon Labs® in 2016) is a lightweight scalable embedded RTOS which features industrial level reliability and application efficiency. Most importantly, μC/OS-II has been verified on many hospital devices used solely by medical professionals, which all have met medical software safety certification standard (IEC 62304) and received FDA (501k) clearance. The event based preemptive multitasking kernel of μC/OS-II could schedule up to 256 tasks in real time according to their statuses and priorities. As is shown is Fig. 2.11, standing on top of the hardware abstract layer (HAL), the RTOS manages all on-chip and onboard resources. Facilitated by the multitasking kernel, different functions of the sCAM have been designed as individual tasks sharing the MCU resources in a harmonic manner and more tasks could be added easily in future when necessary. Currently, six tasks have been developed to fulfill all sCAM functions: BLE communication task, USB communication task, joystick input processing task, AV receiver configuration task, closed-loop DC motor control task as well as LED & Buzzer task. Each task has been assigned a different priority and the RTOS kernel guarantees that the ready task with the highest priority always gets executed. By delicate priority assignment and task loop design, all tasks run on the RTOS reliably and efficiently as if every task has its own

CPU. Above all, real-time event response and processing within a fixed time have guaranteed reliability and safety of the sCAM.

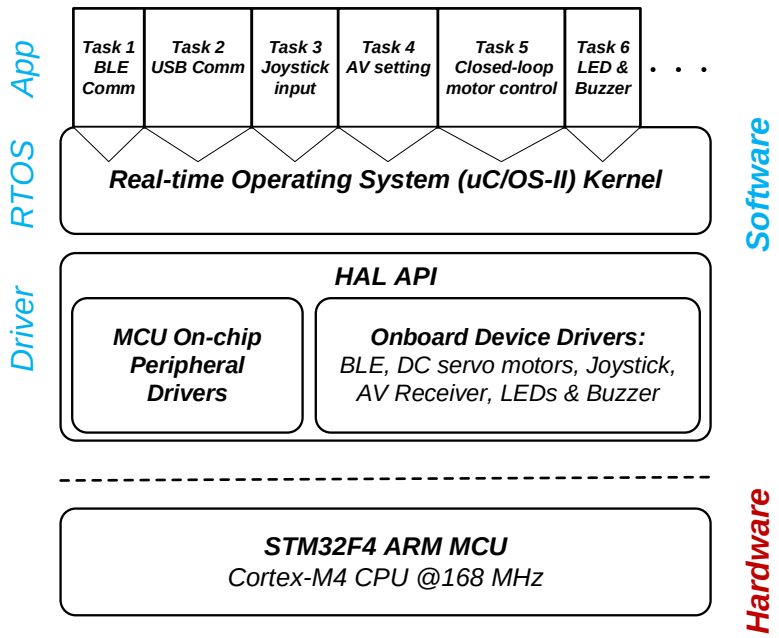

Figure 2.11: Real-time operating system based software framework.

2.4.3 Experimental Validation

Six user tasks were running on the μC/OS-II embedded real-time operating system as developed in Section 2.4.2. Each task was programmed as an infinite loop with a unique priority and an appropriate delay time, which were assigned as Table 2.4. The smaller the number, the higher the task priority. Each task delays itself an appropriate time periodically so that tasks with lower priorities could also get executed. System tick clock was set at 1KHz for the RTOS and task event response within 1ms was ensured for the ready task with the highest priority. USB communication with the ECU was using the interrupt service. In this way, orders from the control unit could be taken care of in microseconds. CPU usage was about 3%~5% when all tasks were in full operation, which indicates there exists a great processing potential for more tasks.

Table 2.4: Task priorities and delay times

Tasks	**Priority**	**Delay Time**(ms)
BLE Comm	4	50
USB Comm (Int.)	5	50
Joystick Input	6	50
AV Setting	7	50
Motor control	8	20
LED & Buzzer	9	50

2.5 Prototype II

A second prototype has been developed and implemented with the following optimization and improvements as is indicated by comparing the system architecture diagrams in Fig. 2.12 and Fig. 2.3.

First, in order to support force measurement, three force sensors have been incorporated into the stator, which were used to measure the camera-tissue interaction forces as detailed in Chapter 4. *Second*, aiming to extend the battery life or even completely eliminate onboard batteries, a wireless power transmission circuit was integrated on the stator with a transmitting coil. Accordingly, a receiving coil was fitted onboard the camera to pick up power from the resonated electromagnetic field. *Third*, the pan motor is removed on prototype II, since the actuator is held by a robotic arm during application and the pan motion could be taken care of by the last joint of the robotic arm. This change also reduces the mechanical complexity of the stator and results in a smaller size. *Forth*, a CAN bus interface is integrated on the second prototype so that control of the actuator could be easily incorporated into the robotic arm controller. *Fifth*, an MPU-9250 which consists of a triple-axis accelerometer, a triple-axis gyro, and a triple-axis magnetometer replaces the MPU-6000 to enable magnetic field strength measurement. *Finally*, an optimization has been made for the camera profile compared to the first prototype. The ends of the second camera prototype are semi-spheres, which provides better camera-tissue interaction smoothness.

sCAM (alpha 1.0) Features

1. Pan / Tilt control
2. Camera-tissue contact force estimation
3. Remote camera pose estimation
4. Wireless power transmission
5. Wireless stator-rotor communication
6. Wireless video streaming
7. User interface
8. PC (control station) interface

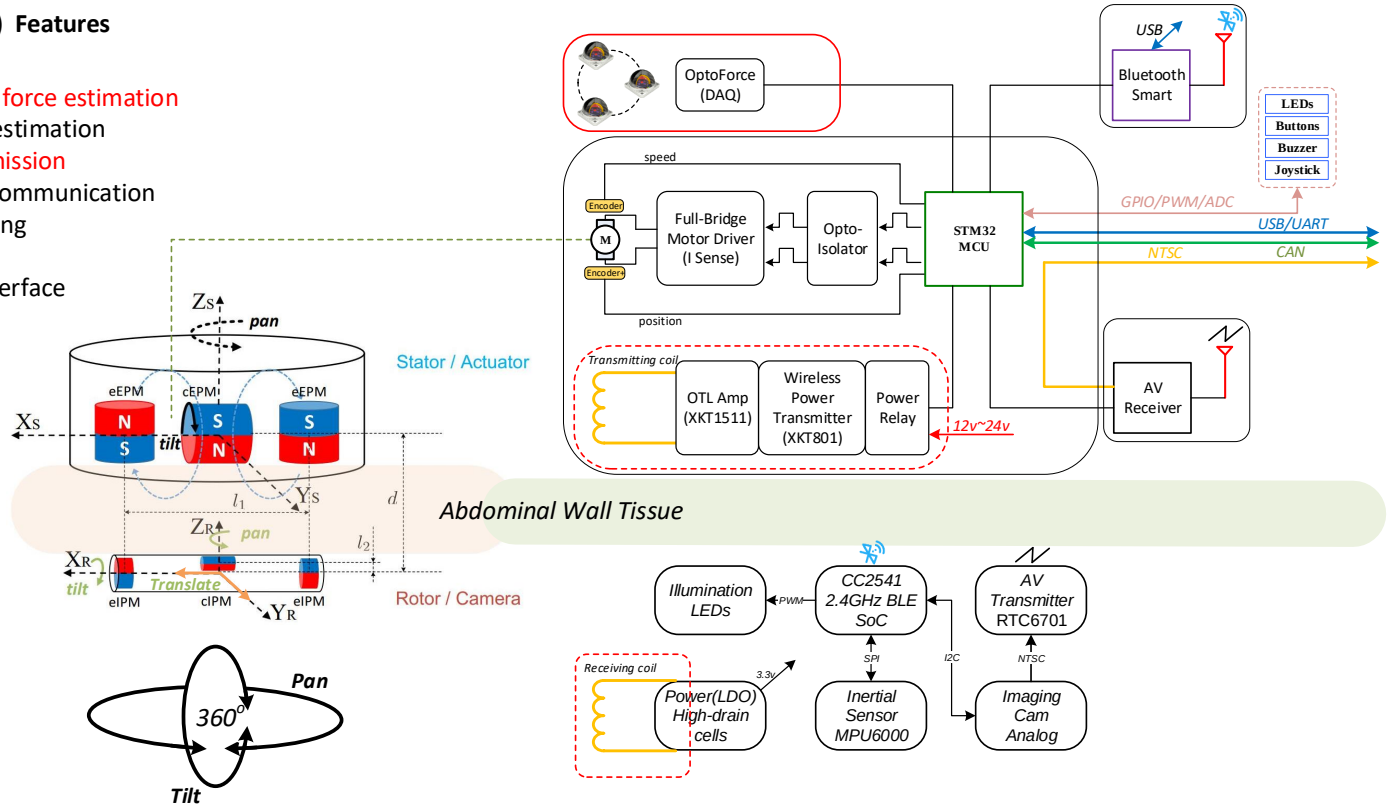

Figure 2.12: System schematic (ii).

The fabricated prototype II using rapid prototyping technology is shown in Fig. 2.14. The mechanical parts of the actuator and the camera were 3D printed with biocompatible resin which has been proven safe for surgical use. The force sensor base is made of aluminium alloy and fastened on the hanger using nonmagnetic screws so that no magnetic attraction exists between the stator and the hanger and the camera-tissue contact force measurement is not contaminated. Fig. 2.13 presents the stator controller circuit board with the feature interfaces, which is fitted into the actuator hanger.

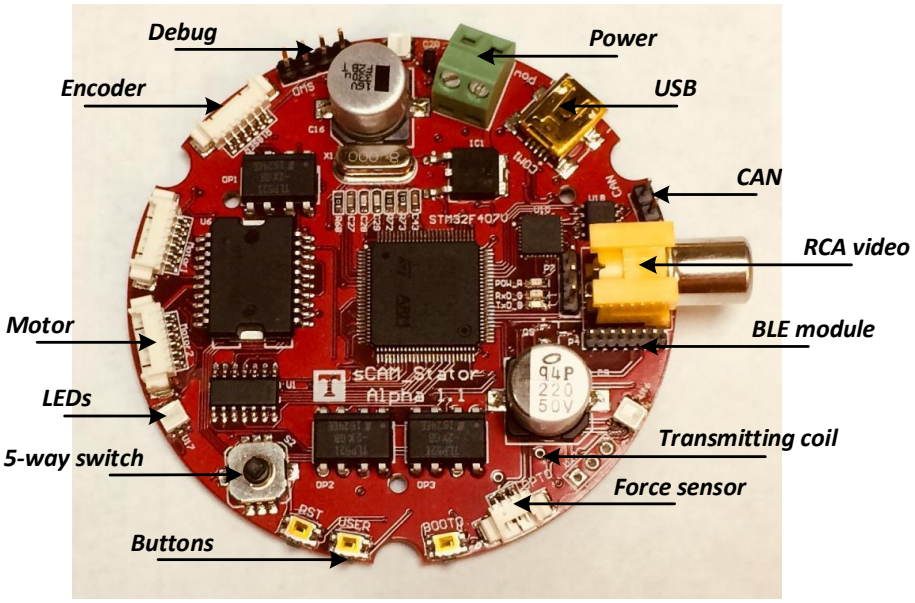

Figure 2.13: Stator controller of the second prototype.

Based on these two proof-of-concept prototype designs and implementations, untethered camera access and results are revealed in Chapter 3 while the force measurement approach and experiments are detailed in Chapter 4.

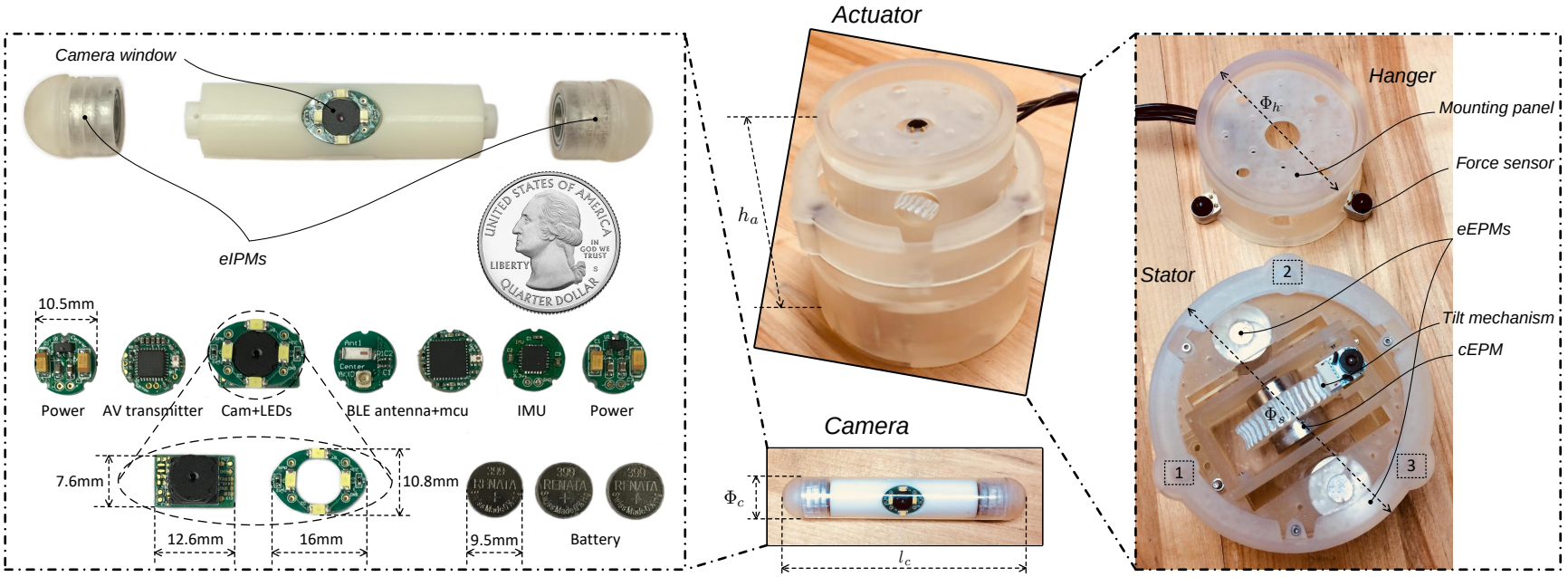

Figure 2.14: Prototype II.

2.6 Summary

This chapter introduces the medical rationale and clinical protocol of the sCAM robotic system. Design and implementation of the sCAM prototypes have been detailed in terms of both hardware and software. The hardware architecture supports transabdominal magnetic camera actuation, wireless video streaming, wireless control communication, camera-tissue interaction force measurement, and remote camera pose estimation. Two prototypes have been fabricated using rapid prototyping technologies and tested in an *ex vivo* environment. Basic function experimental results have shown feasibility of an untethered fully insertable laparoscopic surgical camera which completely eliminate cumbersome tethering wires and lays foundation for more dexterous camera mobility and intuitive camera control. Meanwhile, the hardware and software frameworks provide a technology reference for development of more insertable medical devices in future.

Chapter 3

Untethered Camera Access

3.1 Introduction

The field of insertable laparoscopic robotic camera is gaining increasing attentions from researchers, surgeons, and also patients. So far, exploring steps have been taken towards eliminating mechanical linkages and physical tethering for insertable laparoscopic cameras. Unfortunately, each solution was only able to partially meet the non-contact actuation or tetherless control expectation, a tetherless insertable laparoscopic camera with flexible *in vivo* mobility under non-fixated actuation remains beyond the state of the art. Particularly, operational interference caused by tethering wires has been recognized as a common drawback of current prototypes [20][11]. As is reported by studies [20][35][36], increasing the number of wires in the tether reduces its overall flexibility and thus affects mobility of the *tethered* camera.

This chapter elaborates on how the untethered access to the *in vivo* camera is achieved in terms of transabdominal camera actuation, wireless vision and control, and wireless power. Inspired by the principle of spherical motors, multi-axis camera rotation has been provided with a compact magnetic joint. Tethering wires required for video transmission, control communication, and powering have been removed by wireless vision transmission and control communication based on onboard power. Hence, camera mobility has been improved and operational interference has been reduced.

3.2 Transabdominal Camera Actuation

The sCAM robotic camera targets non-contact actuation which means there exists neither physical linkages between the camera and the driving components nor mechanical fixture of the camera to the abdominal wall. Furthermore, no power-consuming motors could be allowed onboard the camera so as to reduce its mechanical complexity and extend battery life. Hence, inspired by the principle of spherical motors which enables multi-axis rotor rotation with one compact magnetic rolling joint [52], actuation of this camera is realized in a variant non-contact stator-rotor manner as is schematically illustrated in Fig. 3.1. Permanent magnets on the stator could be operated by motors to generate controllable rotating magnetic fields. Thus, adjustable tightly coupled magnetic attraction between the stator (actuator) and the rotor (camera) provides manipulating forces and torques for driving this *in vivo* camera. Pan, tilt, translation as well as anchoring of the camera are all enabled by actively generating desired driving magnetic fields in accordance to the camera pose.

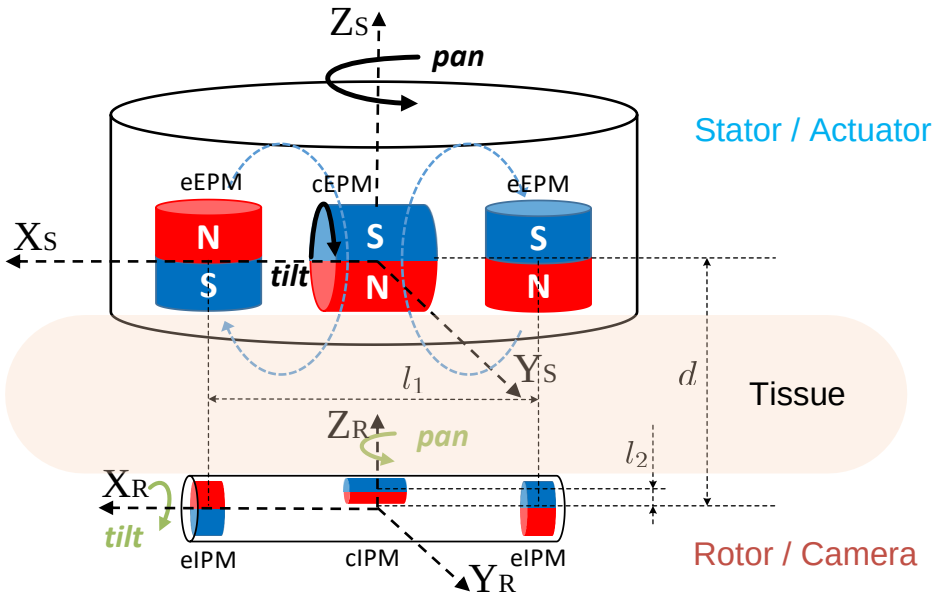

Figure 3.1: Magnetic-based stator-rotor actuation mechanism. $X_S Y_S Z_S$ is the stator coordinate frame and $X_R Y_R Z_R$ is the rotor coordinate frame.

3.2.1 Multi-DoF Decoupled Camera Mobility

Although an insertable camera levitated freely inside the abdominal cavity with 6 DoFs would be ideal for practice, design complexity and MIS restrictions have made that a quite challenging objective at this moment. However, to meet the SILS imaging expectation of observing the whole abdominal cavity flexibly from any desired position and angle over the surgical site, 4 DoFs in camera mobility would be sufficient. 2D translation along the abdominal wall moves the camera to the desired position while 2D rotation directs the camera in the desired perspective. These locomotion DoFs are decoupled from each other by design to simplify kinematic modeling and control of the camera. At the same time, since camera movement perpendicular to the abdominal wall is small and does not contribute much to its workspace, it's reasonable to make a weak assumption that curvature and deformation of the abdominal wall are negligible in the following mobility analysis. However, special attentions to these effects would be essential for camera-tissue interaction force analysis and control, which will be fulfilled in the future.

3.2.2 Anchoring and Translation

Anchoring of the camera is supported jointly by magnetic attraction forces between all external permanent magnets (EPMs) and internal permanent magnets (IPMs). Moreover, facilitated by these attraction forces, the camera could be translated along X_R and Y_R axes by moving the stator in corresponding directions. In this way, the sCAM system obtains the capability to reposition and secure the inserted camera to a desired position intraoperatively and efficiently without causing additional injury. It's also worth noting that in order to anchor the camera safely and reliably against the interior abdominal wall, an appropriate camera-tissue contact force should be maintained so that the camera will neither fall off nor damage tissues.

3.2.3 Pan and Tilt

An effective and comfortable view of the surgical site plays a critical part for SILS efficiency and safety. It's not only the position but also the orientation of the camera that determines

the resultant surgical view. As is shown in Fig. 3.1, the camera could pan about Z_R axis enabled by the rotation of the stator core carrying all EPMs. Meanwhile, tilt motion of the camera about X_R axis is achieved by magnetic coupling between the central internal permanent magnet (cIPM) and the central external permanent magnet (cEPM). In this way, rotational motion of the camera has been decoupled and orientation control could be simplified. Theoretically, these pan and tilt DoFs have potential to point the camera to any desired direction in a spherical space centered at the camera position as shown in Fig. 3.2. As a result, this sCAM system enables multi-quadrant omnidirectional *in vivo* laparoscopic imaging with 4 decoupled DoFs.

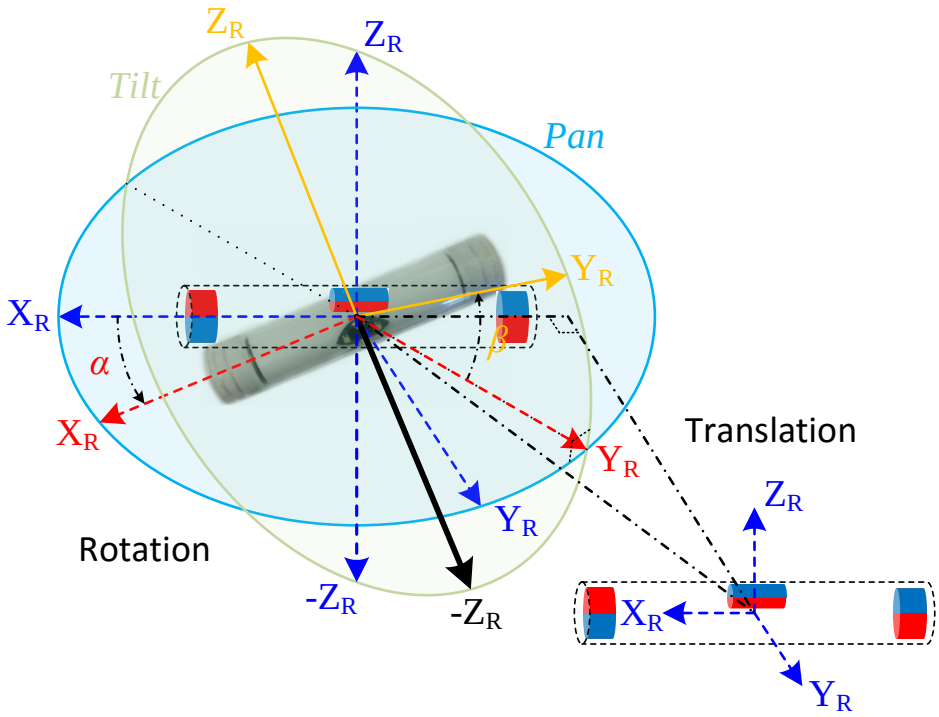

Figure 3.2: Camera mobility interpretation. Translation along X_R and Y_R could reposition the camera while viewing direction $(-Z_R)$ could be reoriented by pan (α) and tilt (β) rotation.

3.2.4 Experimental Validation

Experimental tests of sCAM functions have been performed *ex vivo* using a 3-Dmed® simulation human abdomen model in order to evaluate the sCAM performance and verify

design feasibility. Wall thickness of the abdomen model is about 30mm which, according to studies [46][53], represents an average value of human abdominal wall thickness. As is shown in Fig. 3.3, the synthetic abdomen model was laid on a horizontal workbench while the stator was placed right over the abdomen and the rotor camera was introduced into the abdominal cavity through an opening on the model. Magnetic coupling between the rotor camera and the stator actuator was established under direct visual assistance for now and the rotor camera was anchored against the interior abdominal wall. Vision and control of the camera were using wireless communications between the stator and the rotor. The stator ran on a $12v$ DC power supply and communicated with the ECU (a windows PC) through a USB cable. Meanwhile, video signals were output to the ECU using a coaxial composite video cable as seen in Fig. 3.3.

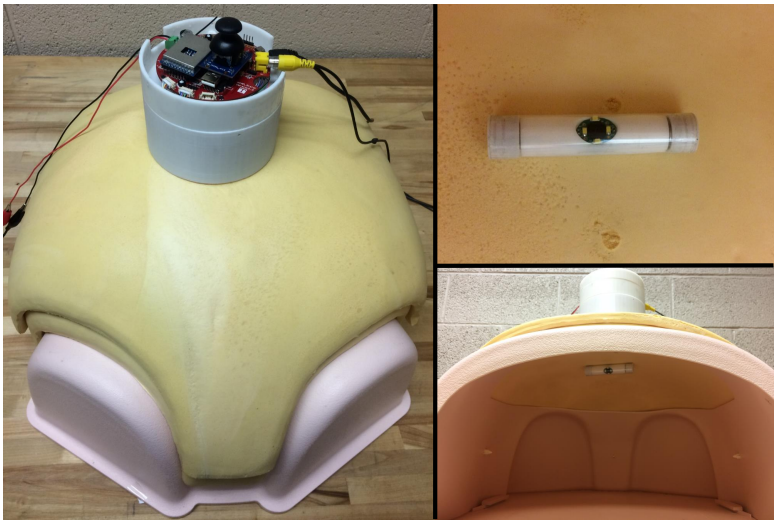

Figure 3.3: *Ex vivo* experiment setup in a 3-Dmed® synthetic abdomen model.

Since our goal was to verify the stator-rotor actuation and camera mobility, the robotic arm was not integrated for now in order to simplify the experiment setup. Multi-DoF camera mobility was tested using the same setup as Fig. 3.3 by manually manipulating the stator actuator. Translation of the camera was tested by moving the stator over the surface of the abdomen model while pan and tilt of the camera were tested by manipulating the joystick.

Thanks to the non-contact actuation and teteherless control, dexterous camera mobility was observed in the test results. Translation of the camera could reach multiple quadrants inside the abdomen model as shown in Fig. 3.4. Pan motion range of the camera was 0^{o}~360^{o}

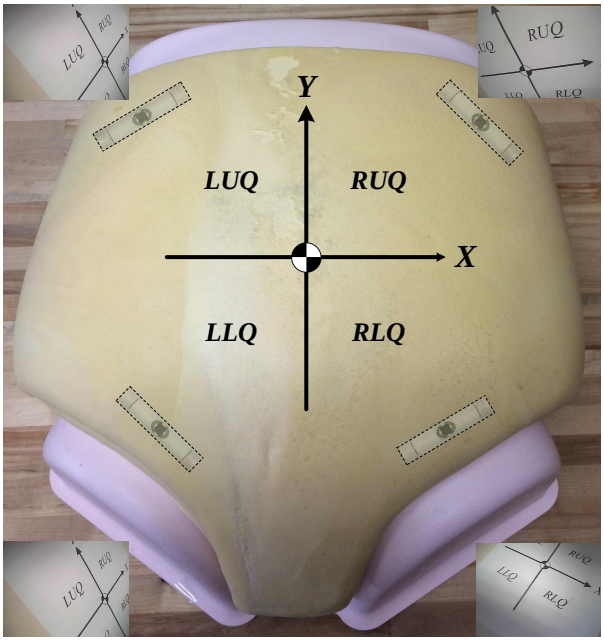

Figure 3.4: Translation of the camera. A multi-quadrant coordinate frame was placed in the belly for imaging reference. Left upper quadrant (LUQ), left lower quadrant (LLQ), right upper quadrant (RUQ), right lower quadrant (RLQ).

as is demonstrated in Fig. 3.5. Results also confirmed that the camera could tilt between -180° and +180°. However, it's worth noting that the camera only needs to tilt between -60° and +60° in clinical practice. As is illustrated in Fig. 3.6, the camera has a 60° field of view which could provide a view scope of ±90° aided by a ±60° tilt angle, sufficient for the camera to observe the whole abdominal cavity in the tilt DoF.

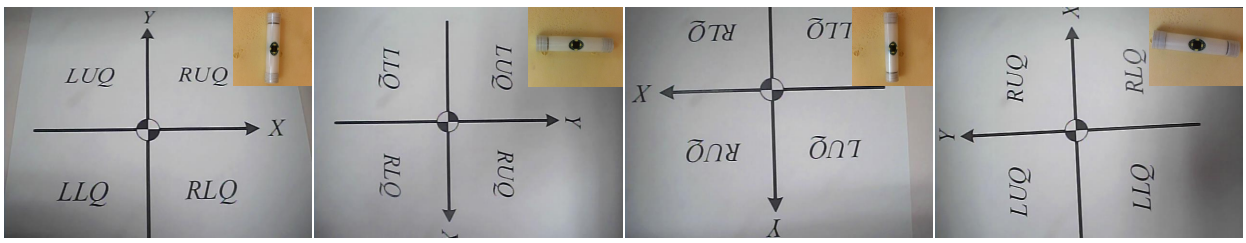

Figure 3.5: Pan motion of the camera. A top-right inset indicated the camera pose.

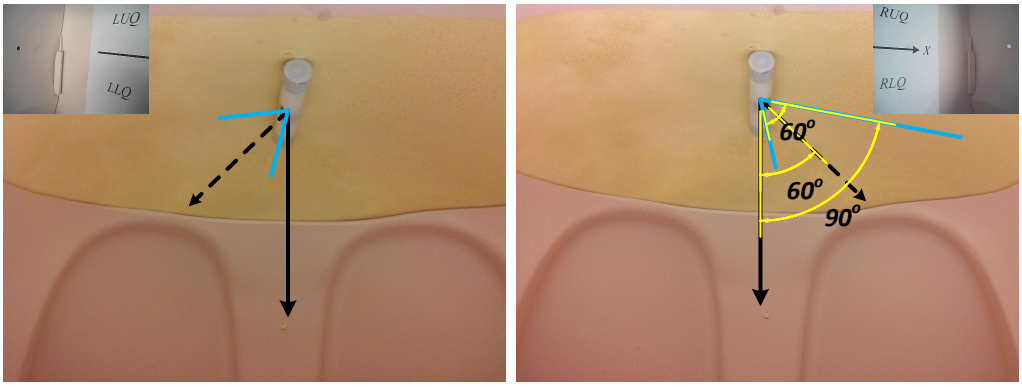

Figure 3.6: Tilt motion of the camera. A resultant tilt observation range angle of $\pm 90^{o}$ was achieved.

3.3 Wireless Vision and Control

In order to realize wireless laparoscopic vision, the first choice to make is the imaging sensor. Although digital imaging has many advantages in terms of image-quality and post-process, however it challenges the design with high transmission bandwidth and power consumption, even after image compression. Thus, an analog CMOS imaging sensor (OV7955) with NTSC format video output has been chosen for its high sensitivity and low bandwidth and power requirements.

A 2.4 GHz AV transmitter with an analog FM modulator and a $+12dBm$ power amplifier transmits video signals from the camera. At the RF front end of the transmitter, a quarter wave folded wire antenna of $31.25mm$ ($\lambda/4 = 4c/f$) is connected for maximum radiation efficiency and minimum space consumption. Accordingly, the external AV receiver on the stator is equipped with a compatible antenna for maximum receiving sensitivity. Moreover, the AV transmitter is capable of stereo audio modulation. Thus, *in situ* audio feedback from the remote surgical environment will be available once an audio sensor gets integrated.

Wireless camera control is realized through 2.4 GHz BLE communication between the cc2540/1 BLE modules. A miniature ceramic monopole chip antenna (2450AT42A100, Johanson Technology®) is chosen for the cc2541 module onboard the camera due to the limited space while a microstrip antenna is adopted for the cc2540 module onboard the stator. Software development of a customized BLE application profile specifically for this sCAM is detailed in Section 2.4.1. Although more tissue absorption may be seen for higher

carrier frequencies, viability of 2.4 GHz ISM band based wireless physiological telemetry had been verified in [50], which provides feasibility grounds for our wireless vision and control solution.

3.3.1 Experimental Validation

Wireless Vision Tests

The experiment setting is the same as that of the camera actuation as is show in Fig. 4.19. Wireless video received by the AV receiver on the stator was output to a video to usb converter (DFG/USB2pro) which connects to the ECU. Received video streams could be displayed, processed, and stored using the monitoring software and development APIs provided with the converter. As is shown in Fig. 3.7, two experiments have been performed in order to evaluate the wireless imaging performance. First, a SIMULAB Peg Transfer Board with colored triangles was placed in the simulation model for evaluation of color imaging quality. Then, a mocochrome grid was used to check image distortion of the camera. An LED light meter (Extech LT40) was employed to measure the environment illumination level in the abdominal cavity while a Wi-Fi camera was placed inside to capture motion of the camera.

Figure 3.7: Wireless imaging performance test. A picture of the anchored robotic surgical camera taken by a wifi camera is shown in a top-right insets.

Results suggested that both color and monochrome objects could be agreeably imaged for human eyes under sufficient illumination over 500lx. Color images became monochrome

when the illumination fell below 200lx. No noticeable image distortion was observed by human eyes and wireless video connection was stable throughout the test of 30min in the lab. Meanwhile, we deliberately took out the AV receiver and separated it from the camera up to a distance of 10m, which gives some idea of the maximum signal coverage.

BLE Control Tests

Tetherless camera control based on BLE communication was evaluated in terms of sCAM profile services and the received signal strength. As is detailed in Section 2.4.1, camera functions are all implemented in the form of BLE profile services including lighting, imaging, IMU, battery, and temperature. Each service has its own characteristic data bytes that could be read or written by the BLE central device on the stator. Results had confirmed effective control of camera functions using these BLE services. Illumination LED PWM was set arbitrarily between 0 (off) and 255 (fully lit) by writing the lighting service byte. Imaging quality could be tuned online by writing the imaging service bytes, which actually updates the CMOS imaging sensor registers. By reading the IMU service bytes, motion information of the rotor was acquired in real time at 30 frames per second, which could be able to feedback close-loop camera motion control. Likewise, battery voltage and temperature of the camera were monitored by reading corresponding service bytes respectively.

Recieved signal strength indicator (RSSI) values on the BLE central device were recorded and graphed as Fig. 3.8. First, both the stator actuator and the rotor camera were placed in the open air. Then, the rotor camera was inserted into the abdominal cavity while the stator actuator was left in the outside. RSSI values at different stator-rotor distances in both scenarios were compared to show radiation property of BLE signals and effects of the simulation model. It could be concluded that RSSI was attenuated to a certain degree by the synthetic abdominal material. Noticeable differences were seen primarily in the middle range from 10cm to 140cm while RSSI values were similar between these two scenarios in ranges within 10cm or beyond 140cm. Since the rotor camera is actually close to the stator actuator in clinical practice so as to maintain effective magnetic coupling, an RSSI value of -52dBm or better could be achieved within 50mm.

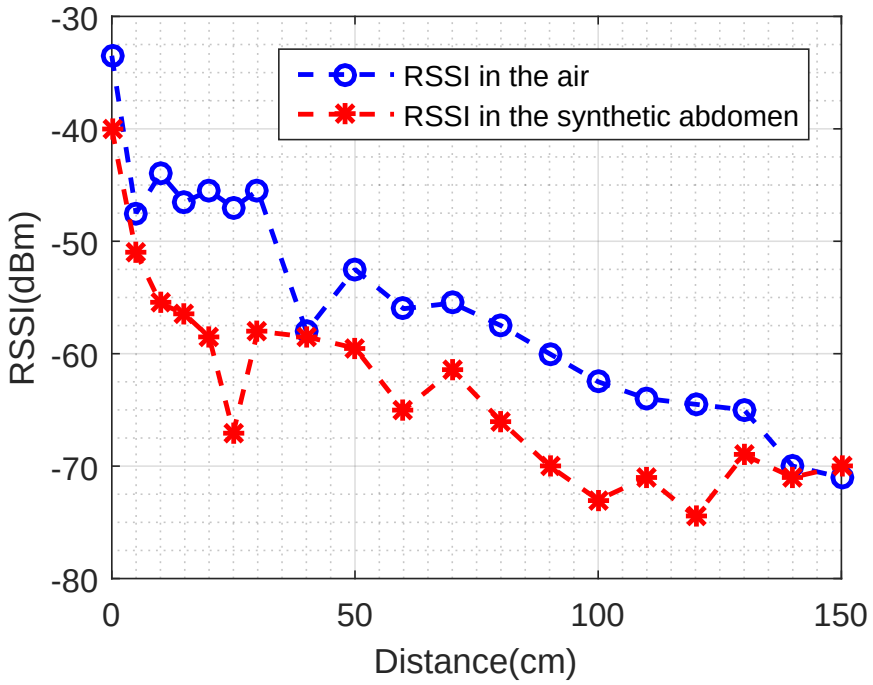

Figure 3.8: RSSIs with respect to stator-rotor distances.

3.4 Wireless Power

Several measures could be taken to eliminate the wires for powering. Currently, wireless power is achieved using onboard batteries as is detailed in Section 2.3.2. In the future, wireless charging or powering could be an option to extend battery duration or eventually eliminate onboard batteries and the power limit.

3.4.1 Experimental Validation

The power duration determines how long the camera could continuously function *in vivo* and thus the scope of procedures that could be performed using this camera. Power consumption of each module onboard the rotor camera has been tested and tabulated in Table. 3.1. Average power duration could reach more than 50min according to the onboard battery capacity introduced in Section 2.3.2 without any power optimization. This power duration time covers most diagnostic laparoscopic procedures and some simple operative laparoscopic procedures [54].

Table 3.1: Power consumption ratings

Module	**Tested Current**(mA)	**Max Current**(mA)
Wireless MCU	17.5 (Active TX)	18.2 (Active TX)
Inertial Sensors	2.9	3.9
Imageing	55	60
AV Transmitter	50	54
Illumination	0~120	130

3.5 Summary

In this chapter, the approaches to the untethered camera access have been revealed in details and experimentally validated in a synthetic abdomen model. Wireless video transmission and control communication using onboard power have completely eliminated cumbersome tethering wires. Meanwhile, transabdominal camera actuation based on magnetic coupling removes constraints from mechanical driving linkages and anchoring fixation. As a result, although there exists no physical connection to this *in vivo* camera, the sCAM is accessible from the outside for manipulation, laparoscopic vision, as well as function control. The sCAM has brought robotic laparoscopic imaging one step further toward less invasiveness and more dexterity.

Chapter 4

Force Measurement

4.1 Introduction

Fully insertable laparoscopic cameras feature more locomotive flexibility in a larger workspace compared to conventional trocar-based laparoscopes and represent a promising future of minimally invasive surgery. Although several proof-of-concept prototypes have shown their technical feasibility in terms of camera actuation and laparoscopic imaging, none of them are getting close to clinical application due to concerns about safety. One common problem lies in that the interaction force between the *in vivo* camera and the abdominal wall tissue is completely unknown, not to mention controlled. The camera is being manipulated in an open loop in terms of force control and the patient has been exposed to a high risk of being injured due to inappropriate camera-tissue contact force [5]. Moreover, it's worth noting that it's the stress magnitude and duration that finally determine whether an irreversible damage could be caused to the tissue [55]. Therefore, not only the camera-tissue interaction force is of our interest, but also the stress distribution needs to be accurately described.

This chapter characterizes the camera-tissue interaction process using a constitutive tissue model of the abdominal wall consisting of a series of Kelvin-Voigt viscoelastic models. The camera-tissue interaction modeling relates forces between the camera and the tissue to the contact profile geometry and finally to the stress distribution over the tissue. Furthermore, this chapter also elaborates on a non-invasive approach to measuring the camera-tissue interaction force. With the force measurement results, the camera-tissue

interaction model simulates the contact profile geometry as well as the stress distribution. The camera-tissue contact force could be reproduced at the user interface to recover the lost force feedback for the surgeon's hand during camera manipulation, while the stress distribution provides an effective feedback for tissue damage prevention.

4.2 Camera-Tissue Interaction Modeling

Rentschler *et al.* studied the interaction between a wheeled robotic device and organ tissue surfaces [17], where the robot crawls on the organs facilitated by differential wheel actuation. Their work resulted in some force-deformation relations with too many unknowns to reach a solvable equation system. This work has been using a similar analysis process enhanced by a geometric constraint and realized a solvable system.

4.2.1 Tissue Model

To effectively study the interaction between the rigid camera and the soft abdominal wall tissue, an appropriate model needs to be firstly found to represent the mechanical behavior of bulk soft tissues. According to [56], *in vivo* biomechanical properties of the abdominal wall tissue have not yet been sufficiently explored, due to complex influencing factors including the microscopic tissue morphology, chemical composition of the tissue, fluid flow, directionality of fiber structures, as well as connective materials between different layers.

Usually, the bulk soft tissue takes on a combination of non-linearity, non-homogeneity, anisotropy, and viscoelasticity. However, a tissue model that could accurately describe its non-linear viscoelastic property under creep compression in one direction would be sufficient for our modeling, taking into account the following facts. First, the camera is anchored into the tissue in a quasi-static state throughout the process. Thus, the tissue is primarily under creep compression and no relaxation or hysteresis needs to be considered. Second, the camera is anchored perpendicular to the abdominal wall, which means the tissue model only needs to depict its behavior in one direction while the non-homogeneity and the anisotropy could be both ignored.

Therefore, the Kelvin-Voigt model[1], which although is not good at describing the relaxation behavior after the stress load is removed however is effective for predicting creep compression, has been chosen for the tissue model.

A KelvinVoigt material, also called a Voigt material, is a viscoelastic material showing the properties both of elasticity and viscosity. It is named jointly after the British physicist and engineer Lord Kelvin and after German physicist Woldemar Voigt. As is shown in Fig. 4.1, the KelvinVoigt model, also called the Voigt model, can be represented by a purely viscous damper and a purely elastic spring connected in parallel. The behavior of a Kelvin-Voigt model is governed by its dynamic differential equation 4.1, where E and η are respectively the modulus of elasticity for the spring and the viscosity for the damper while σ and ϵ respectively represent the stress and the strain. Given a constant stress of σ_0 with a zero initial condition, the deformation decays exponentially and approaches the deformation of a pure elastic model σ_0/E over time, as is mathematically expressed in 4.2, where $\lambda = E/\eta$ is called the rate of relaxation and $\tau = \eta/E$ is defined as the retardation time.

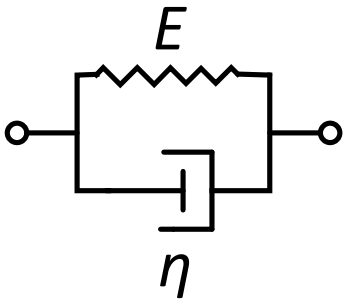

Figure 4.1: Schematic representation of the Kelvin-Voigt model.

$$\sigma(t) = E\epsilon(t) + \eta\frac{d\epsilon(t)}{dt} \tag{4.1}$$

$$\epsilon(t) = \frac{\sigma_0}{E}(1 - e^{-\lambda t}) = \frac{\sigma_0}{E}(1 - e^{-\frac{t}{\tau}}) \tag{4.2}$$

As is shown in Fig. 4.2, the mechanical behavior of the abdominal wall tissue is simulated using a constitutive viscoelastic model consisting of four Kelvin-Voigt models connected in series, each representing one layer of the constitutive materials. According to 4.1 and 4.2, the

[1]According to Wikipedia: https://en.wikipedia.org/wiki/Kelvin%E2%80%93Voigt_material

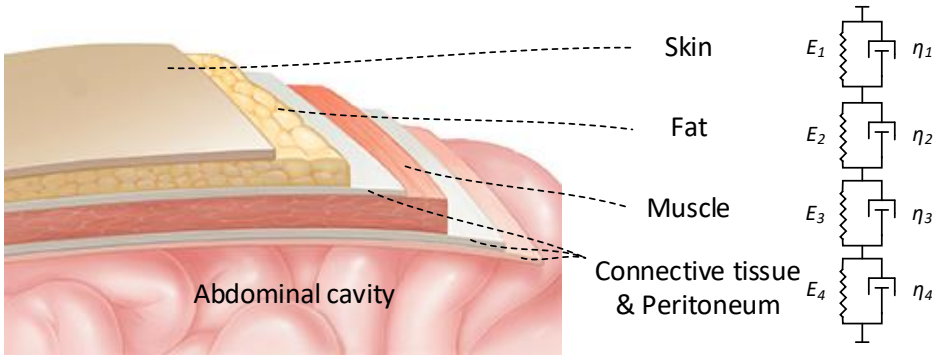

Figure 4.2: The abdominal wall tissue model.

dynamic differential equation of each layer is given as 4.3 and 4.4. Considering $\sigma(t) = \sigma_i(t)$ and $\epsilon(t) = \sum_{i=1}^{4} \epsilon_i(t)$, the creep behavior of the abdominal wall tissue could be described by its dynamic differential equation 4.5 and deformation equation 4.6. Over time in a quasi-static compression state, the tissue deformation decays exponentially to $\sigma_0 \sum_{i=1}^{4} \frac{1}{E_i}$.

$$\sigma_i(t) = E_i \epsilon_i(t) + \eta_i \frac{d\epsilon_i(t)}{dt} \tag{4.3}$$

$$\epsilon_i(t) = \frac{\sigma_0}{E_i}(1 - e^{-\frac{t}{\tau_i}}) \tag{4.4}$$

$$\sigma(t) = \frac{\epsilon(t) + \sum_{i=1}^{4} \tau_i \frac{d\epsilon_i(t)}{dt}}{\sum_{i=1}^{4} \frac{1}{E_i}} \tag{4.5}$$

$$\epsilon(t) = \sigma_0 \sum_{i=1}^{4} \frac{1}{E_i}(1 - e^{-\frac{t}{\tau_i}}) \tag{4.6}$$

4.2.2 Contact Profile

The contact profile between the camera and the tissue is depicted using two sectional views. Fig. 4.3 gives a latitudinal sectional view of the camera-tissue contact geometry. The tissue surface is in close contact with the camera and takes on the shape of an arc between A and B. Beyond these two points, the tissue surface leaves contact with the camera and the

deformation $w(y)$ decays along Y. The camera radius is r and z_c is the vertical position of the center of the camera. φ_a and φ_b represent the contact angles while C_a and C_b are the corresponding contact lengths. The tissue indentation is denoted as h. The longitudinal sectional view is shown in Fig. 4.4, where the tissue surface leaves contact with the camera at C and D. Similar to the parameters in Fig. 4.3, $w(x)$ represents the tissue deformation and decays along X. φ_c and φ_d are the contact angles while C_c and C_d denote the corresponding contact lengths.

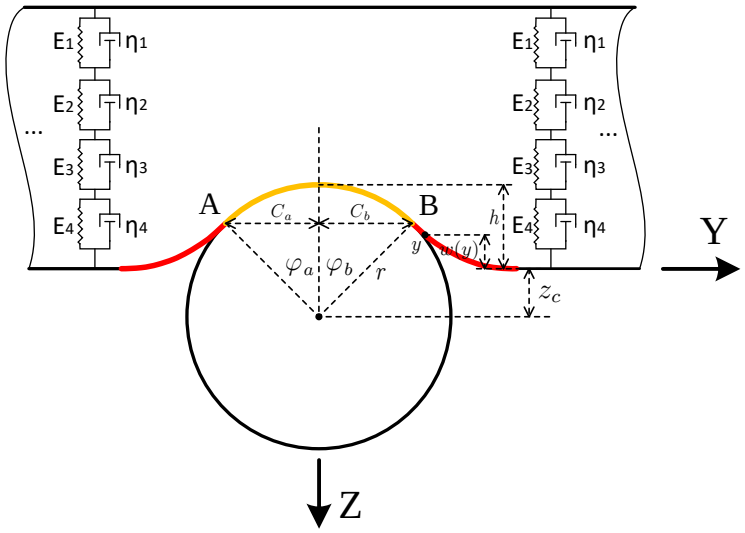

Figure 4.3: Latitudinal sectional view of the contact profile.

Except for r, the other parameters are naturally unknown. Obviously, for a certain tissue modeled as Section 4.2.1, the surface profile could be a determined function of the tissue indentation h under creep compression. In order to establish the mathematical equations describing the profile geometry as a function of h, an ideal case where the camera is normally anchored into the tissue is investigated as a beginning based on the following two assumptions. *First*, the tissue deformation decays exponentially [17] along X/Y as 4.7. The contact angles are considered identical ($\varphi_a = \varphi_b = \varphi_c = \varphi_d = \varphi$) since the camera is considered normal into the tissue. *Second*, the contact angle is related to the tissue indentation by 4.8, where k is a constant coefficient related to the tissue property and the camera diameter.

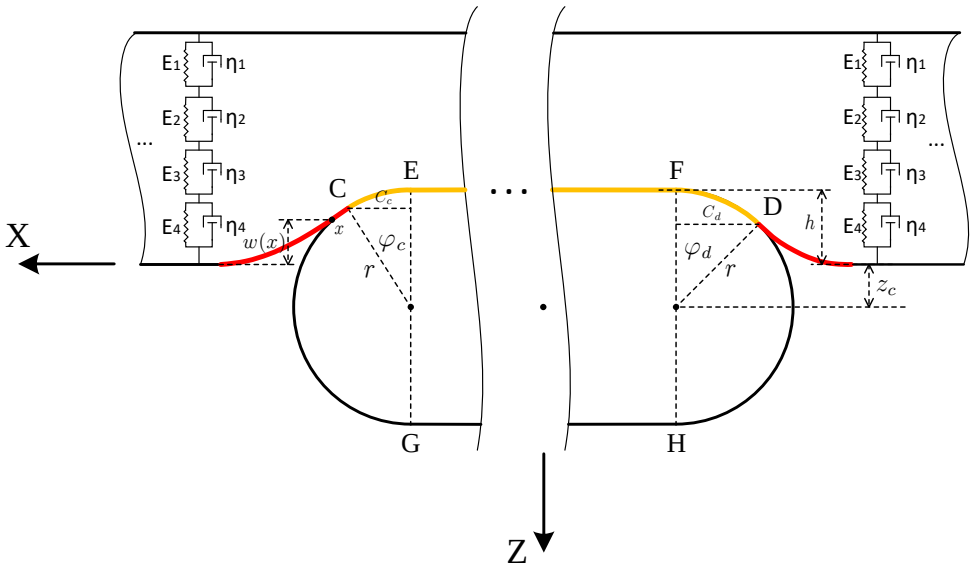

Figure 4.4: Longitudinal sectional view of the contact profile.

$$w(x/y) = \begin{cases} rcos(\varphi(x/y)) - z_c & , \ y \in \widehat{AB} \text{ or } x \in (\widehat{CE} \cap \widehat{DF}) \\ h & , \ x \in \overline{EF} \\ Ae^{B(x/y-C)} & , \ other \end{cases} \tag{4.7}$$

$$tan(\varphi) = kh \tag{4.8}$$

The deformation equation is conditioned on two boundary conditions 4.9 and 4.10 at each contact point of A, B, C, and D.

$$w(x/y = C) = rcos(\varphi) - z_c \tag{4.9}$$

$$\frac{dw(x/y = C)}{dy} = -tan(\varphi) \tag{4.10}$$

Solving 4.7, 4.9, and 4.10, A and B are found as

$$A = rcos(\varphi) - z_c \tag{4.11}$$

$$B = -\frac{tan(\varphi)}{rcos(\varphi) - z_c} \tag{4.12}$$

Meanwhile, z_c is also expressed as a function of h according to the geometric relation shown in Fig. 4.3.

$$z_c = r - h \tag{4.13}$$

Therefore, substituting equations 4.8 to 4.13 into 4.7, the camera-tissue contact profile geometry has been established as a determined function of tissue indentation, laying foundation for stress calculation and force integration.

4.2.3 Stress Distribution and Simulation

The stress distribution is illustrated as Fig. 4.5 and Fig. 4.6. The vertical stress $q(x/y)$ along Z represents the stress caused by tissue strain in the modeled direction in Section 4.2.1, while $p(x/y)$ represents the stress along X/Y. At each point of the tissue surface, the joint stress is considered normal to the surface as is indicated.

Based on the tissue model in Section 4.2.1 and the geometric relations established in Section 4.2.2, the stresses over the tissue surface could now be accurately calculated. According to 4.5, the vertical stress component could be given as 4.14. Since the camera is anchored still in a quasi-static state, $dw_i(x/y,t)/dt$ could be ignored as time goes and $q(x/y)$ is simplified as 4.15, where $E = 1/(\sum_{i=1}^{4} 1/E_i)$ is the equivalent modulus of elasticity of the tissue. The approach to determining the tissue property parameters has been proposed and detailed in our work [57], which is a research topic for another graduate student.

$$q(x/y,t) = \frac{w(y,t) + \sum_{i=1}^{4} \tau_i \frac{dw_i(y,t)}{dt}}{\sum_{i=1}^{4} \frac{1}{E_i}} \tag{4.14}$$

$$q(x/y) = \frac{w(x/y)}{\sum_{i=1}^{4} \frac{1}{E_i}} = Ew(x/y) \tag{4.15}$$

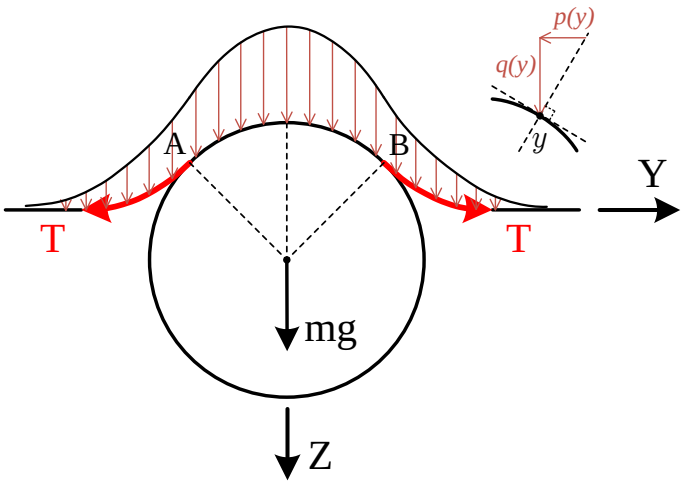

Figure 4.5: Latitudinal sectional view of stress distribution.

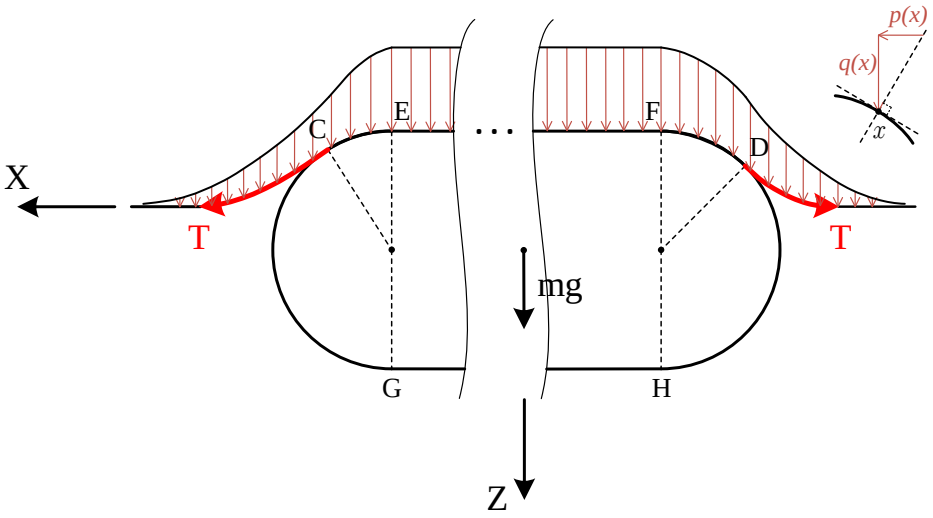

Figure 4.6: Longitudinal sectional view of stress distribution.

The stress distribution has been simulated in Matlab to quantitatively visualize the results and validate the modeling work. Prior to the simulation process, several parameters need to be chosen appropriately. The effective stiffness of the tissue E and the constant coefficient k were fitted using linear least-square parameter fitting performed *ex vivo* [17][57].

$$rsin(\varphi) \leq \sqrt{r^2 - z_c^2} \tag{4.16}$$

Meanwhile, it's worth noting that there exists an geometric constraint 4.16 for the choice of k. According to the contact profile in Fig. 4.3, the contact length C won't exceed $\sqrt{r^2 - z_c^2}$ at any indentation between zero and r as the tissue is compliant and flexible. Substituting 4.8 and 4.13 into 4.16, 4.17 is achieved.

$$\begin{aligned} & k^2 \leq \frac{2r-h}{h(r-h)^2} \\ \Rightarrow & k^2 \leq min\{\frac{2r-h}{h(r-h)^2}\}, \quad h \in (0, r) \\ \Rightarrow & k^2 \leq \frac{(\frac{1+\sqrt{5}}{3-\sqrt{5}})(\frac{2}{-1+\sqrt{5}})^2}{r^2}, \quad \text{when } h = \frac{(3-\sqrt{5})}{2}r \\ \Rightarrow & k \leq \frac{2.32}{r}, \quad \text{when } h = 0.38r \end{aligned} \tag{4.17}$$

According to Table. 2.2, $r = 0.008m$ and $k \leq 290.16m^{-1}$. Finally, E was approximated as $E = 200000N/m^3$, k was chosen as $k = 125m^{-1}$. The simulations were performed in an tissue area of $20mm \times 100mm$ at an tissue indentation of $h = 0.25r = 0.002m$ with all other attributes the same as given in Table. 2.2. The vertical stress $q(x, y)$ distribution is shown in Fig. 4.7, with the maximum stress values of $400Pa$ at the deepest part of the tissue. Fig. 4.8 shows the horizontal stresses $p(x, y)$. Different from the vertical stress distribution, the lowest values of $0Pa$ were found at the deepest part of the tissue, while the maximum values $88.057Pa$ occurred where the tissue leaves contact with the camera.

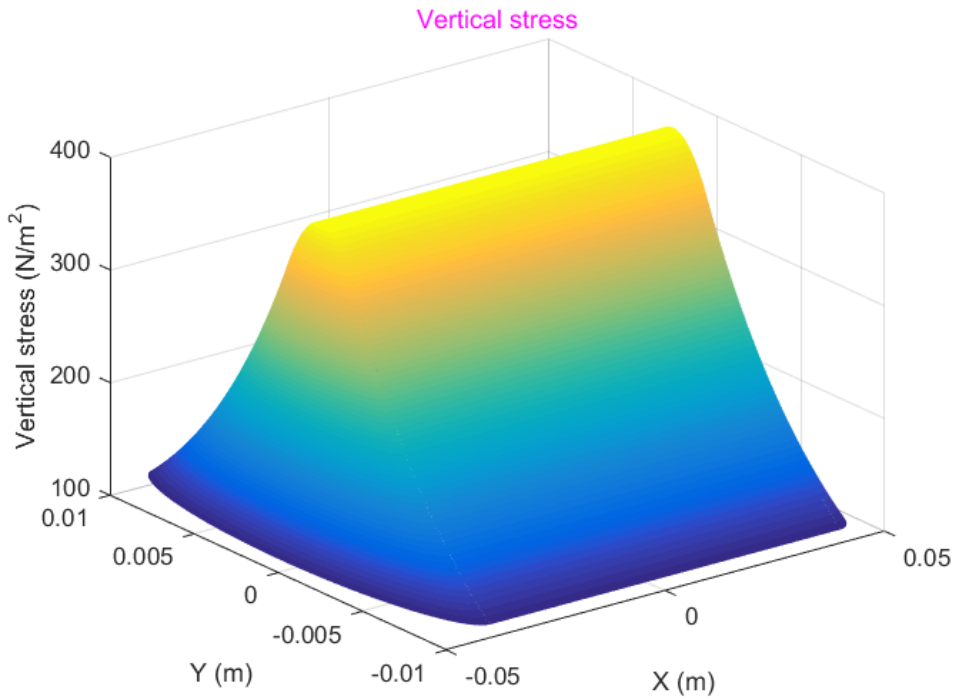

Figure 4.7: Vertical stress distribution.

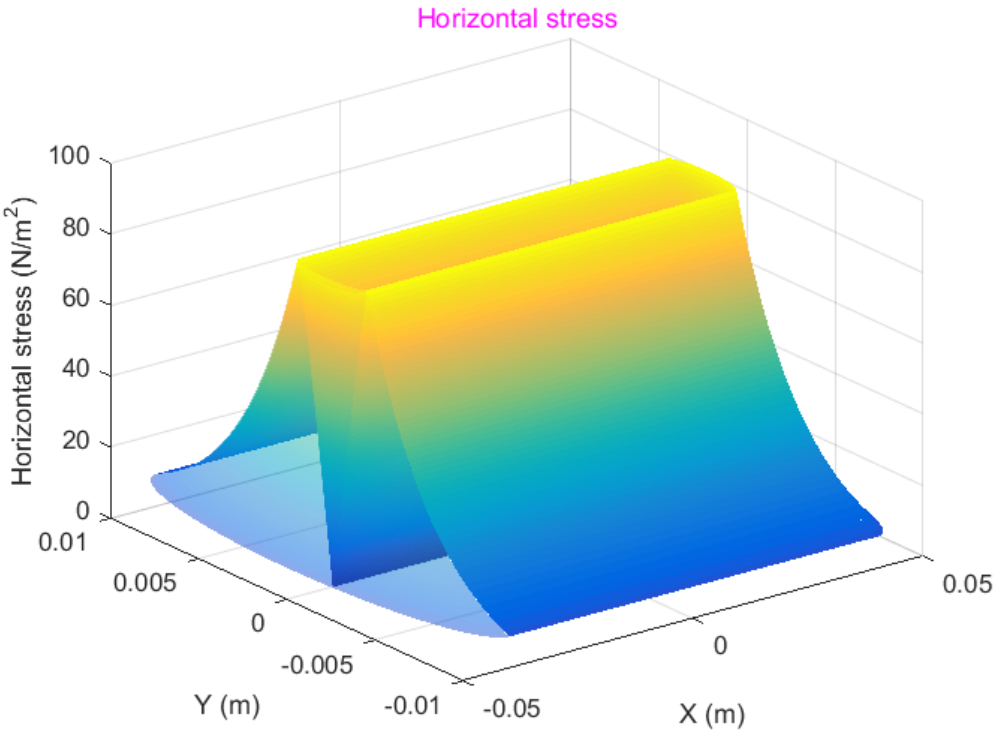

Figure 4.8: Horizontal stress distribution.

Fig. 4.9 plotted the vertical and the horizontal stresses for comparison, which clearly shows the difference and indicates the vertical stresses are the dominant stresses during the camera-tissue interaction. The resultant normal stresses over the tissue surface is plotted in Fig. 4.10 which takes on a similar shape to Fig. 4.7 with the same maximum stress values of $400Pa$. Obviously, the stress distribution over the tissue surface is symmetric about the XZ and YZ planes. Thus, integrating these stresses over the tissue surface will result in a vertical resultant force, which is detailed in Section 4.2.4.

4.2.4 Force Integration and Simulation

Integrating the stresses over the tissue surface, the interaction forces between the camera and the tissue will be achieved. The forces applied to the camera by the tissue could be classified into two types, pressure forces and membrane forces, according to the interaction situation. The pressure forces are caused by the stress over the contact area between the camera and the tissue, while the membrane forces represent forces applied to the camera by membrane tension caused by stresses beyond the contact area. In order to clarify the integration process, the camera has been imaged as a combination of a cylinder of $L \times \phi 2r$ (the central segment between EG and FH) and a sphere of $\phi 2r$ (made of the two semi-spheres at the ends of the camera). Therefore, the camera tissue interaction force is given as 4.18 each item of which will be detailed in this section.

$$\begin{aligned} F_{interaction} &= F_{pressure} + F_{membrane} \\ &= F_{cylinder-pressure} + F_{cylinder-membrane} \\ &\quad + F_{sphere-pressure} + F_{sphere-membrane} \end{aligned} \tag{4.18}$$

As is shown in Fig. 4.5 and Fig. 4.6, due to symmetry of the stress distribution, the resultant force in the horizontal XY plane is zero in theory. For the cylinder component, Fig. 4.5 represents the latitudinal sectional view of stress distribution and $F_{cylinder-pressure}$ is integrated 4.19 over the 2D projection area D_1 of the camera-tissue contact area on XY plane.

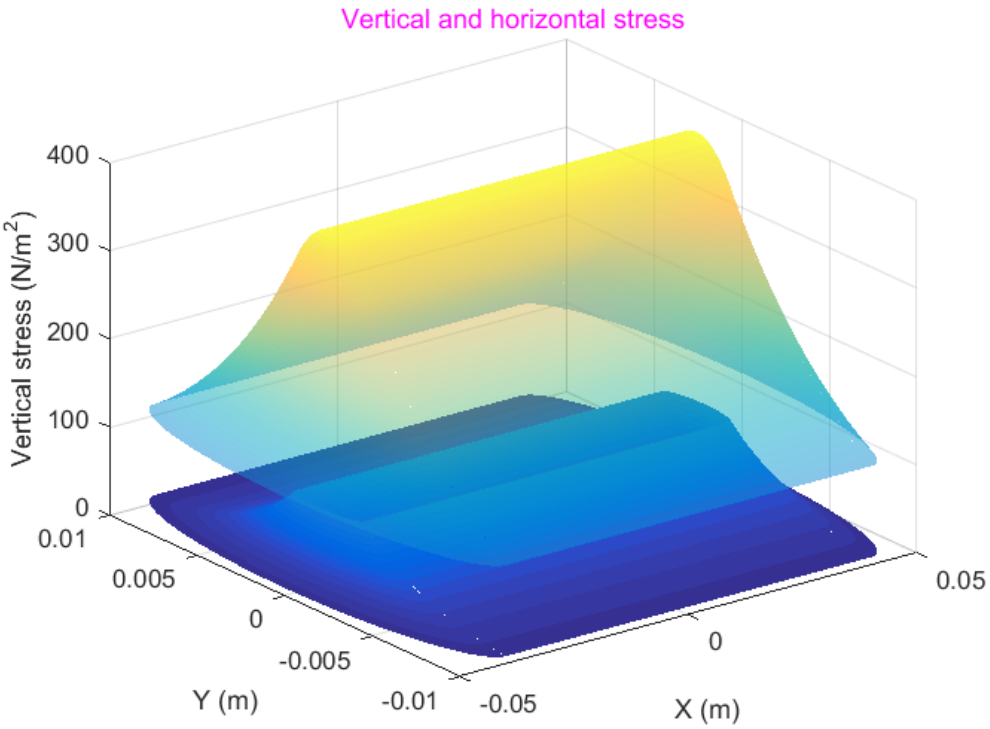

Figure 4.9: Vertical-horizontal stress comparison.

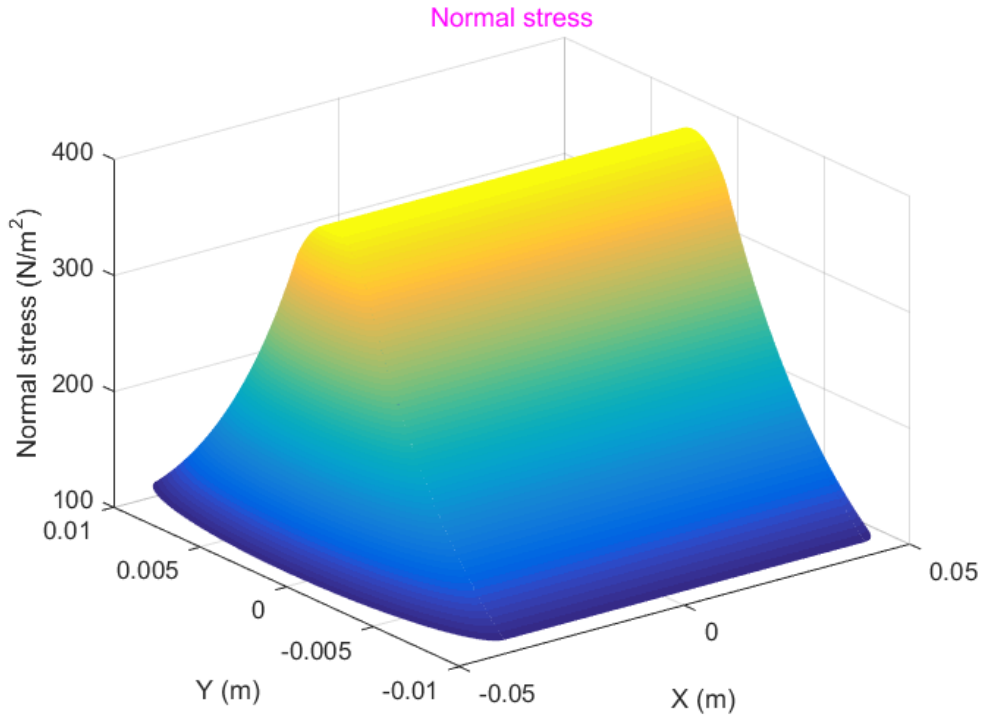

Figure 4.10: Normal stress distribution.

$$
\begin{aligned}
F_{cylinder-pressure} &= \iint_{D_1} E(\sqrt{r^2-y^2}-z_c)dxdy \\
&= E\iint_{D_{xy}} (\sqrt{r^2-y^2}-z_c)dxdy \\
&= E\int_{-\frac{L}{2}}^{\frac{L}{2}} dx \int_{-C}^{C} (\sqrt{r^2-y^2}-z_c)dy \\
&= EL(C\sqrt{r^2-C^2}+r^2 arcsin(\frac{C}{r})-2z_cC)
\end{aligned}
\tag{4.19}
$$

The membrane force $F_{cylinder-membrane}$ corresponding to the cylinder component is integrated 4.20 over the 2D projection area D_2 on XY plane of the tissue surface that is not in contact with the camera, where T represents the membrane tension.

$$
\begin{aligned}
F_{cylinder-membrane} &= 2Tsin(\varphi) \\
&= 2EA\iint_{D_2} (e^{B(y-C)})dxdy \\
&= 2EA\int_{-\frac{L}{2}}^{\frac{L}{2}} dx \int_{C}^{\infty} (e^{B(y-C)})dy \\
&= -\frac{EAL}{B}
\end{aligned}
\tag{4.20}
$$

The two semi-sphere components at the ends of the camera have been imagined as an intact sphere anchored into the abdominal wall tissue to make the force integration easier without affecting the results. For the imagined sphere, Fig. 4.5 is still useful as an longitudinal sectional view of the stress distribution. Similar to $F_{cylinder-pressure}$, the pressure force corresponding to this sphere $F_{sphere-pressure}$ is integrated 4.21 over the 2D projection area D_3 of the camera-tissue contact area on XY plane.

$$
\begin{aligned}
F_{sphere-pressure} &= \iint_{D_3} E(\sqrt{r^2 - x^2 - y^2} - z_c)dxdy \\
&= E\iint_{D_{xy}} (\sqrt{r^2 - \rho^2} - z_c)\rho d\rho d\theta \\
&= E\int_0^{2\pi} d\theta \int_0^{C} \sqrt{r^2 - \rho^2}\rho d\rho \\
&= 2\pi E(-\frac{1}{3}(r^2 - C^2)^{\frac{3}{2}} - \frac{1}{2}z_c C^2 + \frac{1}{3}r^3)
\end{aligned}
\tag{4.21}
$$

Likewise, the membrane force $F_{sphere-membrane}$ corresponding to the sphere component is integrated 4.22 over the 2D projection area D_4 on XY plane of the tissue surface that surrounds the contact area but is not in contact with the sphere.

$$
\begin{aligned}
F_{sphere-membrane} &= \iint_{D_4} E(Ae^{B\sqrt{x^2+y^2}-C})dxdy \\
&= EA\iint_{D_{xy}} e^{B(\rho-C)}\rho d\rho d\theta \\
&= EA\int_0^{2\pi} d\theta \int_C^{\infty} e^{B(\rho-C)}\rho d\rho \\
&= -2\pi EA\frac{1}{B^2}(BC - 1)
\end{aligned}
\tag{4.22}
$$

Based on the above integration equations and the stress distributions revealed in Section 4.2.3, the force integrations were simulated in Matlab to characterize the interaction forces. The attribute parameters are the same as those in the stress distribution simulation. The simulations were performed within $h \in [0mm,\ 0.008mm]$ and the corresponding contact angle is within $\varphi \in [0rad,\ 0.78rad]$ as is shown in Fig. 4.11 governed by 4.8.

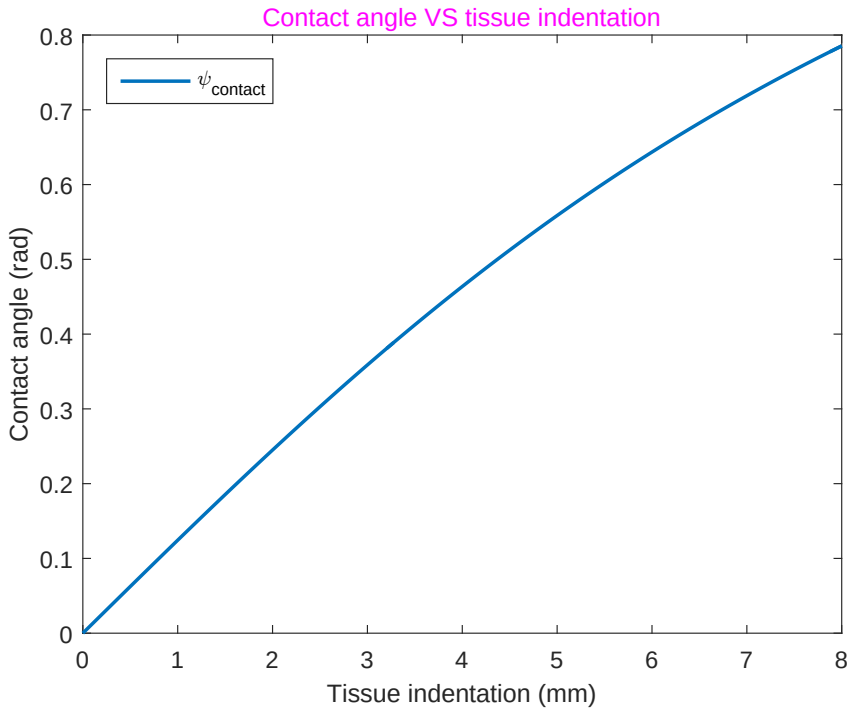

Figure 4.11: Relation between contact angle and tissue indentation.

Fig. 4.12 and Fig. 4.13 respectively plot the interaction force against the tissue indentation and the contact angle. According to the simulation results, the abdominal wall tissue is relatively compliant at small indentations and becomes stiffer at high indentations. The maximum interaction force of $2.9N$, as expected, occurred at the indentation of $h = 0.008mm$.

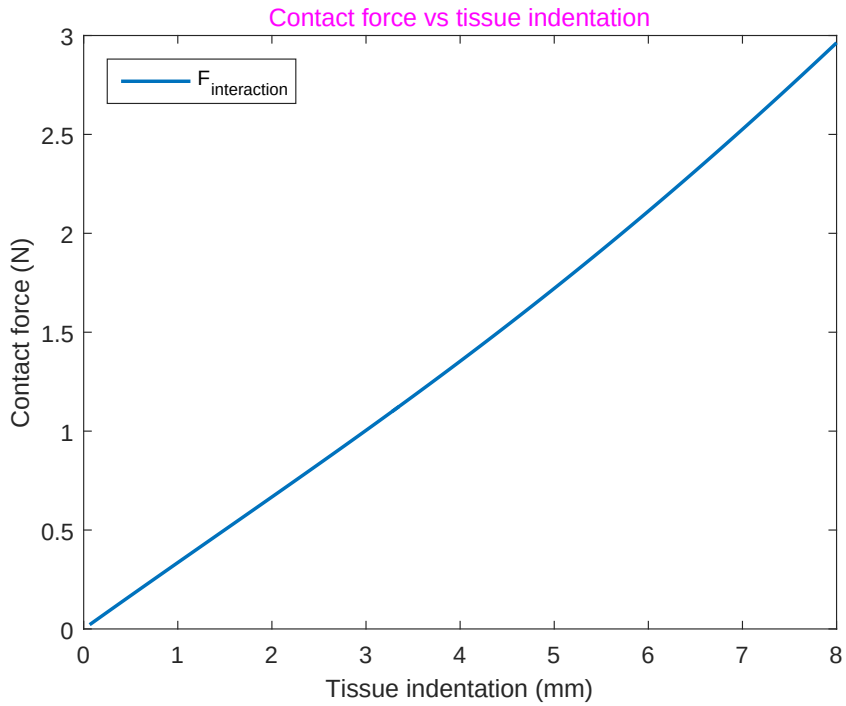

Figure 4.12: Interaction force vs tissue indentation.

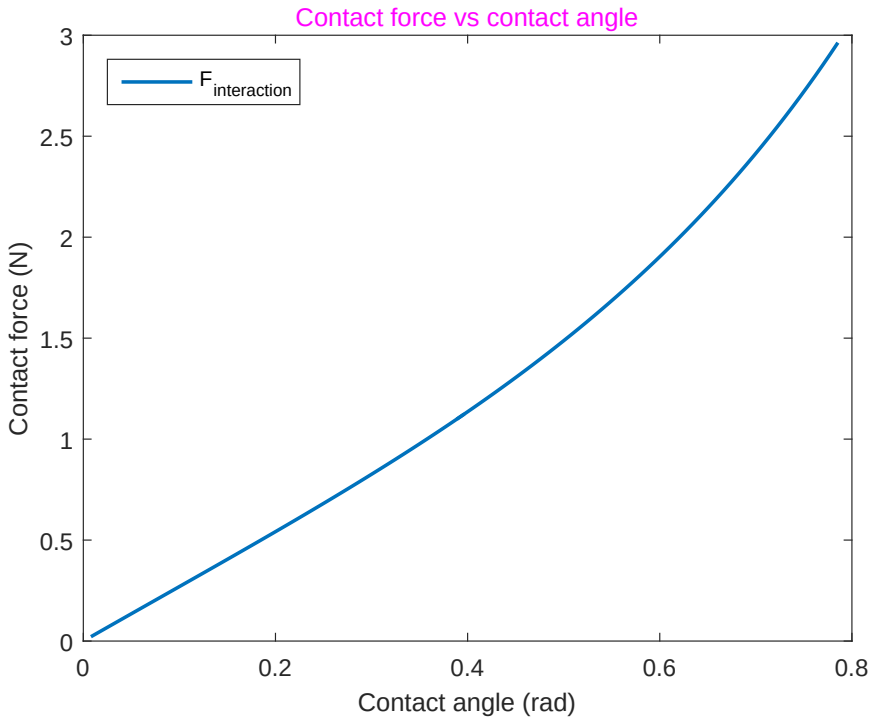

Figure 4.13: Interaction force vs contact angle.

In order to compare the contributions of different components, the pressure forces and the membrane forces of the cylinder component and the sphere component have been plotted against the tissue indentation h and the contact angle φ in Fig. 4.14 and Fig. 4.15. The cylinder forces contribute more than the sphere forces for most of the time, which is because the cylinder segment of the camera is larger than the imagined sphere segment. For the cylinder forces, $F_{cylinder-membrane}$ was dominant for most of the time. But $F_{cylinder-pressure}$ became dominant once the tissue indentation reached beyond $5.89mm$ or the contact angle exceeded $0.63rad$. For the sphere forces, the membrane force $F_{sphere-membrane}$ was always relatively dominant compared to the pressure force $F_{sphere-pressure}$.

4.3 Non-Invasive Force Measurement

A non-invasive measuring approach to the camera-tissue contact force has been chosen over estimation based on pure mathematical camera-tissue interaction modeling or measurement using invasive force sensors for the following reasons.

First, in vivo biomechanical properties of the abdominal wall tissue have not yet been explored effectively [55]. Thus, modeling and simulation of the camera-tissue interaction not only can not provide real force measurements but also are impossible without assumptions that are far away from the reality. *Second,* mathematical camera-tissue interaction modeling is expected to be useful to estimate the camera-tissue contact force from the geometric interaction information or vice versa. Unfortunately, neither of them is naturally available since the camera is completely *in vivo* and invisibly secured on the interior abdominal wall. *Third,* it's technically unrealistic to incorporate enormous miniaturized force sensors on the camera-tissue contact interface and measure forces on every contact point. A non-invasive measuring approach that accesses the resultant camera-tissue contact force with sensors located outside the patient's anatomy could be subject to smaller sterilization and miniaturization challenges.

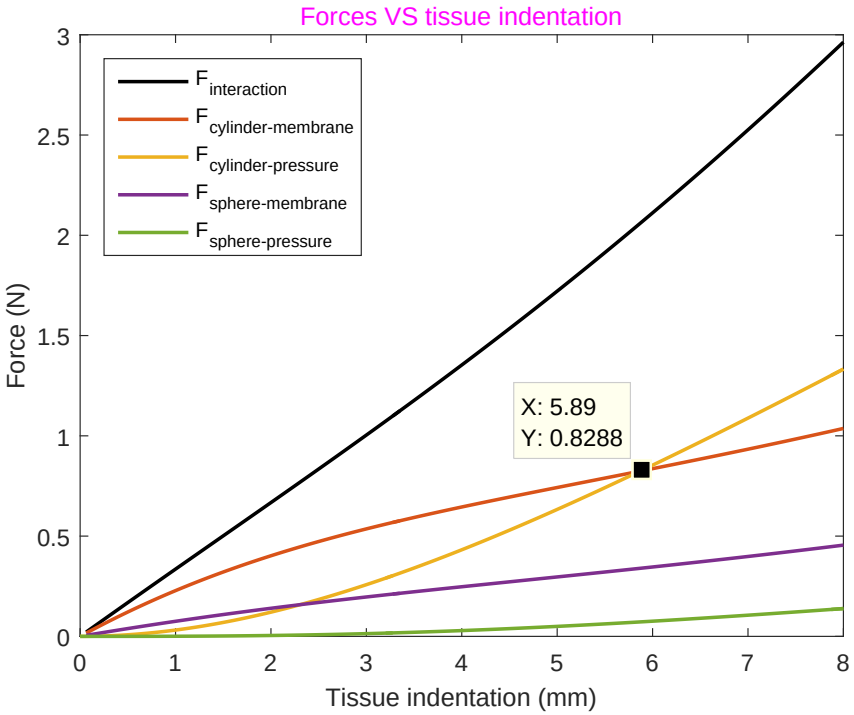

Figure 4.14: Forces vs tissue indentation.

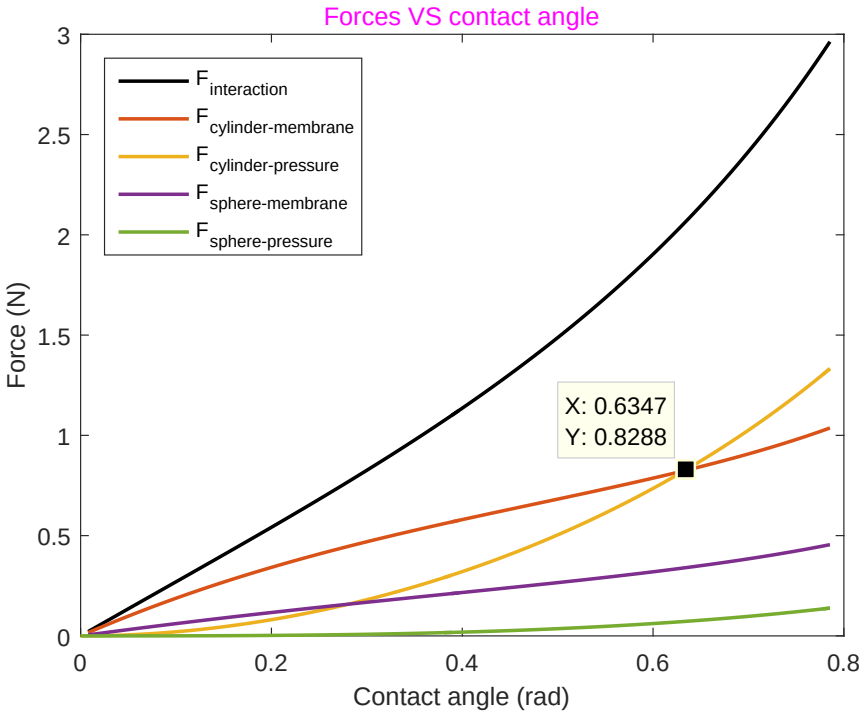

Figure 4.15: Forces vs contact angle.

4.3.1 Approach

Hence, in order to access the camera-tissue contact force for closed-loop control feedback, three OptoForce 3D force sensors, instead of being integrated onboard the invasive camera, have been installed on the actuator between the upper part (hanger) and the lower part (stator). As is indicated in Fig. 4.16, the three force sensors are evenly installed on the flange of the hanger and the stator has been hung on the hanger through these force sensors. These sensors measure the exact forces exerted on the stator by the hanger and cause zero invasion into the patient during the procedure. In this non-invasive manner, the camera-tissue contact force could be accessed by solving the equilibrium of the stator-rotor system as modeled and analyzed in Section 4.3.2.

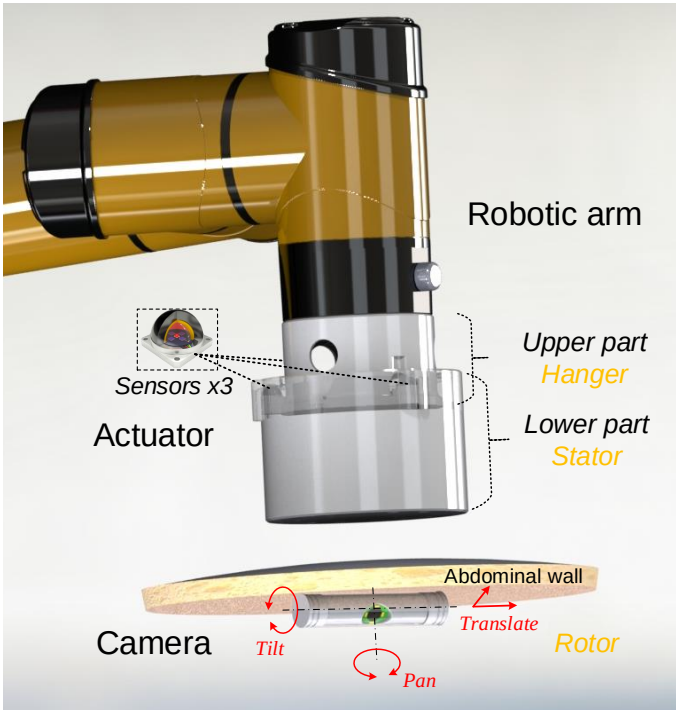

Figure 4.16: Overview of the sCAM.

4.3.2 Modeling and Force Analysis

Current modeling methods ideally assume that the movement of the camera is always a horizontal 2D space and the camera-tissue contact profiles are identical as shown in Fig. 4.3 across different intersections. Actually, both the camera and the actuator locomote in a

3D space although the camera is constrained to the interior of the curved abdominal wall. Moreover, the middle of the camera may actually not be in contact with the tissue with all forces exerted on the ends of the camera. A more general modeling which is limited to minimum kinematic or geometric assumptions has been elaborated in this paper for practical applications.

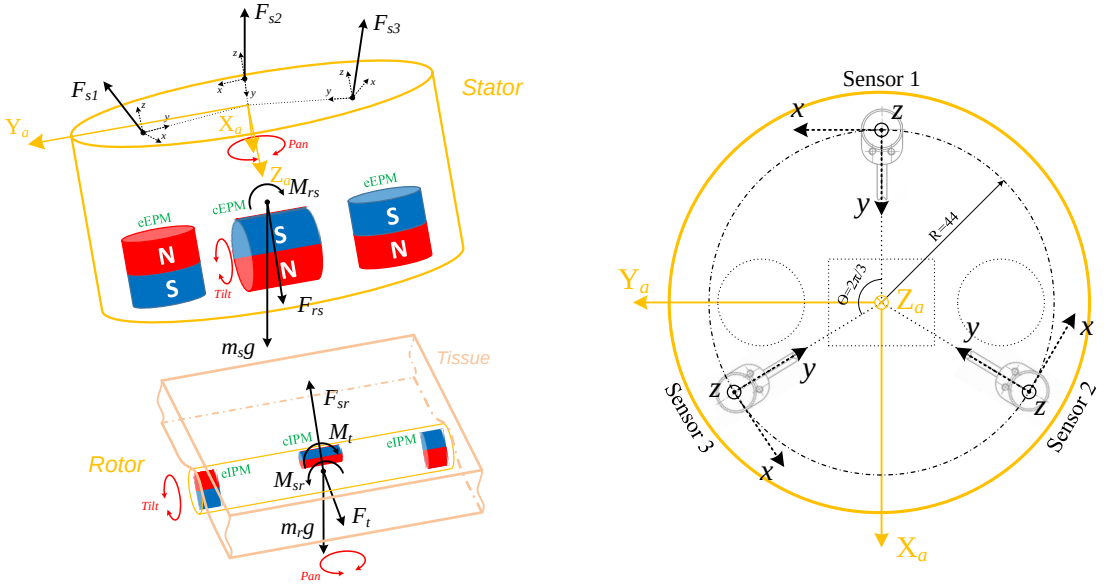

(a) Free body diagram **(b)** Top view of the free body diagram

Figure 4.17: Modeling and force analysis.

As is illustrated in Fig. 4.17a, a free body diagram of the system has been drawn on the schematic of the stator-rotor mechanism. An inertial coordinate frame $X_i Y_i Z_i$ fixed on the base of the robotic arm is referred to as the world coordinate frame. An actuator coordinate frame $X_a Y_a Z_a$ is attached at the center of the hanger-stator contact plane with the Z_a-axis perpendicular to the plane and pointing into the stator. The Y_a-axis is parallel to the axis of the cEPM and the X_a-axis is determined by the right-hand rule. A top view of the diagram in Fig. 4.17b depicts relative poses of force sensor coordinate frames with respect to the actuator frame. These sensors are evenly distributed on a circle of $R = 44mm$ on the hanger-stator contact plane at an interval of $\theta = 2\pi/3$. The sensor frames have been configured symmetrical about the Z_a-axis with their y-axes pointing at the center, z-axes pointing upwards and x-axes tangent to the circle. This centrosymmetric configuration

makes each sensor geometrically identical and equivalent, which simplifies the modeling and sensor installation.

The actual forces inside and between the stator and the rotor could constitute a complex force system. To simplify analysis and calculation, these forces have been reduced to equivalent force-couple systems at the centers of gravity of the stator and the rotor as shown in Fig. 4.17a. Since the camera is anchored still on the interior abdominal wall for most of the time and only moves slowly when necessary, static force equilibrium equations of rigid bodies have been employed and worked well according to experimental results.

For the stator, a force equilibrium could be formulated as 4.23, where $\boldsymbol{F_{rs}}$ represents the resultant magnetic attraction between the rotor and the stator, $\boldsymbol{F_{sensor}}$ is the joint force measured by force sensors, and $m_s\boldsymbol{g}$ is the gravity of the stator.

$$\sum \boldsymbol{F_{stator}} = \boldsymbol{F_{rs}} + \boldsymbol{F_{sensor}} + m_s\boldsymbol{g} = \boldsymbol{0} \tag{4.23}$$

$$\sum \boldsymbol{F_{rotor}} = \boldsymbol{F_{sr}} + \boldsymbol{F_c} + m_r\boldsymbol{g} = \boldsymbol{0} \tag{4.24}$$

Likewise, the force equilibrium of the rotor could be formulated as 4.24, where $\boldsymbol{F_{sr}}$ is the counterforce of $\boldsymbol{F_{rs}}$, $m_r\boldsymbol{g}$ is the gravity of the rotor, and $\boldsymbol{F_{interaction}}$ is the resultant camera-tissue contact force of our interest. Combining 4.23 and 4.24, the camera-tissue contact force could be obtained as 4.25.

$$\boldsymbol{F_{interaction}} = -\boldsymbol{F_{sensor}} - (m_s + m_r)\boldsymbol{g} \tag{4.25}$$

$$\boldsymbol{F_{sensor}} = \boldsymbol{F_{s_1}} + \boldsymbol{F_{s_2}} + \boldsymbol{F_{s_3}} \tag{4.26}$$

Simply, m_s and m_r could be known from prior knowledge and the joint force applied to the stator through force sensors is computed as 4.26, where $\boldsymbol{F_{s_1}}$, $\boldsymbol{F_{s_2}}$, and $\boldsymbol{F_{s_3}}$ represent forces applied to the stator by the hanger through the three force sensors. These forces are originally measured in sensor frames, then projected to the actuator frame using 4.27, where $T^a_{s_i}$ is the transformation matrix from the i^{th} sensor frame to the actuator frame. Calculation

of the force equilibrium is performed in the actuator frame and then transformed into the world coordinate frame for robotic control.

$$\boldsymbol{F_{s_i}} = T^a_{s_i} \begin{bmatrix} f_x^{s_i} & f_y^{s_i} & f_z^{s_i} \end{bmatrix}^T, i = 1, 2, 3 \tag{4.27}$$

$$\boldsymbol{g} = T^a_i \begin{bmatrix} 0 & 0 & -g \end{bmatrix}^T \tag{4.28}$$

The pose of the actuator frame with respect to the inertial frame could be conveniently computed from joint variables of the robotic arm using forward kinematics. The expression of $\boldsymbol{g}$ relative to the actuator frame is given in 4.28 where T^a_i is the transformation matrix from the inertial frame to the actuator frame.

4.3.3 Implementation and Experiments

Prototype Fabrication

The fabricated prototypes of the actuator and the camera using rapid prototyping technology are shown in Fig. 4.18. Three 3D force sensors (OptoForce, OMD-10-SE-10N) installed on the flange of the hanger support the stator once the actuator is assembled. Specific ratings of the 3D force sensor are summarized in Table 4.1. Contact points between these force sensors and the stator have been numbered clockwise as indicated. A motor-driven worm-gear mechanism is adopted for tilting the cEPM with respect to the eEPMs. The mounting panel of the hanger is compatible with the end-effector mounting flange of the robotic arm so that the actuator could be mounted to the robotic arm as an end-effector. The camera profile resembles a cylinder with an oval window opened sideways in the middle for camera view and illumination. IPMs and functional payloads have been appropriately integrated inside the camera in a space-efficient manner [48]. The mechanical parts of the actuator and the camera were 3D printed with biocompatible resin which has been proven safe for surgical use. The force sensor base is made of aluminium alloy and fastened on the hanger using nonmagnetic screws so that no magnetic attraction exists between the stator and the hanger

and the camera-tissue contact force measurement is not contaminated. Table 4.2 lists some of the important physical attributes that characterize the fabricated actuator and camera.

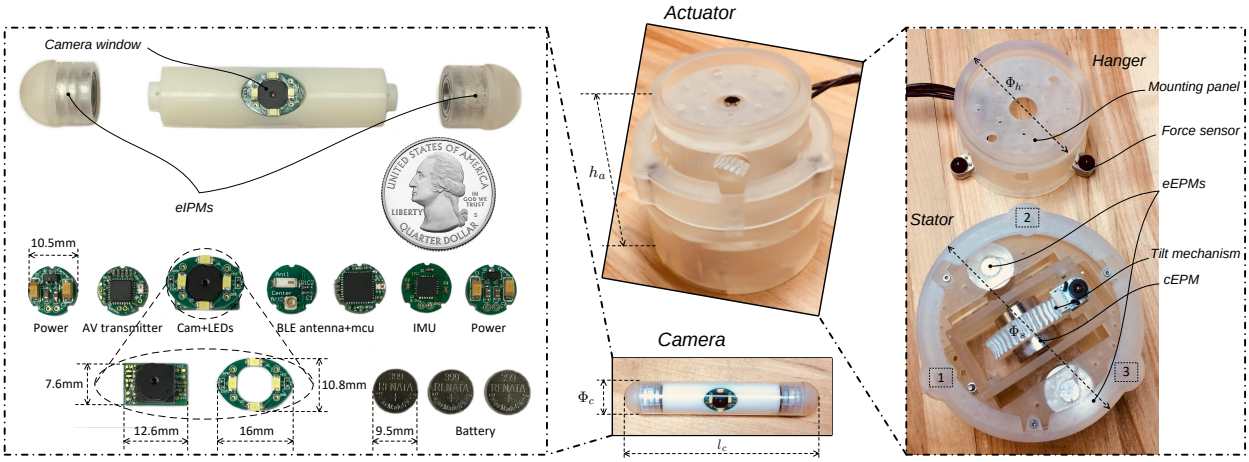

Figure 4.18: Fabricated prototypes of the actuator and the camera. Mechanical parts were printed using a Formlabs Form 2® 3D printer. Functional payloads for the camera including the imaging sensor and lens, illumination LEDs, Bluetooth low energy (BLE) module, video transmitter, inertial measurement unit (IMU), and onboard batteries have been stacked up inside the hollow cylinder.

Table 4.1: Ratings of the OptoForce 3D sensor

	Capacity	**Deformation**	**Resolution**	**nonlinearity**
F_{xy}	$\pm 2.5N$	$\pm 1.0mm$	$\pm 2.5mN$	5%
F_z[1]	$10N$	$1.0mm$	$2.5mN$	2%

[1] Compression only

Experiments

Experiments have been performed in four cases in order to verify feasibility of this non-invasive camera-tissue contact force measurement approach: 1) Anchoring, 2) Translation, 3) Rotation, and 4) Robotic-assisted control. Each case represents one characteristic functional or application behavior of the *in vivo* camera during a surgical procedure.

Fig. 4.19 lays out the setup for these experiments. A test platform was built with aluminum T-slotted framing components, a clear acrylic sheet, and a viscoelastic rubber

Table 4.2: Physical attributes of the actuator and the camera

Symbol	Description	Value
Φ_h	Diameter of the hanger	$75mm$
Φ_s	Diameter of the stator	$100mm$
h_a	Actuator assembly height	$98mm$
m_s	Stator mass	$465g$
Φ_c	Diameter of the camera	$16mm$
l_c	Length of the camera	$81mm$
m_c	Camera mass	$37.5g$

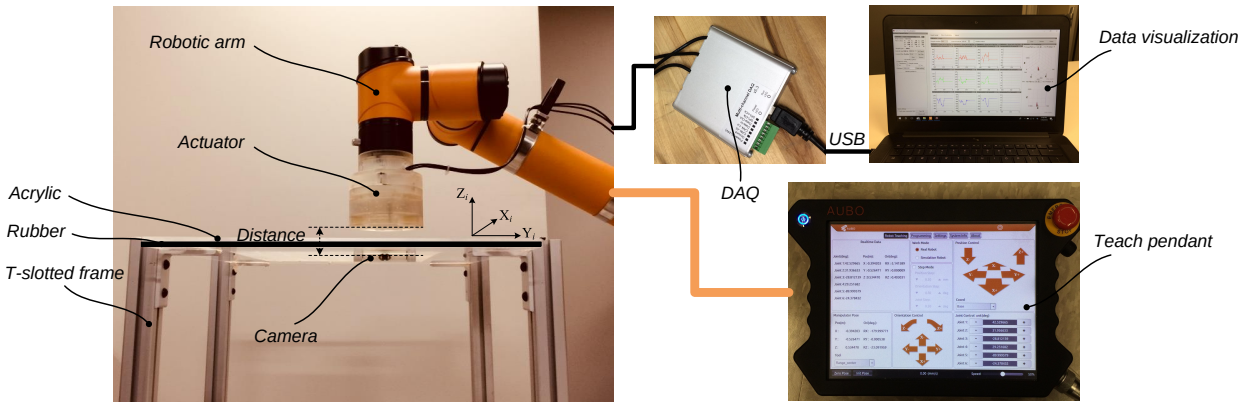

Figure 4.19: Experimental setup: the actuator was manipulated by the robotic arm, sensor measurements were visualized on a PC, and the robotic arm was controlled using the teach pendant. The inertial coordinated frame $X_iY_iZ_i$ was fixed on the base of the robotic arm with the X_iY_i plane parallel to the simulated abdominal wall and Z_i pointing upward.

sheet to represent the abdominal cavity. The acrylic sheet sitting on top of the T-slotted frame was a support layer and the super-cushioning rubber sheet attached to the bottom of the support layer was simulating the viscoelastic tissue property. The actuator was mounted on a collaborative lightweight robotic arm (AUBO-i5^{TM}) as an end-effector for robotic-assisted camera control. This collaborative robotic arm was capable of force sensing and collision detection, thus could work safely side by side with surgeons in the shared surgical environment. Position and orientation of the actuator could be controlled precisely at a resolution of 0.02mm and 0.01deg respectively. Measurements of the force sensors were acquired through a data acquisition unit (DAQ) at up to 1000Hz, visualized and processed on a laptop. Finally, the solved camera-tissue contact force was updated to the robotic arm controller for closed-loop force control feedback.

Anchoring

This experiment examined camera-tissue contact forces at different actuator-camera distances. The camera was anchored still to the abdominal wall throughout the experiment while the actuator was held right above the camera by the robotic arm. At the beginning, the actuator was placed at the closest distance of 18mm to the camera. Then, the actuator was moved up vertically at a step length of 0.5mm until the camera fell off at a distance of 68mm. The results were shown in Fig. 4.20, where the recovered camera-tissue contact force was plotted as a normal component $\boldsymbol{F_n}$ to the abdominal wall and a shear component $\boldsymbol{F_s}$ along the abdominal wall. The normal component was definitely dominant with a maximum force of -2285mN. The resultant camera-tissue contact force decayed exponentially as the camera-actuator distance increased, which agrees well with the exponential attenuation characteristic of magnetic fields.

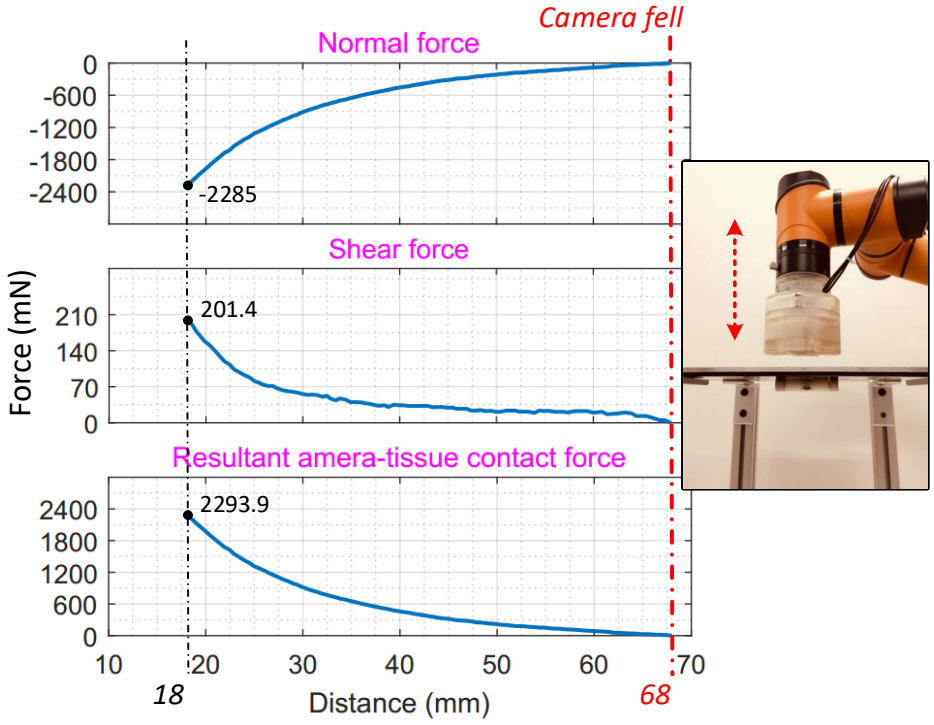

Figure 4.20: Anchoring experiment.

Translation

This experiment aimed to characterize the camera-tissue contact force during the translation process. As is shown in Fig. 4.21, the actuator began to move along X_i-axis at 3.6s and the camera began to move at 5.1s. During this period, the normal force was decreasing due to the fact that the actuator was moving away sideways. Meanwhile, the shear force was increasing which was reasonable since more attraction force to the camera was being exerted in the horizontal plane. When the horizontal force became large enough to overcome the static friction at 5.1s, the camera started to move. From 5.1s to 15s, the camera was translating as actuated. The camera stopped immediately when the actuator stopped at 15s and the resultant camera-tissue contact force decreased from 535mN to 500mN after this experiment.

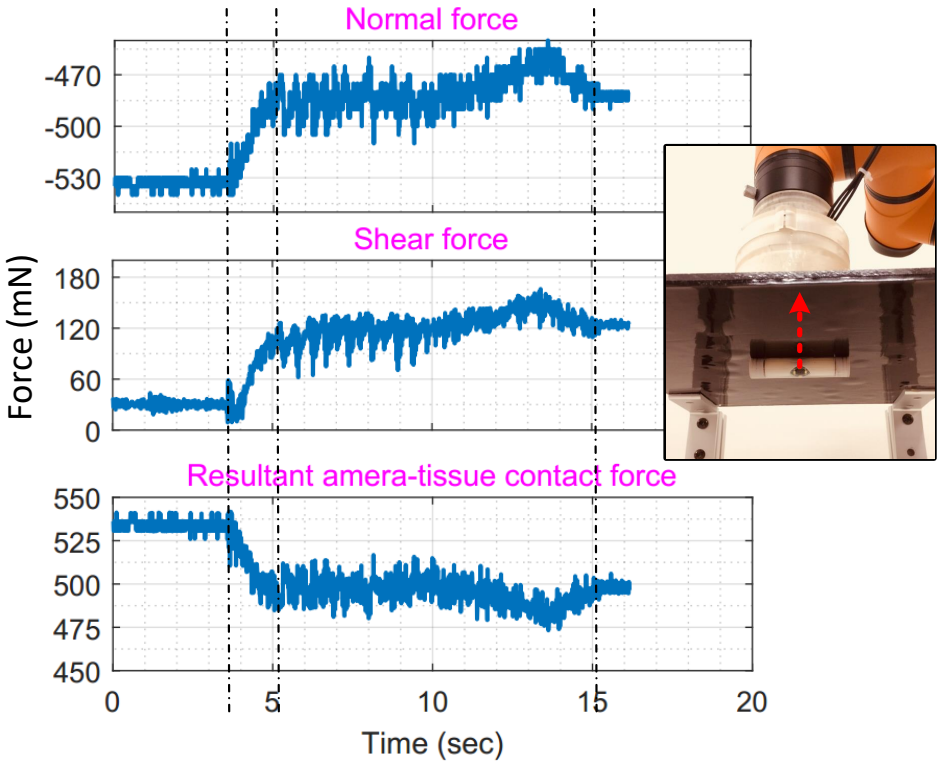

Figure 4.21: Translation experiment.

Rotation

Characteristics of the camera-tissue contact force during rotation were studied in this experiment. As the electrical board driving the tilt motor was not ready at the time of writing, the tilt experiment was saved for future. The camera was actuated to pan about Z_i-axis and Fig. 4.22 graphed the results. The actuator began to rotate at 5s and the camera began to pan at 11s. The normal component was decreasing until the camera started to move and the shear component was also decreasing during this period, which could be explained with similar reasons as the translation experiment. The actuator and the camera stopped at the same time at 26s. However, after the pan motion, the resultant camera-tissue contact force was increased by 30mN.

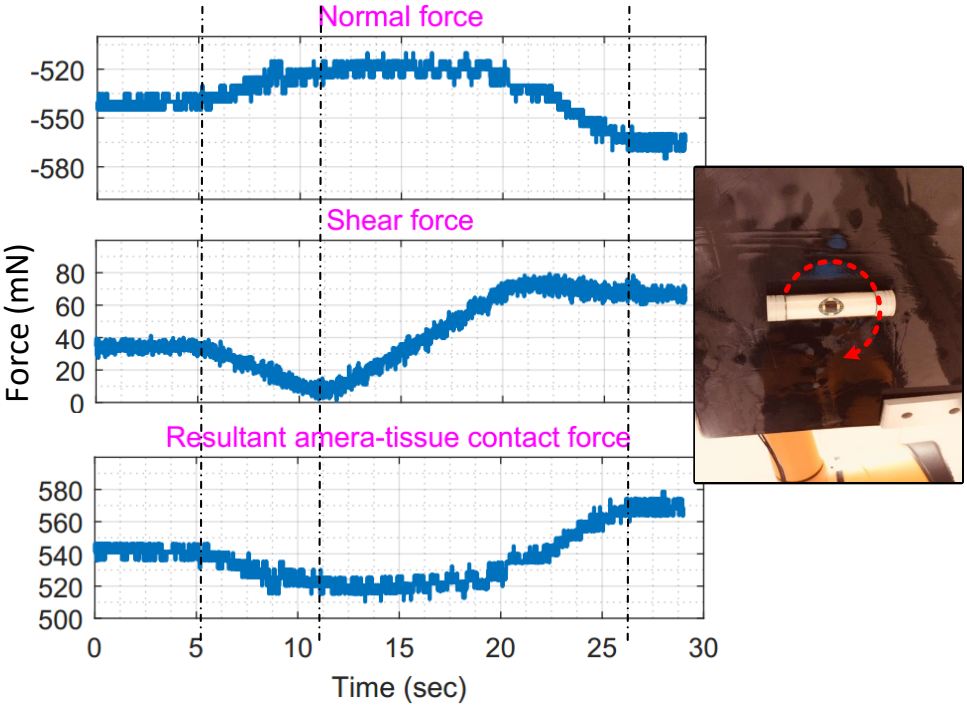

Figure 4.22: Pan experiment.

4.4 Summary

This chapter models and simulates the camera-tissue interaction process, through which the interaction force, the contact profile, and the stress distribution over the tissue surface have

been related to each other. Moreover, a non-invasive force measurement approach has been proposed, implemented, and verified for an insertable laparoscopic camera. Modeling and force analysis of the actuator-camera system require few kinematic or geometric assumptions, which makes it more applicable in clinical practice. The actuator and the camera have been fabricated using the rapid prototyping technology for experimental tests. Force measurement experiments have characterized the camera-tissue contact force and demonstrated the effectiveness of the approach. Potential surgical impacts enabled by the force feedback have also been exemplified by a robotic-assisted camera control experiment using shared autonomy in Chapter 6.

Chapter 5

Pose Estimation

5.1 Introduction

The potentially promising idea of bringing a miniaturized imaging device [17][58] and even other functional surgical units [16] entirely into the abdominal cavity in a robotic manner has initiated wide research efforts [32][33][25][26][28][39]. These *in vivo* robots provide vision and task assistance in a larger workspace under appropriate magnetic or motorized actuation, eliminating the trocar constraints. Up to date, several proof-of-concept prototypes of insertable laparoscopic imaging devices have been proposed to demonstrate their capabilities, kinematic flexibility, and relevant technical feasibility to different extents. These designs in essence are mostly magnetic anchoring and guidance systems (MAGS) [59] with [29][39][60][20] or without [61][62][32] tethering wires for power and communication. Compared to motorized solutions which need to be mechanically pieced into [27] or sutured onto [63] the abdominal wall for anchoring, magnetic coupling could facilitate more flexible *in vivo* camera mobility through non-contact transabdominal actuation. However, although the magnetic field could penetrate human body with little attenuation, its strength decreases exponentially with distance, which underlies poor camera controllability [64]. Especially in consideration of morbidly obese patients and complex viscoelastic camera-tissue interaction, it's easy to lose track of the camera because of backlash and sluggish effects, not to mention precise motion control.

Spatial information loss pertaining to standard laparosopes has drawn wide concerns from both surgeons and patients as it decreases surgical performance in terms of intuition, speed, and accuracy [5]. Since clinical monocular vision system mostly adopted for traditional LS only produces 2D images, this sharply impairs depth perception for surgeons during the operation, which may cause misoperations, thus jeopardize safety of patients.

Although a few state-of-the-art clinical laparoscopes [1] and on-going research prototypes [25][65] have shown feasibility to access 3D imagery by integrating two cameras there, they are still potentially losing useful spatial information of the laparoscopic camera which could lay foundation for robotic-assisted closed-loop control, depth inference, 3D structure reconstration, object motion detection and anatomical image registration still requires more efforts. Unfortunately, none of the state-of-the-art works have shown any ability in tracking the inserted laparoscopic camera. Visual servoing camera control loop closed by a human was being performed roughly without any knowledge of camera pose or motion in the surgical environment [64]. The motion control for the insterted laparoscope has been seriously challenged as there exist no physical connection to the laparoscope and no position or pose information of it.

It's worth noting that spatial information plays a critical part in surgical work flow as is reported in the literature [66][67]. Optical techniques based on laparoscopic vision have been able to reconstruct 3D organ surfaces [67][68] and track surgical instruments [69] with respect to camera coordinate frame. Therefore, knowledge of camera motion and pose could not only help stabilize laparoscopic imaging and provide feedback for precise camera control, but also facilitate operation planning and augment intraoperative navigation by registering the *in situ* recovered data to the robot coordinate frame or preoperative medical images.

As a first step towards pose estimation for insertable surgical devices, this section focuses on orientation estimation of the sCAM camera. Different from tracking wireless capsule endoscopes (WCEs) [70] with respect to the GI tract for precise diagnosis [71] where the targets locomote slowly and various techniques have been devised [72], orientation estimation for the magnetic-driven sCAM faces unique technical challenges. First, accurate orientation of the untethered camera needs to be estimated in a wireless manner under dynamic magnetic

[1] According to: http://medical.olympusamerica.com/products/laparoscopes/endoeye-flex-3d

interference from multiple movable permanent magnets. Second, real-time tracking should be achieved at an acceptable update rate for closed-loop control feedback requirement, unlike WCE localization which could even be post-processed off line by a human reviewer.

5.2 Problem Formulation

As is conceptually illustrated in Fig. 5.1, the sCAM system represents a robotic MAGS which consists of a camera rotor and an actuator stator. The stator is held by a lightweight collaborative robotic arm as an end effector. Borrowing the principle of spherical motors, the camera rotor is actuated to rotate (yaw, pitch, and roll) in a three-dimensional (3D) space by appropriately adjusting magnetic fields generated by the actuator stator. As is configured in Fig. 5.2, three movable external permanent magnets (EPMs) have been integrated on the stator. All these EPMs are installed on a stator core which could rotate with respect to the stator housing under motor actuation. In addition, the central external permanent magnet (cEPM) could rotate with respect to the end external permanent magnets (eEPMs).

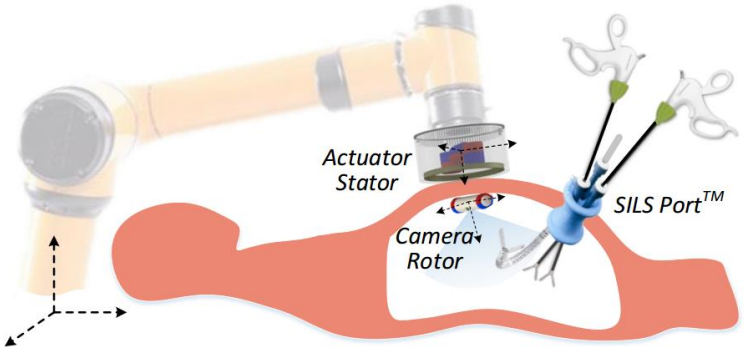

Figure 5.1: Concept of camera pose estimation with the sCAM system. An AUBO-i5™.

Real-time pose feedback with respect to the stator is critical for robotic precise motion control of this novel surgical camera. As is indicated in Fig. 5.1, the stator is held by the robotic arm as an end effector whose pose with respect to the robot base could be conveniently computed using forward kinematics. Meanwhile, the robot base is mounted at a known location in the operating room. Thus, the camera pose, once established, could be easily transformed between the stator coordinate frame and the world coordinate frame.

Many other surgical augmentations could be achieved after the camera pose is registered into the world coordinate frame in the operating room.

Although an attitude and heading reference system (AHRS) based on an inertial measurement unit (IMU) aided with a 3-axis magnetometer has been documented with different implementations, they are useful only in applications where the geomagnetic field can be clearly observed for heading reference. In order to compute pose of the sCAM in a strong dynamic magnetic environment for real-time control feedback, an effective approach must meet the following requirements: (i) the estimation should be able to robustly counteract magnetic interference, (ii) and the pose update rate needs to be agreeable for feedback-intensive control tasks, such as image stabilization.

5.3 Modeling Approach

According to the design and application environment, the camera is essentially a rigid body levitated inside the 3D abdominal cavity against soft tissues with 6 DoFs (3D translation and 3D rotation). Since we are initially focusing on the orientation estimation in this paper, kinematic modeling will be explained towards how to solve for the orientation of the camera.

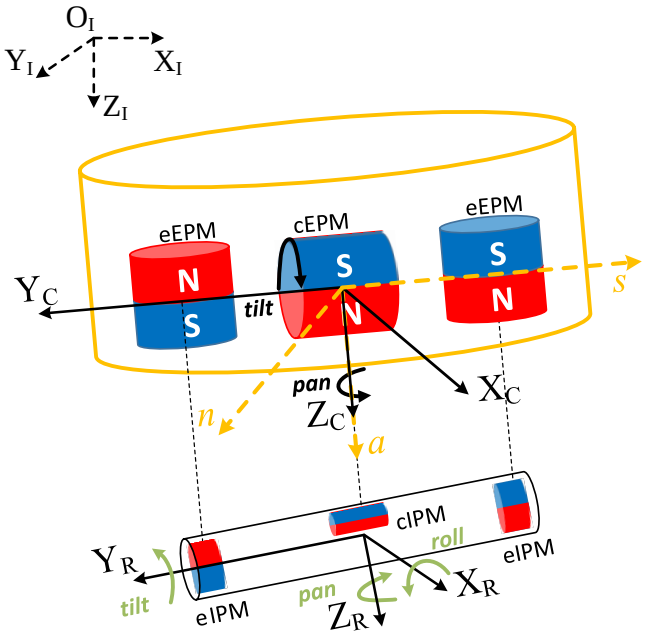

Figure 5.2: Schematic of magnet configuration and kinematic modeling.

Thus, the 3D general rotation differential equation of the camera will be investigated in the inertial coordinate frame.

In order to mathematically depict kinematic model of the sCAM system, a series of coordinate frames have been determined as is shown in the schematic Fig. 5.2. The world coordinate frame in the operating room is referred to as the inertial coordinate frame $O_iX_iY_iZ_i$. An robotic end effector frame is assigned to the stator housing, where a is the approaching direction, s represents the sliding direction, and n is determined by the right hand rule. Another coordinate frame $O_CX_CY_CZ_C$ is attached to the stator core on which all EPMs are siting. The stator core frame coincides with the end effector frame at the center of the cEPM and could pan (θ_p) with respect to the end effector frame about Z_C/a axis. Meanwhile, the cEPM could tilt (θ_t) about Y_C axis according to the design principle. Most of all, a body coordinate frame $O_RX_RY_RZ_R$ of the rotor is established with its origin at the center of the rotor, Z_R axis pointing the camera view direction, Y_R axis in the longitudinal direction, and X_R determined by the right hand rule. Besides, sensor axes of the onboard IMU are all aligned with the rotor body coordinate frame.

For attitude description of the sCAM in a 3D space, Euler angles are more intuitive and easy to use in terms of control purposes. According to different rotation sequences, there exist 12 sets of Euler angels. Unless specified otherwise, the Z-X-Y set of Euler angels (ψ, θ, ϕ) will be used in this work, which is considered one of the most appropriate sets for depicting pan, roll, and tilt of the *in vivo* camera. With angular rate vector Ω^R measured in the rotor coordinate frame, the rotation differential equation of Euler angles could be given as 5.2. However, as $cos\theta$ approaches zero, solution accuracy of 5.2 degrades quickly, which implies this equation is not able to work in the full attitude space.

$$\Omega^R = (\omega_x^R, \omega_y^R, \omega_z^R)^T \tag{5.1}$$

$$\begin{bmatrix} \dot{\psi} \\ \dot{\theta} \\ \dot{\phi} \end{bmatrix} = \frac{1}{cos\theta} \begin{bmatrix} sin\theta & 0 & -cos\theta \\ cos\theta cos\phi & 0 & cos\theta sin\phi \\ sin\theta sin\phi & 1 & sin\theta cos\phi \end{bmatrix} \begin{bmatrix} \omega_x^R \\ \omega_y^R \\ \omega_z^R \end{bmatrix} \tag{5.2}$$

In order to eliminate the singularity problem with 5.2, quaternions Q have been chosen for formulation of the rotation differential equation 5.5, which works in the full attitude space with similar computation complexity. After the orientation is calculated, it's easy to convert quaternions and Euler angles to each other using 5.6 and 5.7

$$Q = \begin{bmatrix} q_0 & q_1 & q_2 & q_3 \end{bmatrix}^T \tag{5.3}$$

$$\frac{dQ(t)}{t} = f[Q(t), \Omega^R(t)] \tag{5.4}$$

$$\begin{bmatrix} \dot{q_0} \\ \dot{q_1} \\ \dot{q_2} \\ \dot{q_3} \end{bmatrix} = \frac{1}{2} \begin{bmatrix} 0 & -\omega_x^R & -\omega_y^R & -\omega_z^R \\ \omega_x^R & 0 & \omega_z^R & -\omega_y^R \\ \omega_y^R & -\omega_z^R & 0 & \omega_x^R \\ \omega_z^R & \omega_y^R & -\omega_x^R & 0 \end{bmatrix} \begin{bmatrix} q_0 \\ q_1 \\ q_2 \\ q_3 \end{bmatrix} \tag{5.5}$$

$$\begin{bmatrix} \theta \\ \phi \\ \psi \end{bmatrix} = \begin{bmatrix} arcsin(2(q_2q_3 + q_2q_3)) \\ arctan(-\dfrac{2(q_1q_3 - q_0q_2)}{q_0^2 + q_3^2 - q_1^2 - q_2^2}) \\ arctan(\dfrac{2(q_1q_2 - q_0q_3)}{q_0^2 + q_2^2 - q_1^2 - q_3^2}) \end{bmatrix} \tag{5.6}$$

$$\begin{bmatrix} q_0 \\ q_1 \\ q_2 \\ q_3 \end{bmatrix} = \begin{bmatrix} cos\frac{\psi}{2}cos\frac{\theta}{2}cos\frac{\phi}{2} - sin\frac{\psi}{2}sin\frac{\theta}{2}sin\frac{\phi}{2} \\ cos\frac{\psi}{2}sin\frac{\theta}{2}cos\frac{\phi}{2} - sin\frac{\psi}{2}cos\frac{\theta}{2}sin\frac{\phi}{2} \\ sin\frac{\psi}{2}sin\frac{\theta}{2}cos\frac{\phi}{2} + cos\frac{\psi}{2}cos\frac{\theta}{2}sin\frac{\phi}{2} \\ sin\frac{\psi}{2}cos\frac{\theta}{2}cos\frac{\phi}{2} + cos\frac{\psi}{2}sin\frac{\theta}{2}sin\frac{\phi}{2} \end{bmatrix} \tag{5.7}$$

5.4 Filtering Algorithm

According to the kinematic analysis, quaternions of the camera have been chosen as state variables of the filtering algorithm. Since we have redundant measurements to update the

same state variables of interest independently, a complementary filter has been devised for fusing these data from multiple sensors. Fig. 5.3 presents structure of the complementary filter implemented using RK1 (first order Runge-Kutta method) for time update process and DCM (Direction Cosine Matrix) for measurement update process.

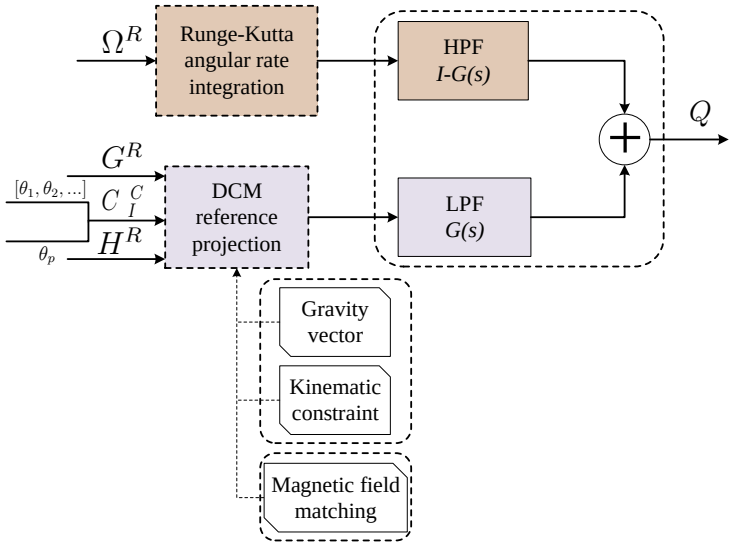

Figure 5.3: Structure of the implemented complementary filter.

During one step time update, RK1 provides a numerical solution to the rotation differential equation using its first-order taylor expansion as 5.8. This time update process gives accurate state prediction based on integration of angular rates in a short period of time but drifts due to cumulative integration errors.

$$\begin{bmatrix} q_0 \\ q_1 \\ q_2 \\ q_3 \end{bmatrix}_{t+\Delta t} = \begin{bmatrix} q_0 \\ q_1 \\ q_2 \\ q_3 \end{bmatrix}_t + \frac{\Delta t}{2} \begin{bmatrix} 0 & -\omega_x^R & -\omega_y^R & -\omega_z^R \\ \omega_x^R & 0 & \omega_z^R & -\omega_y^R \\ \omega_y^R & -\omega_z^R & 0 & \omega_x^R \\ \omega_z^R & \omega_y^R & -\omega_x^R & 0 \end{bmatrix}_t \begin{bmatrix} q_0 \\ q_1 \\ q_2 \\ q_3 \end{bmatrix}_t \tag{5.8}$$

Therefore, the measurement update process which could correct integration errors is necessary for a stable estimation in the long run. The gravity vector G^I would be measured as G^R in the rotor coordinate frame, projected by the DCM matrix determined by camera orientation 5.9. Tilt and roll angles could be solved from 5.9 as 5.10 and 5.11, which prevents θ and ϕ from drifting. However, the vertical reference can not help converge ψ, since the pan

angle doesn't affect projection of a vertical vector to the rotor coordinate frame as indicated by the third column of C_I^R.

In order to solve for the pan angle, another independent reference needs to be found. According to the design principle of the sCAM system, it's reasonable to assume that Y^R is perpendicular to X_C, which would give us a virtual kinematic constraint for heading reference. It's easy to calculate DCM (C_I^C) of the stator core coordinate frame using forward kinematics based on joint variables of the robotic arm and the pan angle θ_p of the stator core. Suppose Euler angles of the core coordinate frame are ψ_c, θ_c, and ϕ_c, C_I^C would be calculated as 5.12. Hence, the heading reference constraint could be formulated as 5.13, where $e_{Y_R}^R$ and $e_{x_C}^C$ are respectively standard basis vectors of the rotor coordinate frame and the stator core coordinate frame. Substituting 5.10, 5.11, and 5.12 into 5.13, ψ is solved as 5.14, where a, b, and c are all given in 5.15. In this way, integration error of ψ could be corrected without using the local geomagnetic vector as heading reference, which makes the estimation robust to dynamic magnetic fields. However, it's worth noting that the kinematic heading constraint is not rigid since the camera is actuated by magnetic coupling. To make the heading estimation ψ accurate, one potential solution lies in magnetic field registration based on measurements of onboard magnetometers.

Finally, the time update and the measurement update are fused with a CF made up of a high-pass filter and a low-pass filter. The sum of the transfer functions should be I, which reflects their complementary attributes. Performance of the filter could be tuned by adjusting the scale of $G(s)$ to make the fused estimation trust one update more and the other less so that a good balance can be found between high frequency and low frequency responses.

$$\begin{bmatrix} g_x^R \\ g_y^R \\ g_z^R \end{bmatrix} = \begin{bmatrix} c\phi c\psi & -c\phi s\psi + s\phi c\psi s\theta & -s\phi c\theta \\ s\psi c\theta & c\psi c\theta & s\theta \\ s\phi c\psi - c\phi s\psi s\theta & -s\phi s\psi - c\phi c\psi s\theta & c\phi c\theta \end{bmatrix} \begin{bmatrix} 0 \\ 0 \\ g \end{bmatrix} \tag{5.9}$$

$$\theta = -arcsin(\frac{g_y^R}{g}) \tag{5.10}$$

$$\phi = -arctan(\frac{g_x^R}{g_z^R}) \tag{5.11}$$

$$C_I^C = \begin{bmatrix} c\phi_c c\psi_c & -c\phi_c s\psi_c + s\phi_c c\psi_c s\theta_c & -s\phi_c c\theta_c \\ s\psi_c c\theta_c & c\psi_c c\theta_c & s\theta_c \\ s\phi_c c\psi_c - c\phi_c s\psi_c s\theta_c & -s\phi_c s\psi_c - c\phi_c c\psi_c s\theta_c & c\phi_c c\theta_c \end{bmatrix} \tag{5.12}$$

$$((C_I^R)^T e_{y_R}^R)^T \cdot (C_I^C)^T e_{x_C}^C = 0 \tag{5.13}$$

$$\psi = arcsin(\frac{ac \pm b\sqrt{a^2+b^2-c^2}}{a^2+b^2}) \tag{5.14}$$

$$\begin{bmatrix} a \\ b \\ c \end{bmatrix} = \begin{bmatrix} c\theta c\phi_c c\psi_c \\ c\theta(s\phi_c c\psi_c s\theta_c - c\phi_c s\psi_c) \\ s\theta s\theta_c c\theta_c \end{bmatrix} \tag{5.15}$$

DCMs are used to project gravity and heading references to desired coordinate frames, which offers converged observation of state variables in the long run and helps correct integration errors.

5.5 Software Design

A framework of software design for the sCAM orientation estimation is given in Fig. 5.4. There are three primary tasks in software implementation: wireless IMU measurements acquisition, CF filtering for orientation estimation, and results visualization.

Bluetooth low energy (BLE) features low power consumption with an agreeable data rate for IMU raw data acquisition over-the-air. A private BLE profile based on TI BLE stack has been developed specifically for this sCAM application. This sCAM profile runs on a cc2541 system-on-chip solution for BLE, which has been integrated onboard the sCAM and samples IMU measurements in real time. Therefore, the sCAM could be connected to a

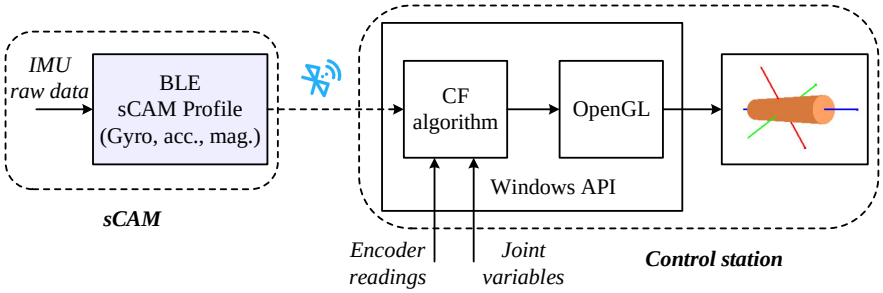

Figure 5.4: Framework of software implementation.

master BLE device on the control station and provide multiple application services. Inertial measurement data could be read by the control station through requesting the IMU service.

With the IMU raw data acquired, data procession of the CF algorithm is implemented using C++ based on windows APIs on the control station. Since the robotic arm and the stator has been integrated with the control station, joint variables of the robotic arm and encoder readings are naturally accessible for use. Finally, to make the estimated orientation visible for reference, a rigid body of the sCAM is rendered using the OpenGL technique which supports hardware-accelerated 3D rendering.

5.6 Implementation and Experiments

The implemented pose estimation has been incorporated into the sCAM_app software program as is shown in Fig. 5.5. The sCAM_app was developed to provide a convenient user interface for testing the sCAM system at the developing stage. The laparoscopic vision, the visualized camera pose, as well as the Euler angle plot were displayed in real time. Meanwhile, this app helps set up the sCAM, send control commands, read camera messages, and monitor camera health. The camera orientation was updated at $30Hz$ with a resolution of 0.1^o.

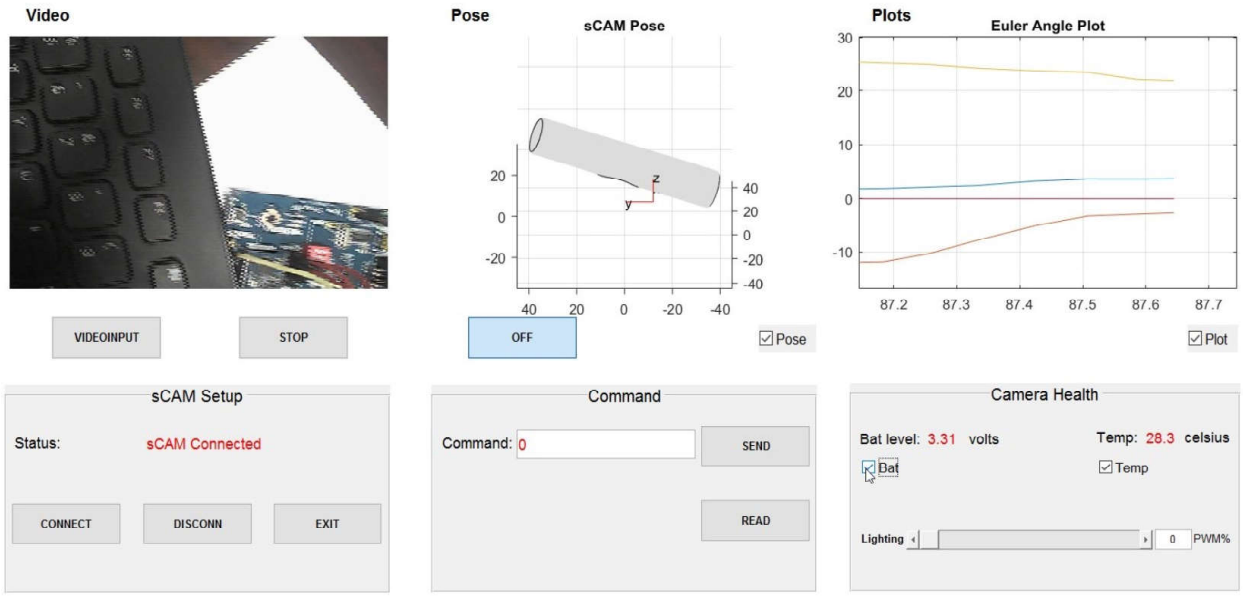

Figure 5.5: sCAM_app software program.

5.7 Summary

This chapter presents the approach towards pose estimation of an insertable laparoscopic camera. A complementary filter specifically customized for this application fuses motion information of the *in vivo* camera measured by an onboard IMU aided by a kinematic heading constraint. The kinematic modeling of the camera is performed using quaternions in a 3D space and the numerical solution to the quaternion differential equation is achieved using RK1. Raw IMU data is accessed through requesting the BLE IMU service and the estimated optimal camera pose is visualized for reference. The camera orientation could be updated at $30Hz$ with a resolution of 0.1^o. The orientation estimation detailed in this chapter is actually only a first step towards pose estimation of the sCAM. Position estimation based on magnetic registration will be realized in near future. Jointly, the estimated orientation and position could lay foundation for advanced laparoscopic vision augmented by spatial information.

Chapter 6

Robotic-Assisted Control

6.1 Introduction

Manipulation of MIS instruments has been recognized as a difficult task even for the most experienced surgeons since the very beginning. Traditional trocar-based laparoscopic instruments feature counter-intuitive manual control and usually necessitate a well-trained laparoscopist to share the surgeon's workload, which increases the cooperation cost and results in a crowded surgery table during the operation.

Robotic-assisted medicine has been a clear future of modern medical science with an increasing series of robots dedicated for various diagnostic or operative procedures. The complex instrument movements have been mapped to an intuitive surgeon interface through these robotic systems which allows the surgeon to focus on the surgical tasks with improved efficiency. Therefore, it's advisable to root the next-generation laparoscopic camera deep in robotics so as to carry forward precision, intuitiveness, and automation in surgical imaging.

From the clinical point of view, the sCAM robot should be able to provide a comfortable surgical view according to the surgeon's desire with intuitive operation as well as guaranteed patient safety. The surgical view is determined by the camera pose while the safety is determined by the camera tissue interaction force, or rather the stresses on the deformed tissues. Therefore, the robotic-assisted control aims to provide an intuitive surgeon interface of the laparoscopic view manipulation with automated pose and force control based on

the force measurement and pose estimation work elaborated respectively in Chapter 4 and Chapter 5.

6.2 Control System Design

6.2.1 Double-Loop Control Structure

As is shown in Fig. 6.1, the robotic-assisted control system for the sCAM robot has been designed in a double-loop structure. The outer loop controls the camera pose taking the pose corresponding to the desired laparoscopic view as reference. Real-time pose estimation results filtered by the complementary filtering algorithm described in Section 5.4 provides feedback for this pose control loop. Meanwhile, the inner loop guarantees the surgical safety by governing the camera-tissue interaction force facilitated by non-invasive force measurement detailed in Section 4.3.

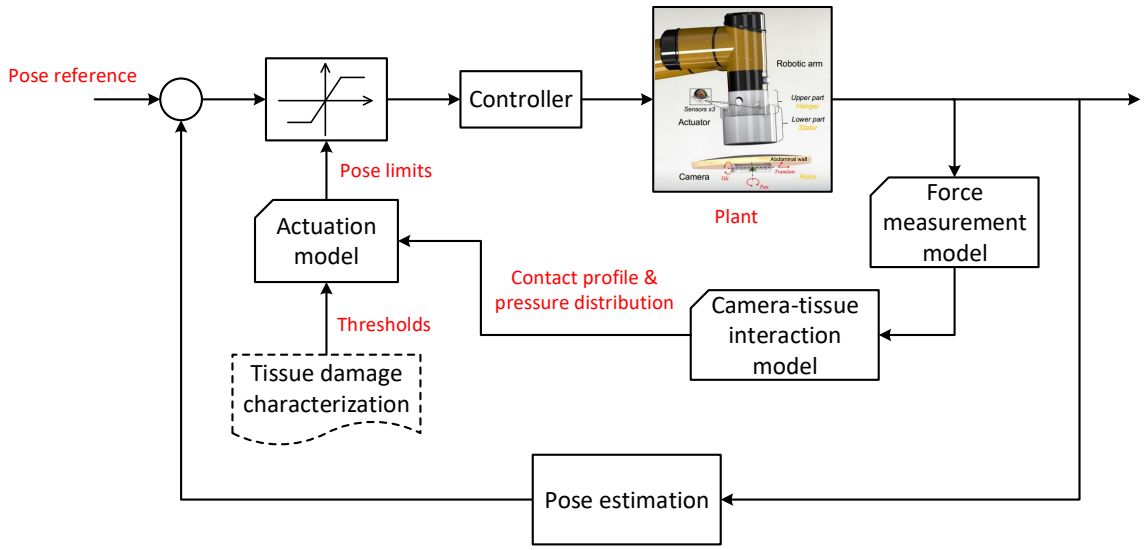

Figure 6.1: Schematic of the robotic-assisted control system.

6.2.2 Shared Surgeon-Robot Autonomy

Different degrees of autonomy could be allowed for robotic-assisted surgery with the two extremes of full autonomy or pure teleoperation. One feasible intermediate approach is

the shared autonomy where free manipulation is allowed for surgeons within a predefined safe range in the robotic control scheme. This concept has been adopted for the double-loop controller, where the surgeon could manipulate the laparoscopic view freely within predefined tissue stress thresholds without worrying about the interaction force.

As is shown in Fig. 6.1, the surgeon's manipulation is incorporated into the outer loop as a desired pose reference while the inner loop actually generates pose limits to the pose reference according to the tissue damage thresholds. Any desired pose falling in the limits will be approximated to by the controller while poses beyond the limits will be prevented. In order to make this possible, the relation between the tissue damage and the stress level needs to be studied to find the proper thresholds. The stress distribution and the camera-tissue contact profile are updated in real time facilitated by the non-invasive force measurement feedback and camera-tissue interaction modeling detailed in Chapter 4. Then, the thresholds and the stress distribution are fed into the actuation model of the sCAM system and the pose limits are predicted to correct the pose reference. Finally, a comfortable laparoscopic view for surgeons could be achieved with guaranteed surgical safety for this sCAM.

6.3 Initial Experiments

An initial experiment was performed to show the feasibility of this robotic-assisted laparosopic camera controller. The experimental setup was the same as shown in Fig. 4.19, where the camera was being actuated by the stator held with a collaborative robotic arm. A temporary user interface was provided with the teach pendant for manipulation of the camera. Since there exists no documented study on the stress-damage correlation for the abdominal wall tissue [55] and no statistically significant thresholds are available, a safe range of camera-tissue contact force was set between 0.4N and 1.0N and programmed into the robotic controller at this point. During the experiment, the actuator was being moved up and down to see how the controller was performing. As is shown in Fig. 6.2, when the camera-tissue contact force reached the thresholds, the robotic control took effect and kept the actuator from going further in the unsafe direction and the camera-tissue contact force has been reliably limited within the safe range with an error of 10mN. Hence, the surgeon

could focus on his surgical operation and manipulate the sCAM freely without concerning that the camera might fall off or damage the tissue.

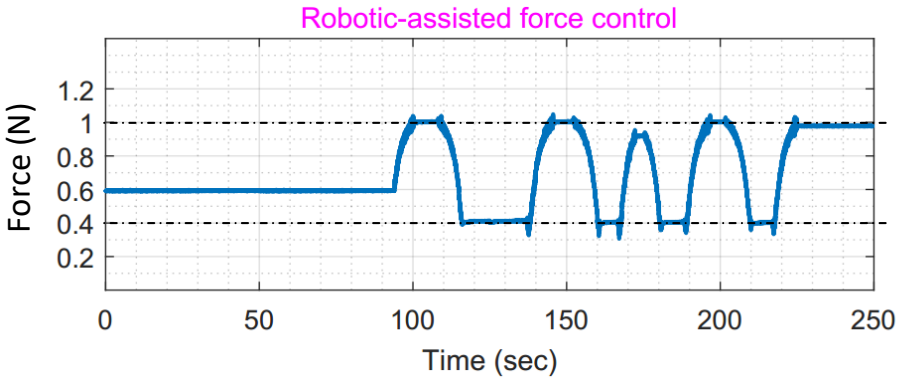

Figure 6.2: Robotic-assisted force control results.

6.4 Summary

In this chapter, robotic-assisted control for the sCAM is designed, whose effectiveness has been shown with some initial test results. Facilitated by force measurement and pose estimation respectively realized in Chapter 4 and Chapter 5, robotic-assisted closed-loop camera camera control has been realized with a double-loop controller. The shared autonomy between the surgeon and the robotic controller guarantees that the surgeon could manipulate the camera pose freely without concerning that the camera might fall off or damage the tissue. Due to the too much programming work, only initial test results are available for now, which have shown effectiveness of the robotic-assisted control design.

Chapter 7

Conclusions and Future Work

7.1 Conclusions

This dissertation has presented a novel fully insertable robotic laparoscoic surgical camera (sCAM), which features no tethering wires, wireless vision and control, as well as non-contact transabdomial actuation. The robotic design and implementation of the sCAM system provide hardware and software technological references for developing fully insertable medical devices and validate feasibility of an untehtered fully insertable laparoscopic surgical camera. The camera-tissue interaction process has been carefully investigated and a non-invasive force measurement approach has been proposed, implemented and verified. Modeling and force analysis of the actuator-camera system require few kinematic or geometric assumptions, which makes it more applicable in clinical practice. Force measurement experiments have characterized the camera-tissue contact force and demonstrated the effectiveness of the approach. Work from this dissertation also contributes an orientation estimation solution for the sCAM robot. The camera pose has been estimated using a complementary filter specifically implemented for this application. For the first time, the pose information becomes available for a fully insertable laparoscopoic surgical camera to assist closed-loop camera manipulation. Facilitated by the force measurement and pose estimation, robotic-assisted closed-loop camera control has been realized in a double-loop control structure with shared autonomy between surgeons and the robotic controller. A comfortable laparoscopic view is precisely maintained with guaranteed surgical safety.

7.2 Future Work

Currently, the sCAM is a proof-of-concept prototype whose technical feasibility and functions have been experimentally verified ex vivo in laboratory settings. Several issues are still open before the sCAM could finally reach clinical practice and more future work will be done to augment the developed prototype.

7.2.1 Tissue Damage Assessment

The shared autonomy control in Chapter 6 requires an effective tissue damage-stress correlation which will accurately provide the damage thresholds in terms of not only the stress magnitude but also the stress duration. However, due to the lack of documented exploration, a statistically significant damage-stress correlation for the abdominal wall tissue is still an open question. Moreover, the correlation could be patient-dependent and there might be a big difference between the excised tissues and the alive tissues. Thus, to find the appropriate thresholds, statistical tissue damage assessment in terms of stress magnitude and stress duration needs to be performed on alive tissues *in vivo*.

7.2.2 Transabdominal Wireless Powering

Onboard battery power adopted for now was able to sustain the camera for a limited scope of laparoscopic procedures. For more procedures with complex operations, the battery life needs to be extended. Another feature under development for the sCAM is transabdominal wireless powering which could extend the battery life or even completely eliminate the powering problem. Wireless power transmission based on magnetic induction or magnetic resonance is emerging quickly in consumer electronics for wireless charging. However, its application in powering *in vivo* medical devices still needs more investigation since the electromagnetic field could be substantially attenuated by the tissues. The transmitting and receiving coils need to be tailored to respectively fit into the stator and the rotor with sufficient power transmission efficiency. Relevant experiments will validate the transabdominal wireless powering performance and shed some light on the biomedical safety effects of using wireless electromagnetic field across human body.

7.2.3 Audio Sensing and Feedback

Current clinical robotic surgical systems provide limited if not no haptic feedback because the interaction between surgical instruments and human organ tissue is difficult to measure and display. One next step is to incorporate audio sensing and feedback to the sCAM, which, as reported [51], plays a very helpful role in improving surgical perception and operating confidence by allowing surgeons to hear the sounds of palpation, cutting, dissection, removal, as well as instrument vibration.

7.2.4 In Vivo and Clinical Tests

The sCAM system is now at a prototyping stage and needs more evaluation to further validate and improve the current design. In order to bring this device toward clinical application, *in vivo* and clinical tests will be performed. These tests will begin with a porcine and a synthetic human cadaver, which will provide preparation knowledge before it finally reaches clinical trials on human subjects.

7.2.5 Augmented Laparoscopic Vision

Another step in improving the current design is to augment the laparoscoic vision with the estimated pose information of the camera. The depth information and 3D surfaces in the surgical environment could be restored from the laparoscopic vision aided by the camera motion information using the sturcture from motion (SfM) technique. Moreover, the reconstructed 3D surgical environment could be registered into the world coordinate system through the camera pose estimation results, which facilitates intra-operative surgical planning and navigation.

7.2.6 A Family of Them

Last but not least, based on the technologies from the sCAM development in this dissertation, a long term ultimate goal is to develop a family of fully insertable laparoscopic surgical robots dedicated for different functions. Although the development of fully insertable laparoscopic

devices starts with the laparoscopic camera, the other laparoscopic surgical instruments could also be minimized using the similar technologies to finally push a systematic solution entirely into the surgical area, shaping the next generation of laparoscopic surgical instrumentation and advancing the state of the art in MIS.

Bibliography

[1] W. S. Richardson, K. M. Carter, G. M. Fuhrman, J. S. Bolton, and J. C. Bowen, "Minimally invasive abdominal surgery," *The Ochsner Journal*, vol. 2, no. 3, pp. 153–157, 2000. 1

[2] L. Y. Wu and D. C. C. Foo, "Single-incision laparoscopic surgery: an update of current evidence," *Annals of Laparoscopic and Endoscopic Surgery*, vol. 1, no. 1, 2016. 3

[3] M. C. Cavusoglu, F. Tendick, M. Cohn, and S. S. Sastry, "A laparoscopic telesurgical workstation," *IEEE Transactions on Robotics and automation*, vol. 15, no. 4, pp. 728–739, 1999. 3

[4] T. E. Udwadia, "Single-incision laparoscopic surgery: An overview," *Journal of minimal access surgery*, vol. 7, no. 1, p. 1, 2011. 3

[5] H. Xin, J. Zelek, and H. Carnahan, "Laparoscopic surgery, perceptual limitations and force: A review," in *First Canadian student conference on biomedical computing*, vol. 6, 2006. 3, 6, 7, 53, 82

[6] J. F. Zhu, "Which term is better: Sils, spa, less, e-notes, or tues?," *Surgical endoscopy*, vol. 23, no. 5, pp. 1164–1165, 2009. 3

[7] I. S. Zeltser, R. Bergs, R. Fernandez, L. Baker, R. Eberhart, and J. A. Cadeddu, "Single trocar laparoscopic nephrectomy using magnetic anchoring and guidance system in the porcine model," *The Journal of urology*, vol. 178, no. 1, pp. 288–291, 2007. 3, 4

[8] A. A. Haris R Shaikh, Mufaddal Mahesri and H. R. Salahuddin, "A comparison of single incision laparoscopic cholecystectomy with the gold standard: is this the next procedure of choice?," *SAGES 2011 Abstracts*, 2011. 3

[9] B. F. Santos, D. Enter, N. J. Soper, and E. S. Hungness, "Single-incision laparoscopic surgery (sils) versus standard laparoscopic surgery: a comparison of performance using a surgical simulator," *Surgical endoscopy*, vol. 25, no. 2, pp. 483–490, 2011. 3

[10] J. P. Pearl and J. L. Ponsky, "Natural orifice transluminal endoscopic surgery: Past, present and future," *Journal of minimal access surgery*, vol. 3, no. 2, p. 43, 2007. 3

[11] J. Cadeddu and J. Gahan, "Magnetic anchoring and guidance systems (mags)," 2013. 3, 4, 6, 9, 42

[12] P. F. Escobar, G.-P. Haber, J. Kaouk, M. Kroh, S. Chalikonda, and T. Falcone, "Single-port surgery: laboratory experience with the davinci single-site platform," *JSLS: Journal of the Society of Laparoendoscopic Surgeons*, vol. 15, no. 2, p. 136, 2011. 3

[13] G. Dakin and M. Gagner, "Comparison of laparoscopic skills performance between standard instruments and two surgical robotic systems," *Surgical Endoscopy And Other Interventional Techniques*, vol. 17, no. 4, pp. 574–579, 2003. 3

[14] D. Nio, W. Bemelman, K. d. Boer, M. Dunker, D. Gouma, and T. Gulik, "Efficiency of manual versus robotical (zeus) assisted laparoscopic surgery in the performance of standardized tasks," *Surgical Endoscopy and Other Interventional Techniques*, vol. 16, no. 3, pp. 412–415, 2002. 3

[15] N. Greaves and J. Nicholson, "Single incision laparoscopic surgery in general surgery: a review," *The Annals of The Royal College of Surgeons of England*, vol. 93, no. 6, pp. 437–440, 2011. 4, 15

[16] G. Tortora, P. Dario, and A. Menciassi, "Array of robots augmenting the kinematics of endocavitary surgery," *IEEE/ASME transactions on mechatronics*, vol. 19, no. 6, pp. 1821–1829, 2014. 4, 9, 81

[17] M. E. Rentschler, J. Dumpert, S. R. Platt, K. Lagnemma, D. Oleynikov, and S. M. Farritor, "Modeling, analysis, and experimental study of in vivo wheeled robotic mobility," *IEEE Transactions on Robotics*, vol. 22, no. 2, pp. 308–321, 2006. 4, 8, 54, 57, 61, 81

[18] K. Harada, D. Oetomo, E. Susilo, A. Menciassi, D. Daney, J.-P. Merlet, and P. Dario, "A reconfigurable modular robotic endoluminal surgical system: vision and preliminary results," *Robotica*, vol. 28, no. 2, pp. 171–183, 2010. 4

[19] S. Park, R. A. Bergs, R. Eberhart, L. Baker, R. Fernandez, and J. A. Cadeddu, "Trocar-less instrumentation for laparoscopy: magnetic positioning of intra-abdominal camera and retractor," *Annals of Surgery*, vol. 245, no. 3, p. 379, 2007. 4

[20] S. R. Platt, J. A. Hawks, and M. E. Rentschler, "Vision and task assistance using modular wireless in vivo surgical robots," *IEEE Transactions on Biomedical Engineering*, vol. 56, no. 6, pp. 1700–1710, 2009. 6, 8, 9, 12, 42, 81

[21] D. R. Fletcher, M. S. Hobbs, P. Tan, L. J. Valinsky, R. L. Hockey, T. J. Pikora, M. W. Knuiman, H. J. Sheiner, and A. Edis, "Complications of cholecystectomy: risks of the laparoscopic approach and protective effects of operative cholangiography: a population-based study.," *Annals of surgery*, vol. 229, no. 4, p. 449, 1999. 7

[22] O. S. Bholat, R. S. Haluck, W. B. Murray, P. J. Gorman, and T. M. Krummel, "Tactile feedback is present during minimally invasive surgery 1," *Journal of the American College of Surgeons*, vol. 189, no. 4, pp. 349–355, 1999. 7

[23] R. Brydges, H. Carnahan, and A. Dubrowski, "Surface exploration using laparoscopic surgical instruments: The perception of surface roughness," *Ergonomics*, vol. 48, no. 7, pp. 874–894, 2005. 7

[24] T. Hu, P. K. Allen, N. J. Hogle, and D. L. Fowler, "Insertable surgical imaging device with pan, tilt, zoom, and lighting," *The International Journal of Robotics Research*, 2009. 7, 14

[25] D. L. Fowler, T. Hu, T. Nadkarni, P. K. Allen, and N. J. Hogle, "Initial trial of a stereoscopic, insertable, remotely controlled camera for minimal access surgery," *Surgical endoscopy*, vol. 24, no. 1, p. 9, 2010. 7, 81, 82

[26] C. A. Castro, A. Alqassis, S. Smith, T. Ketterl, Y. Sun, S. Ross, A. Rosemurgy, P. P. Savage, and R. D. Gitlin, "A wireless robot for networked laparoscopy," *IEEE Transactions on Biomedical Engineering*, vol. 60, no. 4, pp. 930–936, 2013. 7, 14, 81

[27] C. A. Castro, S. Smith, A. Alqassis, T. Ketterl, Y. Sun, S. Ross, A. Rosemurgy, P. P. Savage, and R. D. Gitlin, "Marvel: A wireless miniature anchored robotic videoscope for

expedited laparoscopy," in *Robotics and Automation (ICRA), 2012 IEEE International Conference on*, pp. 2926–2931, IEEE, 2012. 7, 81

[28] M. Simi, M. Silvestri, C. Cavallotti, M. Vatteroni, P. Valdastri, A. Menciassi, and P. Dario, "Magnetically activated stereoscopic vision system for laparoendoscopic single-site surgery," *IEEE/ASME Transactions on Mechatronics*, vol. 18, no. 3, pp. 1140–1151, 2013. 8, 14, 81

[29] M. Simi, G. Sardi, P. Valdastri, A. Menciassi, and P. Dario, "Magnetic levitation camera robot for endoscopic surgery," in *Robotics and Automation (ICRA), 2011 IEEE International Conference on*, pp. 5279–5284, IEEE, 2011. 8, 81

[30] M. E. Rentschler, J. Dumpert, S. R. Platt, K. Iagnemma, D. Oleynikov, and S. M. Farritor, "An in vivo mobile robot for surgical vision and task assistance," *Journal of Medical Devices*, vol. 1, no. 1, pp. 23–29, 2007. 8, 14

[31] G. Tortora, A. Dimitracopoulos, P. Valdastri, A. Menciassi, and P. Dario, "Design of miniature modular in vivo robots for dedicated tasks in minimally invasive surgery," in *Advanced Intelligent Mechatronics (AIM), 2011 IEEE/ASME International Conference on*, pp. 327–332, IEEE, 2011. 9, 14

[32] H. Feng, D. Dong, T. Ma, J. Zhuang, Y. Fu, Y. Lv, and L. Li, "Development of an in vivo visual robot system with a magnetic anchoring mechanism and a lens cleaning mechanism for laparoendoscopic single-site surgery (less)," *The International Journal of Medical Robotics and Computer Assisted Surgery*, vol. 13, no. 4, 2017. 9, 12, 81

[33] N. Garbin, P. R. Slawinski, G. Aiello, C. Karraz, and P. Valdastri, "Laparoscopic camera based on an orthogonal magnet arrangement," *IEEE Robotics and Automation Letters*, vol. 1, no. 2, pp. 924–929, 2016. 9, 81

[34] M. Simi, N. Tolou, P. Valdastri, J. Herder, A. Menciassi, and P. Dario, "Modeling of a compliant joint in a magnetic levitation system for an endoscopic camera," *Mechanical Sciences, 3 (1), 2012*, 2012. 9

[35] M. Beccani, E. Susilo, C. Di Natali, and P. Valdastri, "Smac–a modular open source architecture for medical capsule robots," *International Journal of Advanced Robotic Systems*, vol. 11, 2014. 9, 42

[36] A. C. Lehman, J. Dumpert, N. A. Wood, L. Redden, A. Q. Visty, S. Farritor, B. Varnell, and D. Oleynikov, "Natural orifice cholecystectomy using a miniature robot," *Surgical endoscopy*, vol. 23, no. 2, pp. 260–266, 2009. 9, 42

[37] J. C. Huhn, "Advances in equipment and instrumentation in laparoscopic surgery," *Veterinary Clinics of North America: Small Animal Practice*, vol. 46, no. 1, pp. 13–29, 2016. 14

[38] J. Shang, K. Leibrandt, P. Giataganas, V. Vitiello, C. A. Seneci, P. Wisanuvej, J. Liu, G. Gras, J. Clark, A. Darzi, *et al.*, "A single-port robotic system for transanal microsurgery - design and validation," *IEEE Robotics and Automation Letters*, vol. 2, no. 3, pp. 1510–1517, 2017. 14

[39] B. S. Terry, Z. C. Mills, J. A. Schoen, and M. E. Rentschler, "Single-port-access surgery with a novel magnet camera system," *IEEE transactions on biomedical engineering*, vol. 59, no. 4, pp. 1187–1193, 2012. 14, 81

[40] S. Boppart, T. Deutsch, and D. Rattner, "Optical imaging technology in minimally invasive surgery," *Surgical endoscopy*, vol. 13, no. 7, pp. 718–722, 1999. 14

[41] M. C. Cavusoglu, M. B. Cohn, F. Tendick, and S. S. Sastry, "Laparoscopic telesurgical workstation," in *BiOS'98 International Biomedical Optics Symposium*, pp. 296–303, International Society for Optics and Photonics, 1998. 14

[42] F. Jelınek, R. Pessers, and P. Breedveld, "Dragonflex smart steerable laparoscopic instrument," *ASME J. Med. Dev*, vol. 8, no. 1, p. 015001, 2014. 14

[43] M. A. Karim, J. Ahmed, M. Mansour, and A. Ali, "Single incision vs. conventional multiport laparoscopic cholecystectomy: a comparison of two approaches," *International Journal of Surgery*, vol. 10, no. 7, pp. 368–372, 2012. 15

[44] M. Cianchetti, T. Ranzani, G. Gerboni, T. Nanayakkara, K. Althoefer, P. Dasgupta, and A. Menciassi, "Soft robotics technologies to address shortcomings in today's minimally invasive surgery: the stiff-flop approach," *Soft Robotics*, vol. 1, no. 2, pp. 122–131, 2014. 19

[45] S. M. Strasberg, "A perspective on the critical view of safety in laparoscopic cholecystectomy," *Annals of Laparoscopic and Endoscopic Surgery*, vol. 2, no. 1, 2017. 20

[46] D.-H. Dong, W.-Y. Liu, H.-B. Feng, Y.-L. Fu, S. Huang, J.-X. Xiang, and Y. Lyu, "Study of individual characteristic abdominal wall thickness based on magnetic anchored surgical instruments," *Chinese medical journal*, vol. 128, no. 15, p. 2040, 2015. 22, 46

[47] X. Liu, G. J. Mancini, Y. Guan, and J. Tan, "Design of a magnetic actuated fully insertable robotic camera system for single-incision laparoscopic surgery," *IEEE/ASME Transactions on Mechatronics*, vol. 21, no. 4, pp. 1966–1976, 2016. 23

[48] N. Li, G. J. Mancini, and J. Tan, "Hardware design for a cable-free fully insertable wireless laparoscopic robotic camera," in *Engineering in Medicine and Biology Society (EMBC), 2016 IEEE 38th Annual International Conference of the*, pp. 5128–5131, IEEE, 2016. 26, 74

[49] P. Valdastri, A. Menciassi, A. Arena, C. Caccamo, and P. Dario, "An implantable telemetry platform system for in vivo monitoring of physiological parameters," *IEEE Transactions on Information Technology in Biomedicine*, vol. 8, no. 3, pp. 271–278, 2004. 26

[50] P. Valdastri, S. Rossi, A. Menciassi, V. Lionetti, F. Bernini, F. A. Recchia, and P. Dario, "An implantable zigbee ready telemetric platform for in vivo monitoring of physiological parameters," *Sensors and Actuators A: Physical*, vol. 142, no. 1, pp. 369–378, 2008. 26, 49

[51] J. K. Koehn and K. J. Kuchenbecker, "Surgeons and non-surgeons prefer haptic feedback of instrument vibrations during robotic surgery," *Surgical endoscopy*, vol. 29, no. 10, pp. 2970–2983, 2015. 30, 98

[52] K.-M. Lee, H. Son, J. Joni, *et al.*, "Concept development and design of a spherical wheel motor (swm)," in *IEEE International Conference on Robotics and Automation*, vol. 4, p. 3652, IEEE; 1999, 2005. 43

[53] C. Song, A. Alijani, T. Frank, G. Hanna, and A. Cuschieri, "Mechanical properties of the human abdominal wall measured in vivo during insufflation for laparoscopic surgery," *Surgical Endoscopy And Other Interventional Techniques*, vol. 20, no. 6, pp. 987–990, 2006. 46

[54] A. Shushan, H. Mohamed, and A. L. Magos, "How long does laparoscopic surgery really take? lessons learned from 1000 operative laparoscopies," *Human reproduction*, vol. 14, no. 1, pp. 39–43, 1999. 51

[55] N. Famaey, E. Verbeken, S. Vinckier, B. Willaert, P. Herijgers, and J. Vander Sloten, "In vivo soft tissue damage assessment for applications in surgery," *Medical engineering & physics*, vol. 32, no. 5, pp. 437–443, 2010. 53, 69, 94

[56] S. Arıtan, S. O. Oyadiji, and R. M. Bartlett, "A mechanical model representation of the in vivo creep behaviour of muscular bulk tissue," *Journal of biomechanics*, vol. 41, no. 12, pp. 2760–2765, 2008. 54

[57] A. R. Yazdanpanah, X. Liu, and J. Tan, "Modeling and analysis of a laparoscopic camera's interaction with abdomen tissue," in *Robotics and Automation (ICRA), 2017 IEEE International Conference on*, pp. 4227–4232, IEEE, 2017. 59, 61

[58] A. Taddese, M. Beccani, E. Susilo, P. Völgyesi, A. Lédeczi, and P. Valdastri, "Toward rapid prototyping of miniature capsule robots," in *Robotics and Automation (ICRA), 2015 IEEE International Conference on*, pp. 4704–4709, IEEE, 2015. 81

[59] S. L. Best and J. A. Cadeddu, "Development of magnetic anchoring and guidance systems for minimally invasive surgery," *Indian journal of urology: IJU: journal of the Urological Society of India*, vol. 26, no. 3, p. 418, 2010. 81

[60] M. Silvestri, T. Ranzani, A. Argiolas, M. Vatteroni, and A. Menciassi, "A multi-point of view 3d camera system for minimally invasive surgery," *Sensors and Actuators A: Physical*, vol. 202, pp. 204–210, 2013. 81

[61] X. Liu, G. J. Mancini, and J. Tan, "Design and analysis of a magnetic actuated capsule camera robot for single incision laparoscopic surgery," in *Intelligent Robots and Systems (IROS), 2015 IEEE/RSJ International Conference on*, pp. 229–235, IEEE, 2015. 81

[62] N. Li, A. R. Yazdanpanah, J. G. Mancini, and J. Tan, "Initial design and function verification of a cable-free insertable robotic laparoscopic surgical camera system," in *Robotics and Biomimetics (ROBIO), 2017 IEEE International Conference on*, pp. 319–324, IEEE, 2017. 81

[63] T. Hu, P. K. Allen, and D. L. Fowler, "In-vivo pan/tilt endoscope with integrated light source," in *Intelligent Robots and Systems, 2007. IROS 2007. IEEE/RSJ International Conference on*, pp. 1284–1289, IEEE, 2007. 81

[64] P. Valdastri, C. Quaglia, E. Buselli, A. Arezzo, N. Di Lorenzo, M. Morino, A. Menciassi, and P. Dario, "A magnetic internal mechanism for precise orientation of the camera in wireless endoluminal applications," *Endoscopy*, vol. 42, no. 06, pp. 481–486, 2010. 81, 82

[65] T. Hu, P. K. Allen, T. Nadkarni, N. J. Hogle, and D. L. Fowler, "Insertable stereoscopic 3d surgical imaging device with pan and tilt," in *Biomedical Robotics and Biomechatronics, 2008. BioRob 2008. 2nd IEEE RAS & EMBS International Conference on*, pp. 311–316, IEEE, 2008. 82

[66] D. J. Mirota, M. Ishii, and G. D. Hager, "Vision-based navigation in image-guided interventions," *Annual review of biomedical engineering*, vol. 13, pp. 297–319, 2011. 82

[67] P. Mountney, D. Stoyanov, and G.-Z. Yang, "Three-dimensional tissue deformation recovery and tracking," *IEEE Signal Processing Magazine*, vol. 27, no. 4, pp. 14–24, 2010. 82

[68] T. Collins and A. Bartoli, "3d reconstruction in laparoscopy with close-range photometric stereo," *Medical Image Computing and Computer-Assisted Intervention–MICCAI 2012*, pp. 634–642, 2012. 82

[69] M. Allan, S. Thompson, M. J. Clarkson, S. Ourselin, D. J. Hawkes, J. Kelly, and D. Stoyanov, "2d-3d pose tracking of rigid instruments in minimally invasive surgery," in *International Conference on Information Processing in Computer-assisted Interventions*, pp. 1–10, Springer, 2014. 82

[70] I. Umay, B. Fidan, and B. Barshan, "Localization and tracking of implantable biomedical sensors," *Sensors*, vol. 17, no. 3, p. 583, 2017. 82

[71] T. D. Than, G. Alici, H. Zhou, and W. Li, "A review of localization systems for robotic endoscopic capsules," *IEEE Transactions on Biomedical Engineering*, vol. 59, no. 9, pp. 2387–2399, 2012. 82

[72] H. Mateen, R. Basar, A. U. Ahmed, and M. Y. Ahmad, "Localization of wireless capsule endoscope: A systematic review," *IEEE Sensors Journal*, vol. 17, no. 5, pp. 1197–1206, 2017. 82

Vita

Ning Li was born in Tengzhou, Shandong, China in 1986. He received two Bachelor degrees respectively in Mechatronic Engineering and Economics from Tianjin University of Science and Technology, China in 2010. He received his Master degree in Mechanical Engineering and Automation at Beihang University, China in 2013. In August 2013, he joined Dr. Jindong Tan's lab at University of Tennessee, Knoxville and became a Ph.D. candidate later in 2014. He received multiple graduate teaching and research assistantships during his Ph.D research. He graduated with a Doctor of Philosophy degree in Mechanical Engineering in August 2018.